The Globular Cluster System of NGC 3115

JACKSON, RYAN,ANTONY

JACKSON, RYAN,ANTONY (2018) *The Globular Cluster System of NGC 3115*, Durham theses, Durham University. Available at Durham E-Theses Online: http://etheses.dur.ac.uk/12662/

The Globular Cluster System of NGC 3115

Ryan Antony Jackson

A Thesis presented for the degree of
MSc by Research

Centre for Extragalactic Astronomy
Department of Physics
University of Durham
England

January 2018

Dedicated to

Raymond and Gwen Carr

The Globular Cluster System of NGC 3115

Ryan Antony Jackson

Submitted for the degree of MSc by Research
January 2018

Abstract

The evolution of galaxies through cosmic time remains a key question in Extragalactic Astronomy. Globular Clusters (GCs) are believed to be good tracers of this evolution as they form during large star formation events. In this thesis we use spectroscopic data of GCs, taken using the FORS2 instrument on the Very Large Telescope, to create a catalogue of kinematics and metallicities for GCs in the S0 galaxy of NGC 3115. In order to do this the data was reduced using the ESO REFLEX program, creating 1D spectra for each of the GC targets. These were then fed into a modified version of the full spectrum fitting method 'pPXF' to extract the kinematics, metallicities and ages of each target. The dataset created via this method was then compared to, and combined with, supplementary data from other surveys to create a more complete catalogue of GCs in NGC 3115. From this catalogue there is evidence that the bimodal colour distribution is caused by a underlying bimodal metallicity distribution. Implying that at least two major star formation events have occurred in the history of NGC 3115.

Declaration

The work in this thesis is based on research carried out at the Centre for Extragalactic Astronomy, Department of Physics, University of Durham, England. No part of this thesis has been submitted elsewhere for any other degree or qualification and it is all my own work unless referenced to the contrary in the text.

Acknowledgements

I would like to thank my friends and family for all their support during the completion of this work. I would also like to thank my supervisor, Professor Ray Sharples, for his guidance and expertise throughout my time at Durham University.

Contents

List of Figures

List of Tables

Chapter 1

Introduction

Understanding how galaxies form and evolve over time is a major unanswered question in extragalactic astronomy. A deeper knowledge of the processes that create and change galaxies, building the Universe we see around us, would allow accurate modelling of many aspects of the Universe to become a possibility, potentially opening the doors to understanding some of the other great questions in cosmology and astronomy.

With this in mind, the search has been for tracers in galaxies, that might shed light on the processes involved in galaxy formation and evolution, more specifically their star formation history over the Hubble time since the Universe formed $\sim$13 Gigayears (Gyrs) ago. Given that $\sim$75% of the stellar mass in the local universe is in spheroids (Fukugita et al. 1998) (e.g. spiral bulges, halos and early-type galaxies), a tracer of this star formation needs to be formed from the same events as the bulk of stars, rather than low-level star formation in galaxies. This led astronomers to consider observing globular clusters (GCs) due to the observation that they are formed in significant numbers in galaxy mergers (Schweizer 2002; Ashman et al. 1992), which are thought to play a large role in galaxy evolution. Although the underlying processes forming GCs are not completely understood, there appears to be evidence to suggest they are a good candidate as will be discussed.

1.1 Globular clusters in galaxy evolution

1.1.1 Globular Clusters

Globular clusters are collections of old stars (relative to the host galaxy) that are gravitationally bound. They are generally spherical in shape and have a higher stellar density towards their centre. It is believed that the formation of GCs occurs in single star formation events from large clouds of gas, leading to all the stars contained within the cluster having the same physical properties (age, metallicity, abundance ratio). This is known as a simple stellar population (SSP). An integrated spectrum from an SSP would then allow mean values for the physical properties to be obtained. This is a key assumption, in both previous and current studies.

All galaxies of sufficient mass will contain a population of GCs (Harris 1991a). This fact, along with the assumption that GCs are SSPs, enables GCs to be used to track star formation in their host galaxies, and to measure specific properties of stars at different epochs over the galaxy's lifetime. If multiple populations of GCs are detected, then there has been more than one distinct star formation event in the lifetime of the galaxy.

More recently, there have been studies which suggest that GCs may not all be the SSP that they were once presumed to be (Decressin et al. 2008; Marino et al. 2008; Ferraro et al. 2004). These studies have shown evidence of multiple populations of stars contained within single GCs possibly due to differing ages and He abundances (Piotto et al. 2007). So far this phenomenon has only been attributed to large GCs in the Milky Way galaxy and, given the constraints of current instruments, cannot be tested in extragalactic GCs. Therefore, although useful to acknowledge the potential of multiple populations, it is safe to continue to approximate GCs as SSPs, at least for the purposes of these studies.

1.1.2 Specific Frequency

A key property for relating a GC population to its host galaxy is the specific frequency (S_N) (Harris et al. 1981). It is defined as the number of clusters per unit galaxy luminosity (Harris 1991a) and is defined numerically as:

$$S_N = N_{GC} \times 10^{0.4(M_V+15)} \tag{1.1.1}$$

Where N_{GC} is the total cluster population and M_V is the galaxy absolute magnitude. S_N can vary quite drastically between the different classifications of galaxies with spirals having S_N<1 (van den Bergh 1982) while ellipticals and S0s have S_N between 2-6 (Harris et al. 1981; Kundu et al. 1998). Understanding why some galaxies were more adept at holding or creating GCs became known as the 'Specific frequency problem', as seen in Figure 1.1. What causes these differences in S_N, for different galaxies, has become integral in the development of galaxy formation models (Harris 1991a).

The formation of elliptical galaxies via major mergers of spirals, for example, was called into question by van den Bergh (1982) due to spirals having a lower S_N than elliptical galaxies by a factor of ∼3-6. However, Ashman et al. (1992) argued that S_N would increase after a merger if new GCs were formed. Ashman et al. (1992) predicted that there would be two populations of GCs after the merger, a metal-poor one and a metal-rich one; these were indeed observed in elliptical galaxies shortly after (Zepf et al. 1993). However, this does not account for the high S_N in S0 galaxies, as they are not expected to have been formed by mergers (West 1993). They have also been observed to contain bimodal populations of GCs (Kundu et al. 2001) but the processes that caused these are still being researched.

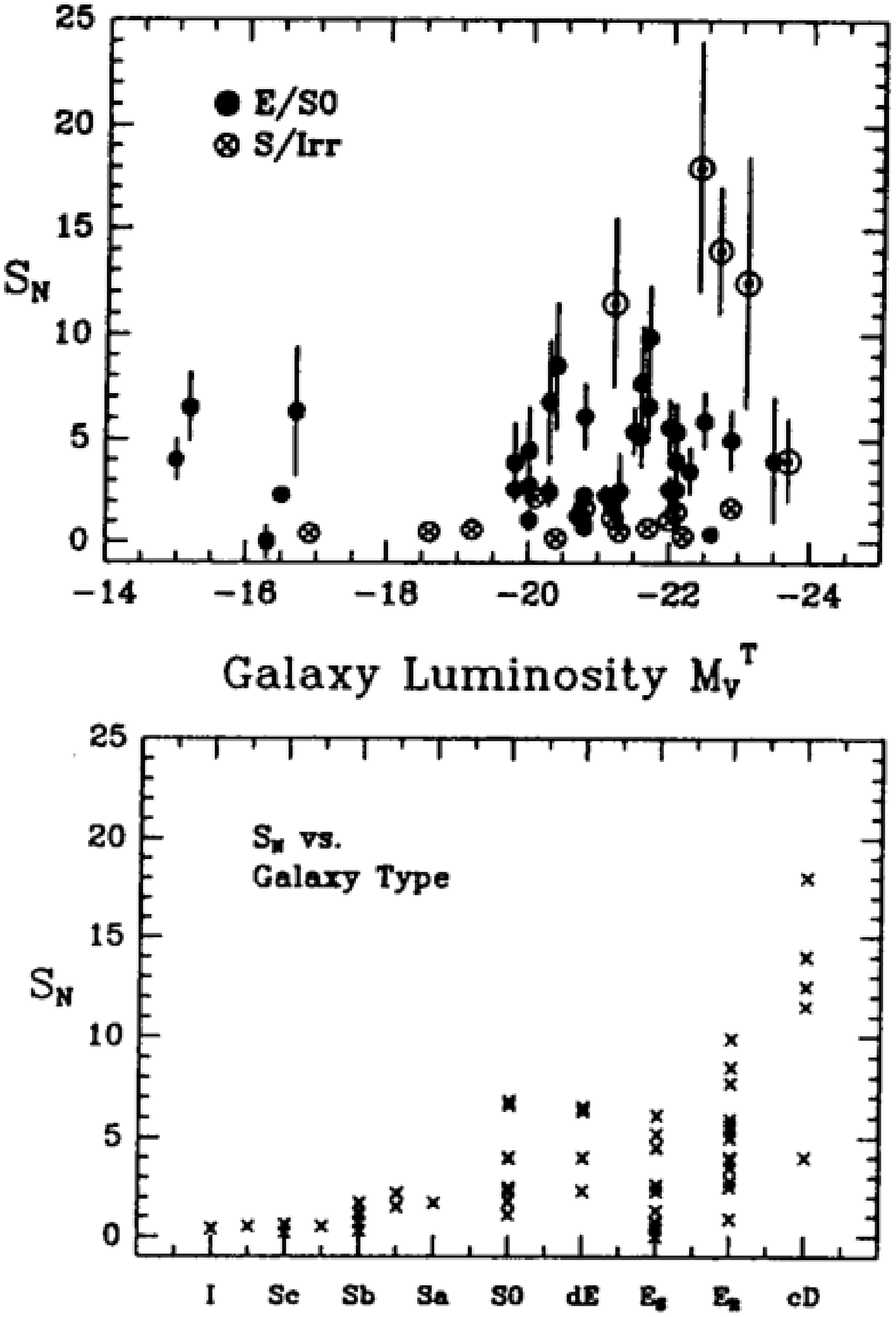

Figure 1.1: The upper plot shows galaxy luminosity against specific frequency, where the filled circles represent elliptical and S0 galaxies and the crossed circles represent spiral and irregular galaxies. Five giant ellipticals at the centres of rich clusters (Virgo, Fornax, Hydra, Coma, A2199) are denoted by the circled dots. The bottom plot shows specific frequency against morphological classification. E_R and E_S represent ellipticals in rich and sparse clusters respectively and c_D shows the central-giant ellipticals from the upper plot. Taken from Harris (1991b).

1.1.3 Bimodality of GC populations

One of the most significant discoveries in the field of extragalactic GCs, is the observation that most colour distributions of GC systems are bimodal (Peng et al. 2006b), as can be seen in Figure 1.2. This suggests that the majority of massive galaxies contain at least two distinct sub-populations of GCs as seen in Figure 1.3. The differences in colour between the sub-populations could be caused by a difference in age, in metallicity or a combination of both. Therefore, spectroscopy of individual GCs is needed to identify the true cause.

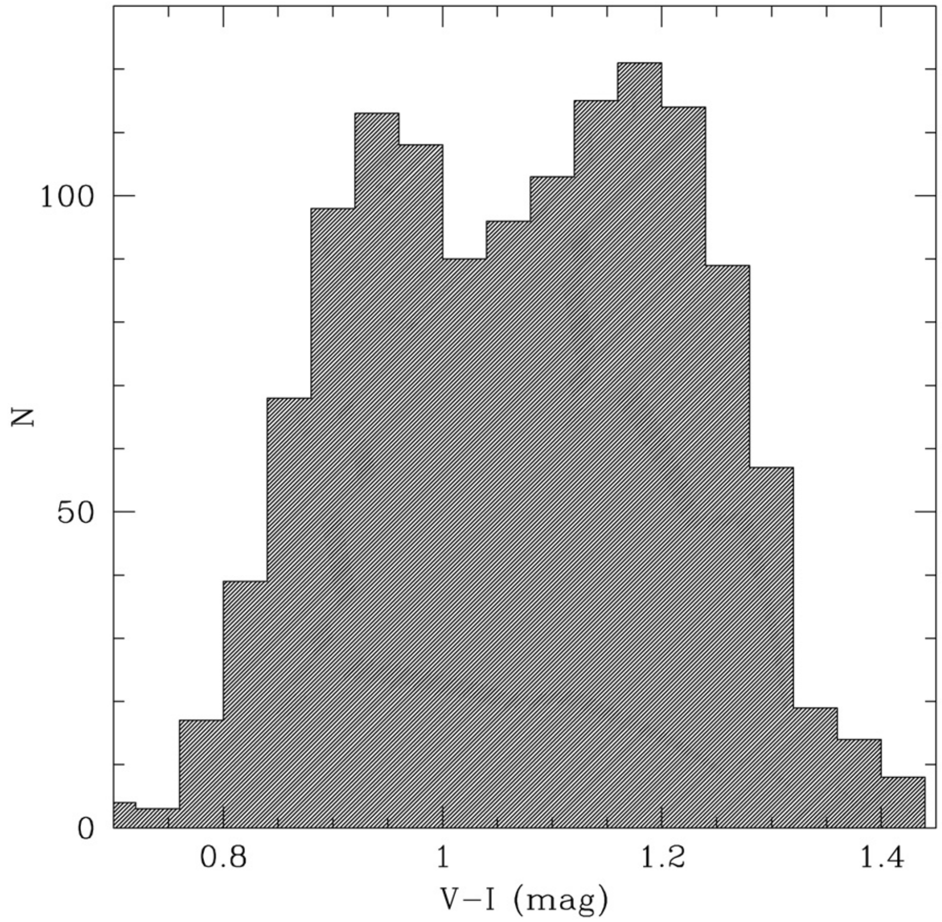

Figure 1.2: Histogram of the V-I colour of GCs in M87 in the Virgo cluster. The histogram shows the GCs to have a bimodal colour distribution. Taken from Larsen et al. (2001).

After many GC surveys, both in the Milky Way and other galaxies, it has been confirmed that the most likely cause of the difference in colour is due to differing metallicities in two older sub-populations of GCs (Kuntschner et al. 2002; Brodie et al. 2012; Barmby et al. 2000; Harris 1996). This suggests that there is an older metal-poor population, most likely formed during the galaxies' early formation, and a younger metal-rich population formed later. The findings of some of these studies, in particular ones more relevant to the research of this thesis, will be discussed later in this chapter.

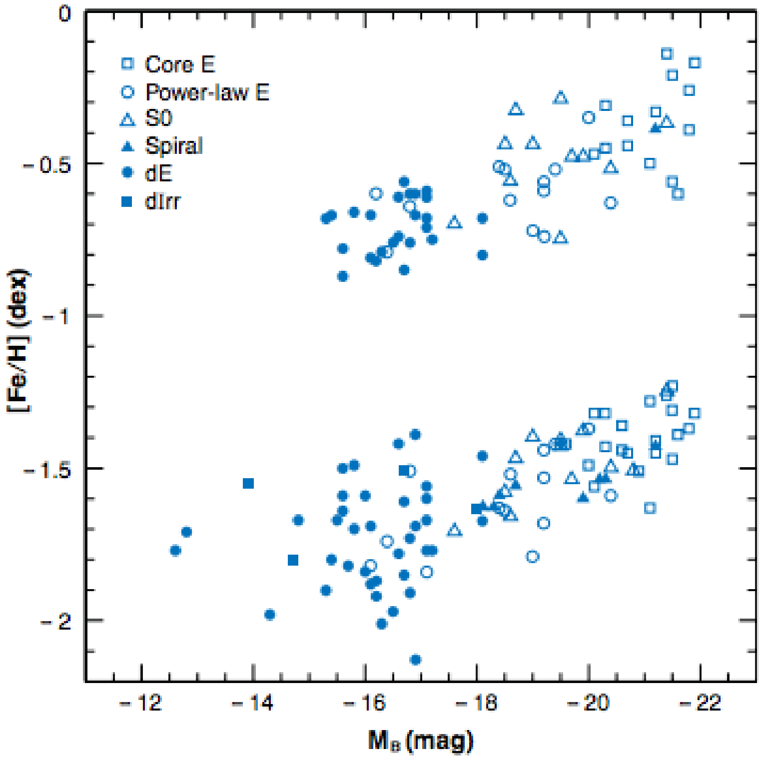

Figure 1.3: Globular cluster mean metallicity against galaxy luminosity (M_B) for metal-poor and metal-rich GC sub-populations in a variety of galaxies. Data is from Strader et al. (2004) and Strader et al. (2006) and was converted from V-I and g-z to [Fe/H] by the relations of Barmby et al. (2000) and Peng et al. (2006a). Figure taken from Brodie et al. (2006)

In order to explain these multiple sub-populations, there needs to be a mechanism by which multiple star formation events are triggered. There are three widely discussed scenarios that could produce such events. The first idea is the major merger model Zepf et al. (1993), which built on research relating to the formation of elliptical (E) galaxies by major mergers (Schweizer 2000; Toomre et al. 1972). It suggests that the metal-poor GCs come from the original disk galaxies, whilst the metal-rich GCs are formed during the merger, where the interaction between the two galaxies initiates a star formation event.

This model was examined by Forbes et al. (1997), who argued that the colour distributions of the GCs in the elliptical galaxies were not in line with what should be seen from a major merger. More precisely, it was discovered that the relative numbers of GCs and their colour distributions were not consistent with the predictions made by the theory. Forbes et al. (1997) offered an alternate theory, whereby the metal-poor GCs were formed in fragments of gas in the early stages of galaxy formation. GC formation then ceased for a few Gyrs, and then resumed, along with the formation of the field stars Forbes et al. 1997. This is known as multi-phase dissipational collapse. Forbes et al. (1997) suggested that this could occur via feedback, where gas was removed from the gas clouds, that earlier formed GCs, and then cooled over time, before eventually becoming dense enough to collapse, forming the new metal-rich GCs.

The third model, discussed for the origin of bimodality, is the accretion scenario (Côté et al. 1998). In this scenario, metal-rich GCs are formed in large seed galaxies and the metal-poor GCs are acquired, not from a second star formation event but via accretion from low mass neighbouring galaxies or satellites. This idea is plausible as there is a known connection between the mass of a host galaxy and the mean metallicity of its GC populations (Brodie et al. 1991; Forbes et al. 2001; van den Bergh 1975). However, it is reliant on two key assumptions:

- Firstly, that E galaxies have a 'zero-age' population of GCs that were formed during the initial collapse of the host galaxy and whose metallicity increased in line with galaxy mass.
- Secondly, that the initial galactic mass-function of the low-mass galaxies is

steep. This is consistent with λCDM models but is currently steeper than observations would suggest.

The actual cause of GC bimodality has still not been completely identified and it is hoped that studies such as the present one, performed on a variety of galaxies, may shed light on its true nature. Its implication, however, is that galactic star formation can be tracked using GC populations and when its origin is known, we can use GCs as a fossil record of what has happened to the galaxy since its formation.

1.2 The Lenticular (S0) Galaxy NGC 3115

NGC 3115 is a lenticular (or S0) galaxy that is almost edge-on to the Milky Way, located in the Sextans constellation at a right ascension (RA) of $10^h05^m14.0^s$ and a declination (dec) of $-7^o43'07$" (Materne 1979). It is located at a distance of 9.7 Megaparsecs (Mpc) and has a radial velocity of 665 [$\pm$39] kms^{-1} (Paturel et al. 2002; Tonry et al. 2001). At this distance 3115 is one of the closest S0 galaxies, making it a prime candidate for studies of extragalactic GC systems.

S0 galaxies are believed to be an intermediate type of galaxies between spirals and elliptical galaxies. They differ morphologically from elliptical galaxies as they contain a stellar disk. They do, however, share similarities as they both have little or no on-going star formation and share some spectral features and scaling relations. From galaxy surveys, there is an increase in population size of S0's since a redshift of 1 whilst simultaneously there has been a decrease in the number of spiral galaxies, particularly in cluster environments (Dressler et al. 1997). This leads to a conclusion that their evolution must somehow be linked.

One theory of their formation is that S0 galaxies are spiral galaxies in which star formation has ceased and have been passively evolving since. This is plausible given that the there is an absence of gas but presence of dust in the disk (Elmegreen et al. 2002). Moore et al. (1998) suggest that tidal harassment from nearby galaxies could contribute to this and cause the disappearance of the spiral structures in the galaxies arms. It has also been suggested that S0 galaxies could be formed via merger processes. Burstein et al. (2005) and Sandage (2005) both found that S0's had a higher surface brightness than spiral galaxies, this could be accounted for if the S0 was the result of a major merger.

The idea of S0's being faded spirals has also been tested by looking at GCs in S0 galaxies, Aragón-Salamanca et al. (2006) and Barr et al. (2007) showed that, as the age of the central region of an S0 galaxy increased, so did its GC specific frequency. The increase measured is what would be expected if the galaxy was formed from the fading of a disk after star formation ceased. Figure 1.4 shows the findings of both studies. For younger S0 galaxies their specific frequencies were closer to that of spirals whereas older S0's were closer to that of ellipticals supporting the theory of S0 galaxies being formed from fading spirals. Barr et al. (2007) also assert that, given there are no young S0's with a high specific frequency, large amounts of GCs cannot be created during S0 formation. Or that if they are, the galaxy undergoes a large increase in luminosity at the same time.

1.3 Previous investigations of NGC 3115

The work contained in this thesis follows on from two previous studies of the GC system of NGC 3115. They are: 'VLT spectroscopy of NGC 3115 globular clusters' by Kuntschner et al. (2002) (hereafter K02) and 'The SLUGGS Survey: NGC 3115, A critical test case for metallicity bimodality in globular cluster systems' by Brodie et al. (2012) (hereafter B12). Our study examines GCs in the same area of the sky as both of these surveys, and so provides some overlap of results. This section will, therefore, examine in detail the results these two particular studies before giving an

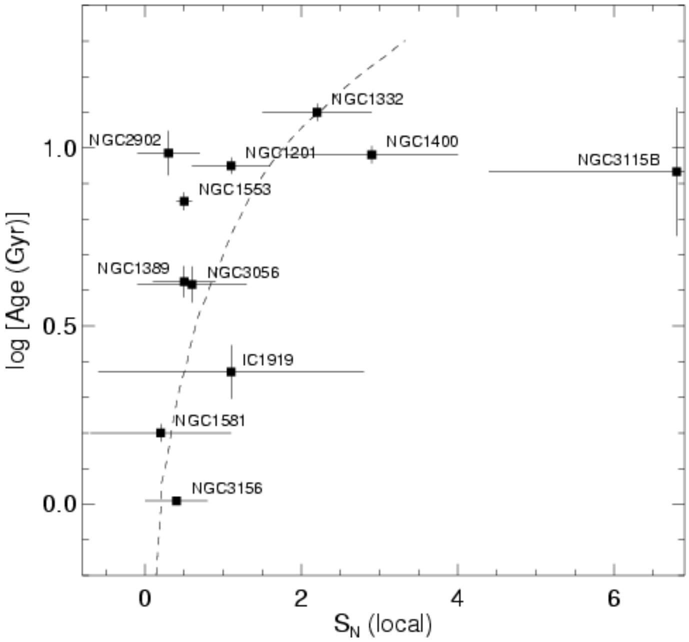

Figure 1.4: The graph shows derived ages for S0 galaxies against their specific frequency. The dashed line is what is expected from a fading galaxy with a starting S_N=0.4, from the stellar population models of Bruzual et al. (2003). Taken from Barr et al. (2007)

overview of other studies that have been conducted on NGC 3115, and give their findings.

1.3.1 VLT spectroscopy of NGC 3115 globular clusters

K02 was the first spectroscopic study dedicated to looking at the GC system of NGC 3115 and is the foundation for our work. In this paper, ∼50 globular cluster candidates were studied using the FORS2 spectrograph on the Very Large Telescope (VLT). Of that number, radial velocities for 28 GC candidates were obtained, which were then compared to the radial velocity of NGC 3115, to decide whether the candidate was a member of the NGC 3115 GC system. For their observations, K02 decided that the velocity cut-off would be between 200-1300kms^{-1}, and 26 of the candidates met this criterion.

To calculate metallicity from the line-strengths of the spectra, K02 enforced a cap

Figure 1.5: Histogram of (V-I) colours for GC candidates in NGC 3115 from Kuntschner et al. (2002) (filled histogram) and Kundu et al. (1998). Taken from Kuntschner et al. (2002).

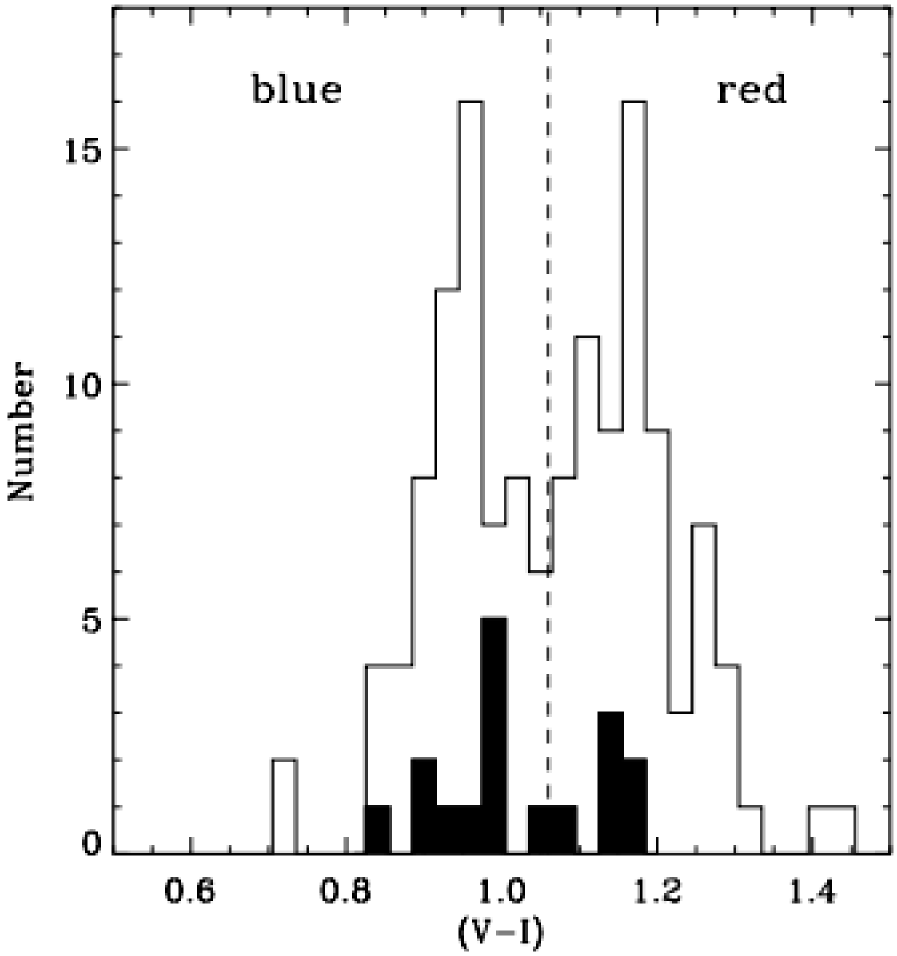

on the signal to noise ratio (SNR) of $\geqslant 12$ per pixel which reduced the sample size to 17 clusters. From this sample, the mean radial velocity was 600 [±12.6] kms^{-1}, with a dispersion of σ =215 kms^{-1}. The colour distribution of this sample can be seen in Figure 1.5. Out of the final 17 candidates, 9 had a high enough quality spectrum to obtain line strength indices and are also kinematically associated with NGC 3115. In order to obtain abundance ratios, metallicities and ages of their GCs the ratio of Mg to Fe, and line strengths of Hβ and [MgFe] were used. The line strength indices system used to obtain age and metallicity in this study was the LICK/IDS system (Worthey et al. 1997; Trager et al. 1998). The data from the FORS spectroscopy needed to be convolved with a gaussian kernel in order to match the resolution of the LICK/IDS system. The line strengths could then be measured against the LICK definitions and used in the analysis.

Metallicities and ages were calculated for each of the candidates in the sample. As the error bars are large in around half of the spectra, an error-weighted mean for age and metallicity was calculated. This gave mean ages of $12^{+1.5}_{-2.0}$ and $10.8^{+1.7}_{-1.8}$ Gyrs for the metal-poor and metal-rich clusters respectively. The average [Fe/H] was -1.05 ± 0.09 for the metal-poor sample and -0.26 ± 0.05 for the metal-rich sample; where the errors quoted are 1σ values. K02 also examine the abundance ratios of the GCs in NGC 3115. They find that [Mg/Fe] varies from around the solar value to $\simeq 0.3$ and note that there appears to be no trend with colour. With both sub-populations containing varying abundance ratios.

K02 concluded from their data that there were two populations of GCs in NGC 3115 and that they had the same age of 11-12Gyr using the H_β vs [MgFe] measurements. K02 also used higher order Balmer line measurements (Hγ, Hδ) and obtained ages of 7 and 5 Gyr for the blue and red clusters. This is a large offset from the ages obtained using H_β, and K02 believe this discrepancy is due to an inaccurate calibration of higher order Balmer lines in the models used for the age calculation. It is therefore suggested, that this measurement should not be taken as reliable and one should instead use the H_β vs [MgFe] measurements for age estimates.

In the discussion of their findings, K02 do make the concession that their data is dominated by the bright end of the luminosity function and that this may play a role in the conclusions that can be drawn from the data. It cannot be concluded that the two populations are separated by age, as well as metallicity, as the data suggests that they both formed around 11-12 Gyr ago, although it is possible for the red clusters to be slightly younger.

It can be concluded from their data that the metal-rich clusters, with solar [Mg/Fe] abundance ratios, must have been well mixed containing the products of both Type 2 and Type 1a supernovae. Thus, knowing that Type 1a supernovae are delayed with

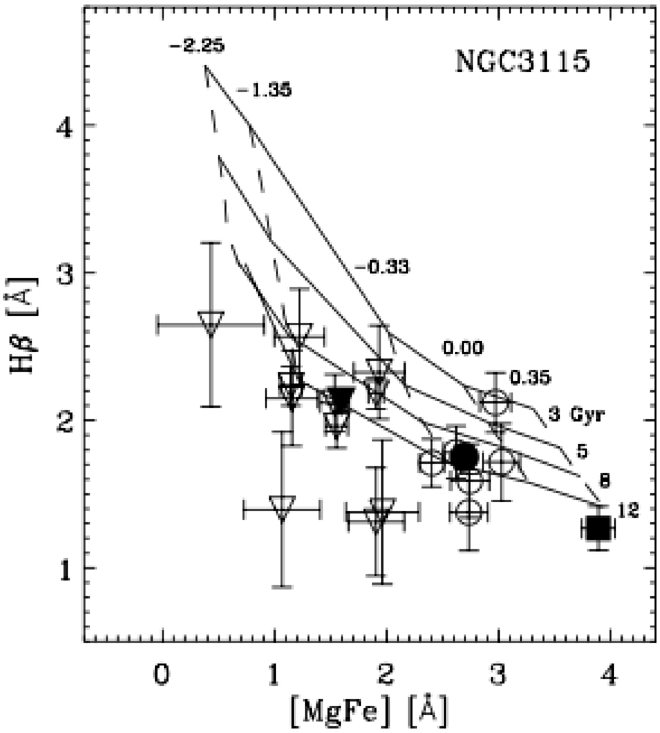

Figure 1.6: An age and metallicity diagram from Kuntschner et al. (2002). Using [MgFe] as the metallicity indicator and H_β as the age indicator. The K02 sample of GCs are the open triangles and circles, representing the red and blue clusters respectively. The filled triangle and circle are the error weighted means of their respective cluster and the filled square represents the centre of NGC 3115 from Trager et al. (1998). The solid and dashed lines are the ages and metallicities from solar-abundance ratio SSP models by Thomas et al. (2002a) and Maraston (2002) over the ranges [Fe/H] $= -2.25, -1.35, -0.33, 0.00, 0.35$ (dashed lines, left to right) and ages 3, 5, 8 and 12 Gyr (solid lines from top to bottom).

respect to Type 2 in an SSP, those clusters with solar abundance ratios must have formed after the initial star burst event. K02 suggest that the possible scenarios needed to explain the observed abundance ratio distribution, are difficult to fit within a theory that only involves two formation events, creating the red and blue clusters.

K02 put forward a hypothesis that the metal-poor non-solar abundance ratio clusters are formed with the halo, and the metal-rich non-solar abundance ratio clusters are formed with the bulge during the galaxy's formation. Then around 1-2 Gyr later, the metal-rich solar ratio clusters are formed with the disk, possibly due to another star forming event (ie merger). In order for this scenario to be correct the disk stars would need to have near solar abundance ratios. The kinematics of the GCs in the disk would also be expected to be clearly different from GCs contained in the halo or bulge of NGC 3115. K02 therefore conclude, that more spectroscopic studies of GCs in nearby galaxies are needed in order to improve our understanding of the formation of GCs.

The study presented in this thesis, aims to address this issue by adding more GCs to the catalogue for NGC 3115 and at a larger galactocentric radii. This will help to remove any biases caused by the sample size of the data and the spatial distribution of different sub-populations.

1.3.2 The SLUGGS Survey: NGC 3115

The SLUGGS survey (The SAGES Legacy Unifying Globulars and GalaxieS) has looked at 25 early-type galaxies with a range of stellar masses, central stellar kinematics and environments all within a range of 30 Megaparsecs (Forbes 2017). It uses the Subaru Suprime-Cam (Miyazaki et al. 2002) for its *gi* photometry and Keck/DEIMOS for spectroscopy. Unlike the Kuntschner et al (2002) study, SLUGGS uses the CaT index that measures the Calcium II triplet at ∼850nm for spectroscopic metallicity estimates. In NGC 3115, B12 obtained kinematics and metallicities for ~150 GCs from different areas of the galaxy, and aimed to provide more clarity on the bimodality of the GC population.

B12 note, in their discussion, that there have been criticisms of using the CaT index as a measure for metallicity, as it may become less sensitive at high metallicities [Z/H]>-0.4 and that it may also be sensitive to changes in the horizontal branch morphology (Foster et al. 2010). However, B12 assert that SSP models have now shown these effects to be minimal and therefore would not impact on the results of their survey.

From the initial data set, a cut at SNR > 12 per Angstrom was set, to produce a sample of 71 GCs. Figure 1.7 shows the histogram of metallicities derived from the CaT index for the sample, and it clearly has a bimodal distribution. Overlain are predictions based on colour-metallicity relations suggested by models from Yoon et al. (2011) and Usher et al. (2012).

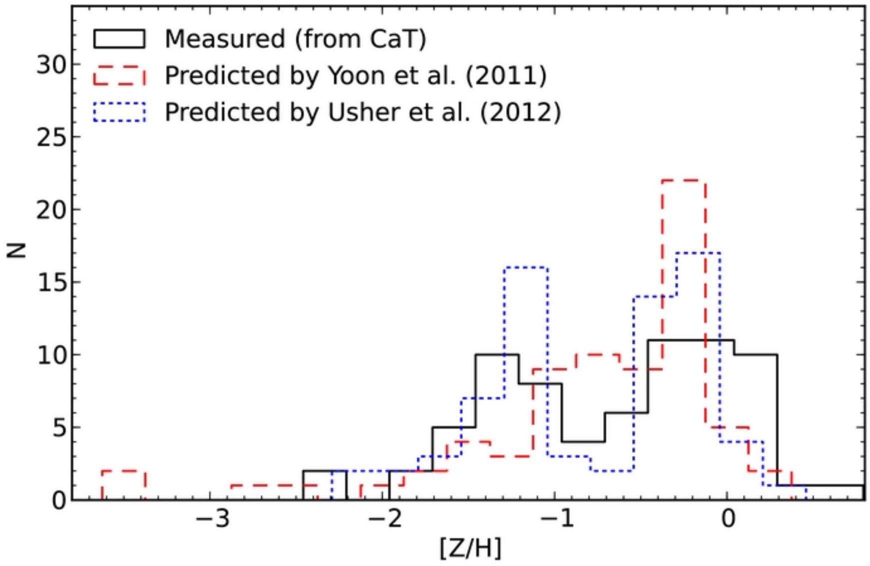

Figure 1.7: GC metallicity distribution functions (MDF) in NGC 3115. The solid line shows the MDF derived from the the CaT measurements. The dashed line is obtained from (g-i) colours using the Yoon et al. (2011) non-linear colour-[Z/H] relation and the dotted line is obtained using the Usher et al. (2012) empirical colour-[Z/H] relation. Taken from Brodie et al. (2012)

B12 conclude that the CaT index can effectively be used to obtain metallicities for GCs and that in NGC 3115 both the colour and CaT observations show a bimodal population. Figure 1.7 indicates that the suggestion by Yoon et al. (2006), that the populations are in fact uni-modal, and only appear bimodal due to an artefact of nonlinear colour-metallicity transformations, cannot be the case for NGC 3115.

The B12 study provides an excellent comparison sample for the study in this thesis, due to its large sample size and use of the CaT line to obtain metallicities. Whilst there could be potentially large offsets between the data due to the difference in methods used to obtain metallicity, if the results are consistent, it would prove to be a major verification for the theory that the bimodality is caused by metallicity and not age or horizontal branch offsets.

1.3.3 Other work

There have also been several photometric studies of the GC population of NGC 3115 in both the optical and in the infrared (Puzia et al. 2002; Cantiello et al. 2014; Jennings et al. 2014). The results of the colour distributions for an infrared and optical study can be seen in Figure 1.8 and Figure 1.9.

The infrared studies assumed the following relation in order to convert colour into [Fe/H] (Puzia et al. 2002):

$$[Fe/H] = -5.52(\pm 0.26) + 1.82(\pm 0.11) \times (V - K) \tag{1.3.2}$$

Whereas the optical studies used (Peng et al. 2006a):

$$[Fe/H] = -6.21 + (5.14 \pm 0.67) \times (g - z) \tag{1.3.3}$$

for $0.7 < (g - z) \leq 1.05$ and outside of that range using:

$$[Fe/H] = -2.75 + (1.83 \pm 0.23) \times (g - z) \tag{1.3.4}$$

This allowed the two results to be compared against each other, and along with agreeing on a bimodal colour distribution, the studies all agree that the two populations of GCs are separated by metallicity. A drop in the numbers of GCs with metallicities in the range $1.1 > [Z/H] > 0.4$ is found in the studies, creating a bimodal metallicity distribution. Comparing the photometric and spectroscopic studies shows that the conclusions from both are consistent with each other. All of the studies to date have agreed on a bimodal distribution for the GC population of NGC 3115 in both colour and metallicity.

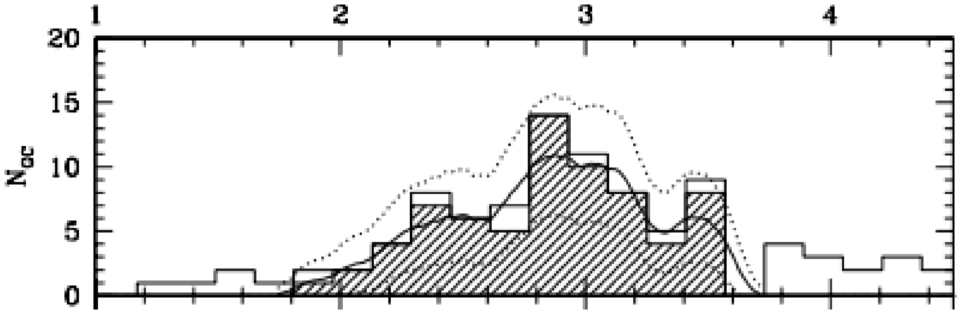

Figure 1.8: V-K histogram plot of all sources (solid histogram) and GC candidates (shaded histogram) along with a probability-density estimate of the data (thick line) and it's 1σ uncertainty (dotted lines) for NGC 3115. Taken from Puzia et al. (2002)

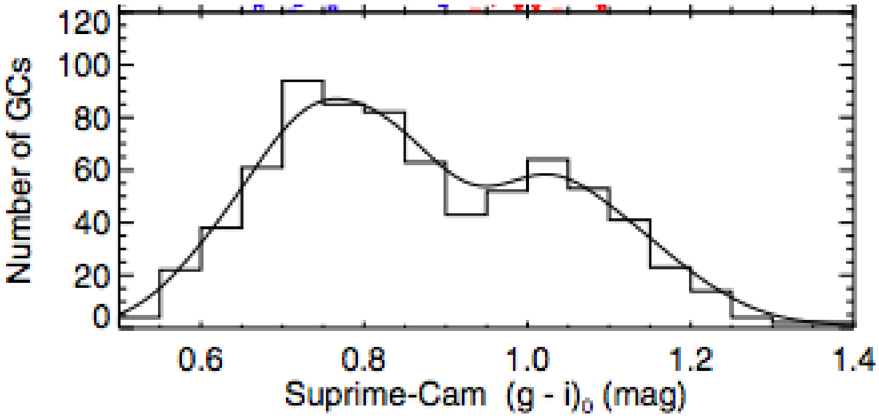

Figure 1.9: (g-i) histogram for Suprime-Cam imaging of detected GC candidates in NGC 3115 from Jennings et al. (2014). Overlaid is a Gaussian kernel density estimate which was normalised so the total number of GCs is the same as in the histogram.

It is also useful to examine other work that has been done on NGC 3115, such as integrated light spectroscopy of the galaxy. This allows comparisons between these findings and those obtained from observing the GC population.

Norris et al. (2006) looked at NGC 3115 using long slit spectroscopy from the GMOS instrument. The spheroid of NGC 3115 was found to have a similar age, metallicity and [α/Fe] to that of the red GC population (Norris et al. 2006), which is suggested as an indication of a common origin. However, the study also found evidence of a younger (5-8 Gyr) and chemically enriched stellar population in the disk, meaning it was likely formed in a different star formation event to the spheroid. An issue of Kuntschner et al (2002) was also addressed, as the offset in ages obtained from Hβ and higher order Balmer lines can be explained mostly by a varying [α/Fe].

In relation to the GC population, Norris et al. (2006) argue that the red GC population and the spheroid could have formed at the same star formation epoch, due to their shared parameters, whereas the blue GC population probably came from the initial star formation burst when the halo was formed.

1.4 Outline of this thesis

The aim of this thesis is to continue the work of these studies and add to the catalogue of kinematics and metallicities for GCs in NGC 3115. The original objective of the observations that this thesis is based on, was to measure spectroscopic ages, metallicities and [α/Fe] ratios for around 100 GCs, along with measuring velocities for ~200 GCs at a range of radii from the galactic centre.

In this thesis, the methods used for the data reduction and analysis of the observations will be presented, as well as discussing the implications of the results and comparing them to the previous studies of the system.

The general structure will be as follows:

- Chapter 2 presents the data reduction including the methods and software used to accomplish it. It will also look at the quality of the data and any problems that occurred during the reduction.
- Chapter 3 presents the data analysis and explores how the pPXF programme (Cappellari 2017) can be used to derive ages and metallicities for GC populations. It will also look at the issues encountered and what could be done to increase the quality and reliability of the results.
- Chapter 4 presents the results of this analysis including final kinematics and metallicities, along with data from other studies to create a more complete catalogue of GCs for NGC 3115
- Chapter 5 presents a discussion of the results, in the context of GC formation theories, and the conclusions that can be drawn from them. It will also present a summary of the thesis and areas of potential future research.

Chapter 2

Observations and Data Reduction

The study presented in this thesis focuses on spectroscopic observations the GC population of NGC 3115 on a larger scale than had been previously attempted at the time of the observations, covering a range of targets at various galactocentric radii. The main aims of this study are:

- To measure ages, metallicities and [α/Fe] ratios of ∼100 GCs around NGC 3115
- To measure velocities of ∼200 GCs with which to constrain the dark matter (DM) content and profile of NGC 3115

The observations were taken in 2008-2009 and, at the time, would have been the largest study of the GC population in NGC 3115. Since then the SLUGGS survey has taken place, observing at least as many GCs as this study, and covering a similar area of the galaxy. However, not only are the majority of the target GCs different between the two surveys, but repeat measurements of GCs, in different studies, will only help to confirm findings. Also, both studies have used different methods of obtaining metallicities and differing wavelength ranges, so the comparisons between them will provide insight into the reliability of the methods used and any systematic offsets.

2.1 Instrument Description

The data for this study was obtained using the FORS2 spectrograph instrument on the ESO Very Large Telescope (VLT). The VLT is operated by the European Southern Observatory (ESO) and consists of 4 main Unit Telescopes (UT 1-4), each with an 8.2m diameter mirror. The observatory is located on Cerro Paranal in the Atacama Desert of northern Chile, with coordinates of 24°37'38"S, 70°24'15"W and an altitude of 2,635 m. These telescopes can either work individually, as in this case, or in conjunction with each other, to create a large interferometer (ESO 2011b).

FOcal Reducer/low dispersion Spectrograph 2 (FORS2) is a multi-function optical instrument that is located at UT1's Cassegrain focus (see Figure 2.1). It can observe in imaging, polarimetry, long slit and multi-object spectroscopy modes over a wavelength range of 330-1100 nm (Appenzeller et al. 1998). For the observations described here the instrument was used in Multi-Object Spectroscopic Mask (MXU) mode and the observations were taken in service time. This allows for the most GC targets to be observed simultaneously in each exposure, with a mask produced containing a set number of slits covering the GC targets in each field. In order to achieve this, the FORS Instrumental Mask Simulator (FIMS) is used to create the masks in advance of the observations. FIMS has a graphical user interface which enables users to see the FORS field of view and position the slits of the MXU mask on the image (see Figure 2.2). This enables users to create optimised masks that cover as many targets as possible within the field of view.

This telescope and instrument were selected for this study due to the criteria needed to successfully observe GCs in NGC 3115. In order to obtain accurate metallicities,

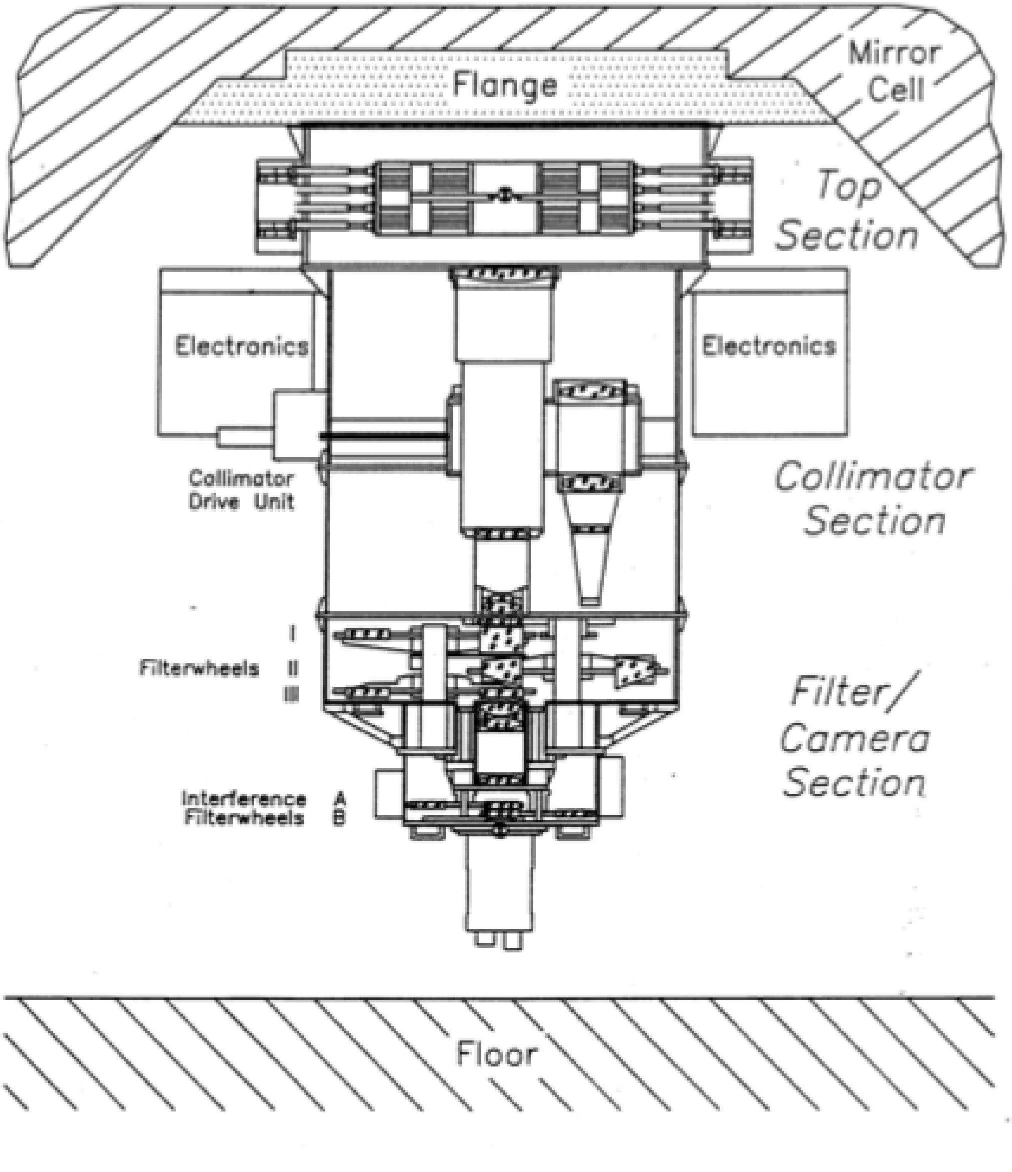

Figure 2.1: Diagram showing a schematic view of the FORS instrument at the Cassegrain focus of UT1. Taken from the FORS2 User Manual.

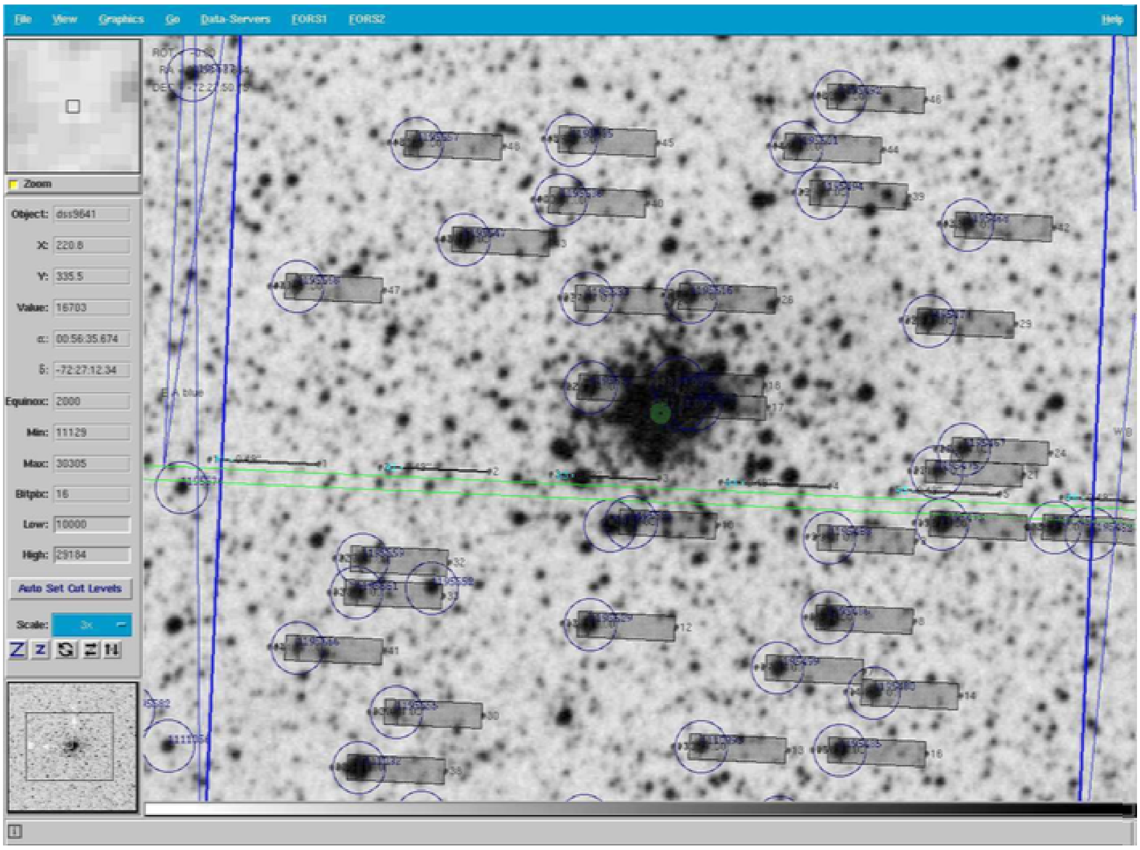

Object: dss9641
X: 220.8
Y: 335.5
Value: 16703
α: 00:56:35.674
δ: -72:27:12.34
Equinox: 2000
Min: 11129
Max: 30305
Bitpix: 16
Low: 10000
High: 29184

Figure 2.2: An example of FIMS being used to place slits on a field whilst in MXU mode. Taken from the FIMS manual.

a signal to noise ratio (SNR) of around 12 per Angstrom (Kuntschner et al. 2002) is needed. Therefore, for objects at the distance of 9.7 Mpc, and the luminosity of a GC (typically $\sim M_V = -6.5$), a large telescope such as the VLT is required. FORS2 was chosen due to its large field of view (6'.8x6'.8 for standard resolution and 4',2x4'.2 for high resolution), allowing observations of GCs at a range of galactocentric radii (up to 30 kpc). In order to probe to even larger galactocentric radii, some fields were centred on the major axis of NGC 3115, and also offset into the halo (Figure 2.3).

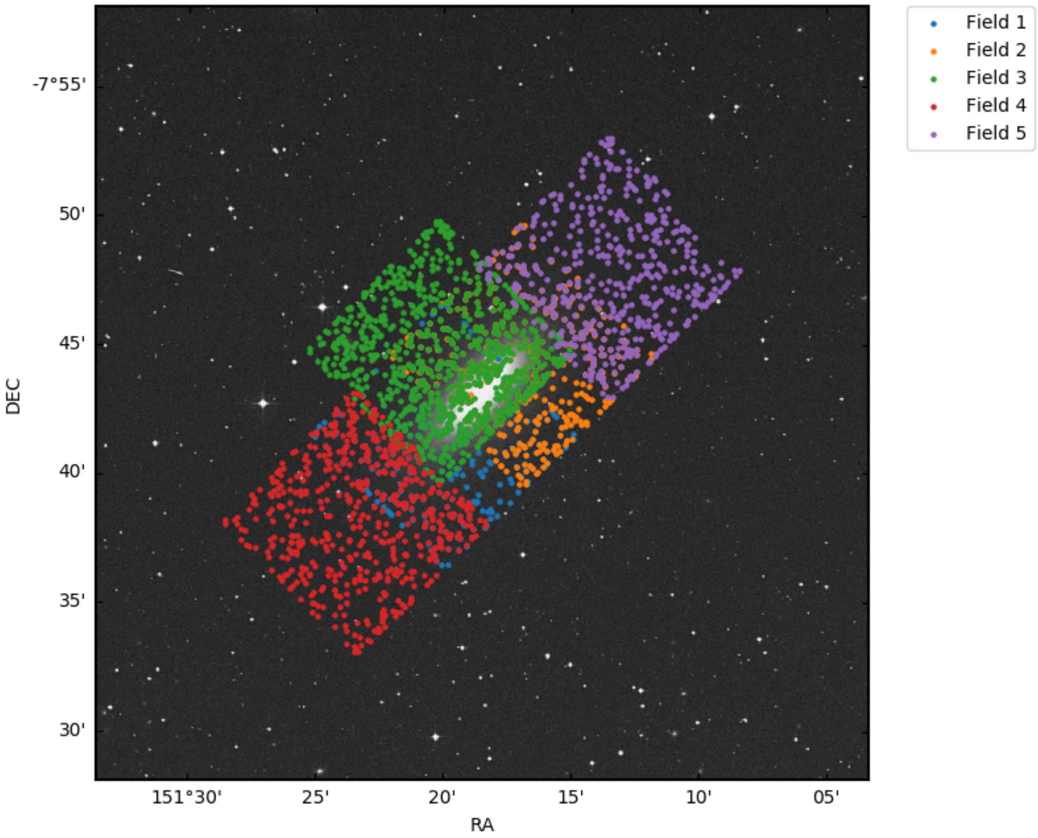

Figure 2.3: All possible GC candidate targets, identified from pre-imaging exposures taken with the same instrument. Each colour represents a field around NGC 3115 which can be identified by the legend. The image of NGC 3115 is obtained from the SDSS survey (Abolfathi et al. 2017).

The observations were taken over two observing runs, as the initial run didn't observe all of the requested fields. They have the program ID's: 083.B-0720(A) and 081.B-0633(B). The observations covered 5 fields in NGC 3115, as seen in Figure 2.3. The

Table 2.1: The Field ID, Mask ID, central coordinates and exposure times of the masks used in this study.

Field	Mask ID	RA	Dec	Exposure Time (s)
1	971913	151.331935	-7.69047	10800
2	901611	151.280663	-7.74215	13500
3	913942	151.389366	-7.63397	13500
4	925440	151.223613	-7.79916	13500
5	970716	151.335022	-7.74496	13500

areas selected covered targets previously observed in Kuntschner et al. (2002), along with previously unknown GC candidates based on the pre-imaging. The locations of the masks along with their IDs and exposure times can be seen in Table 2.1.

2.2 Target selection and Pre-imaging

Pre-imaging of the fields was taken in order to aid target selection and the reduction of these images was completed by Dr Mark Norris. The pre-imaging was taken using V,R and I filters, each for an exposure time of ∼ 35 seconds. The imaging was also zero pointed to match the photometry of Puzia et al. (2004), which allowed the two sets of data to be directly compared. The depth of the pre-imaging can be seen in Figure 2.5, which is ∼ 24.5 magnitude. Although as seen from the figure the cut-off magnitude used was slightly lower than this as seen in Figure 2.4.

From the pre-imaging, objects were extracted using SExtractor (Bertin et al. 1996) and several cuts were applied. These cuts removed any objects that had an R-band ellipticity of less than 0.4 and an R-band Class Star of greater than 0.5. This ensured that the objects were close to round and not obviously extended sources, in order to attempt to remove any background galaxies. As seen in Figure 2.5 there were

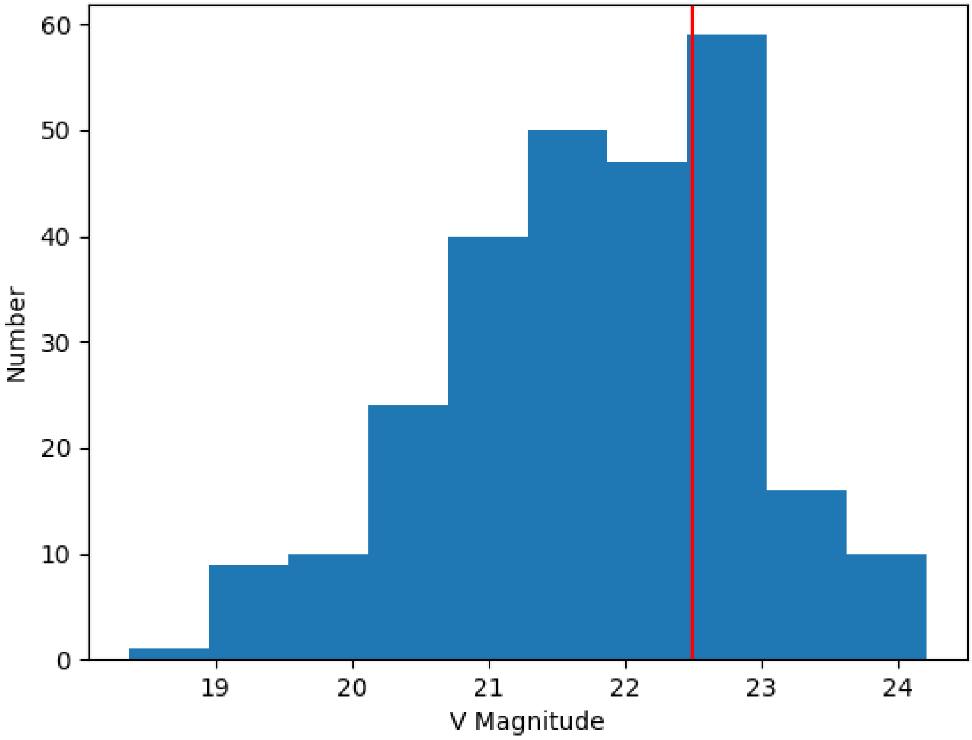

Figure 2.4: This plot shows V Magnitude against the number of targets in each magnitude bin. It contains all targets selected by FIMS in each of the 5 fields in the study. The magnitude cut-off of the survey of ~ 23.5 can be seen from the histogram. The vertical line shows the expected peak of a Gaussian GC luminosity function with $M_V = -7.5$

also cuts applied to the V and R magnitudes and the V-I and V-R colours, shown by the dashed lines in the plot. These restricted objects to magnitudes and colours where GCs are expected to be found. The plot also shows known galaxies denoted by the green dots and spectroscopically confirmed GCs in blue and red from Puzia et al. (2004) for comparison.

Using these criteria, the FIMS mask creation software was then used to create the masks for the observations. The targets had a designated priority based upon how closely they met the cut-off criteria or had other special features (ie previously untargeted object). FIMS uses this information, along with the location of the targets, to optimally select the most targets, with the highest priority, to place on the masks.

There were approximately 60 slits per mask and 5 masks in total. For the observations 1" wide slits were used with the 600B grism, it has a central wavelength of 465 nm, range of 330 - 621 nm and dispersion on 50Å/nm (ESO 2011a). The observations were taken over a wavelength range of 330-621nm (depending on the position of the slit) and had a resolution of ~4.8Å, full width half maximum (FWHM), with 1.2 pixels per Angstrom and a seeing of $\leqslant$ 1.0". Each field had a total exposure of 13,500s, split over 5 exposures of 2700s, apart from field 1 which had a total exposure of 10,800s split into 4 exposures of 2700s. The wavelength range covered by the observations varies slightly based on the positions of the slits on the mask. The selected range allowed coverage of some of the key absorption lines that can be used to determine metallicity, such as: G band (4304Å), Hβ (4862Å), Mgβ (5175Å) and Fe5270 (5270Å), as can be seen in Figure 2.7.

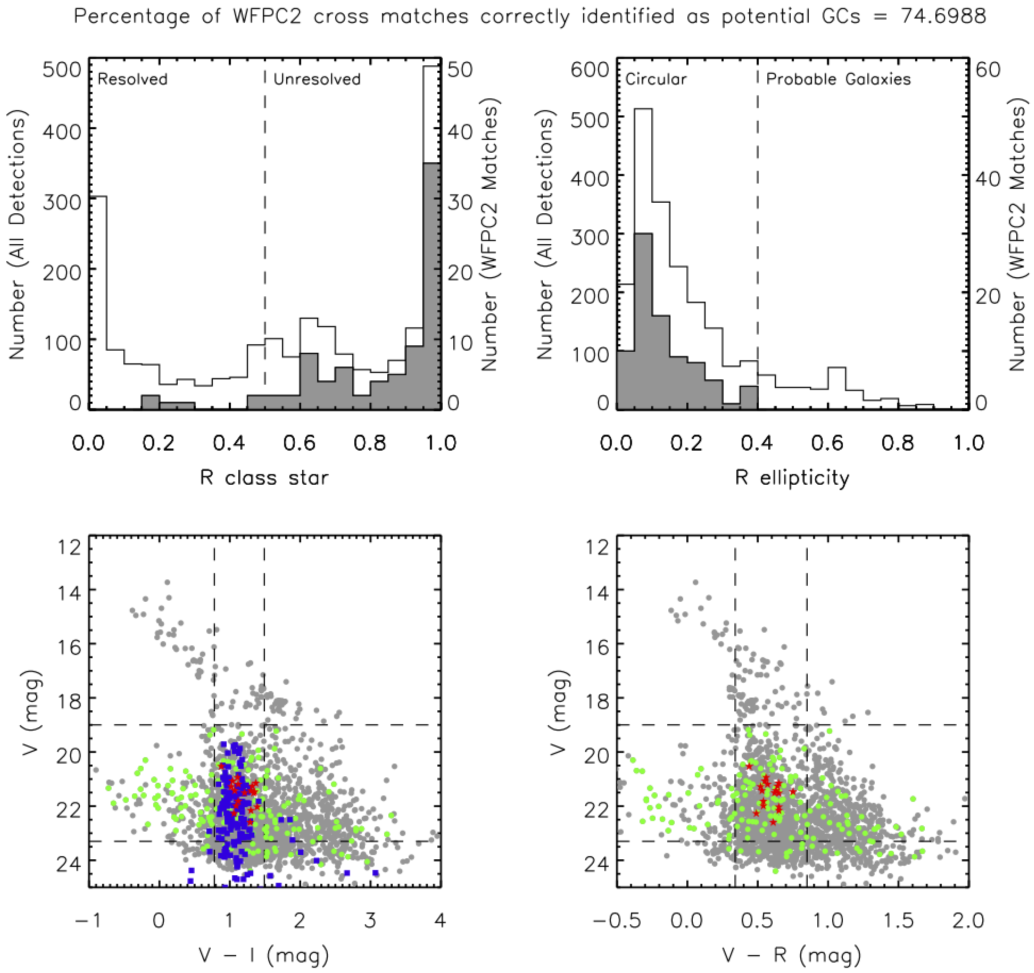

Figure 2.5: These four plots summarise the GC target selection process. For the pre-imaging the photometry was zero pointed to match the V, R and I data of Puzia et al. (2004). The top plots show the cut-off points based on the SExtractor star-galaxy separation parameter (Class Star) and ellipticity from the R photometry (from SExtractor). The ellipticity cut-off was less than 0.4 and the Class Star greater than 0.5, ensuring the sources were close to round and not too extended. WFPC2 imaging was used as a training set to help determine which objects were galaxies. The bottom plots show the cuts based on V magnitude and V-R and V-I colours, where the green circles are objects determined to be galaxies, based on WFPC2 photometry. and the blue and red points are spectroscopically confirmed GCs from Puzia et al. (2004).

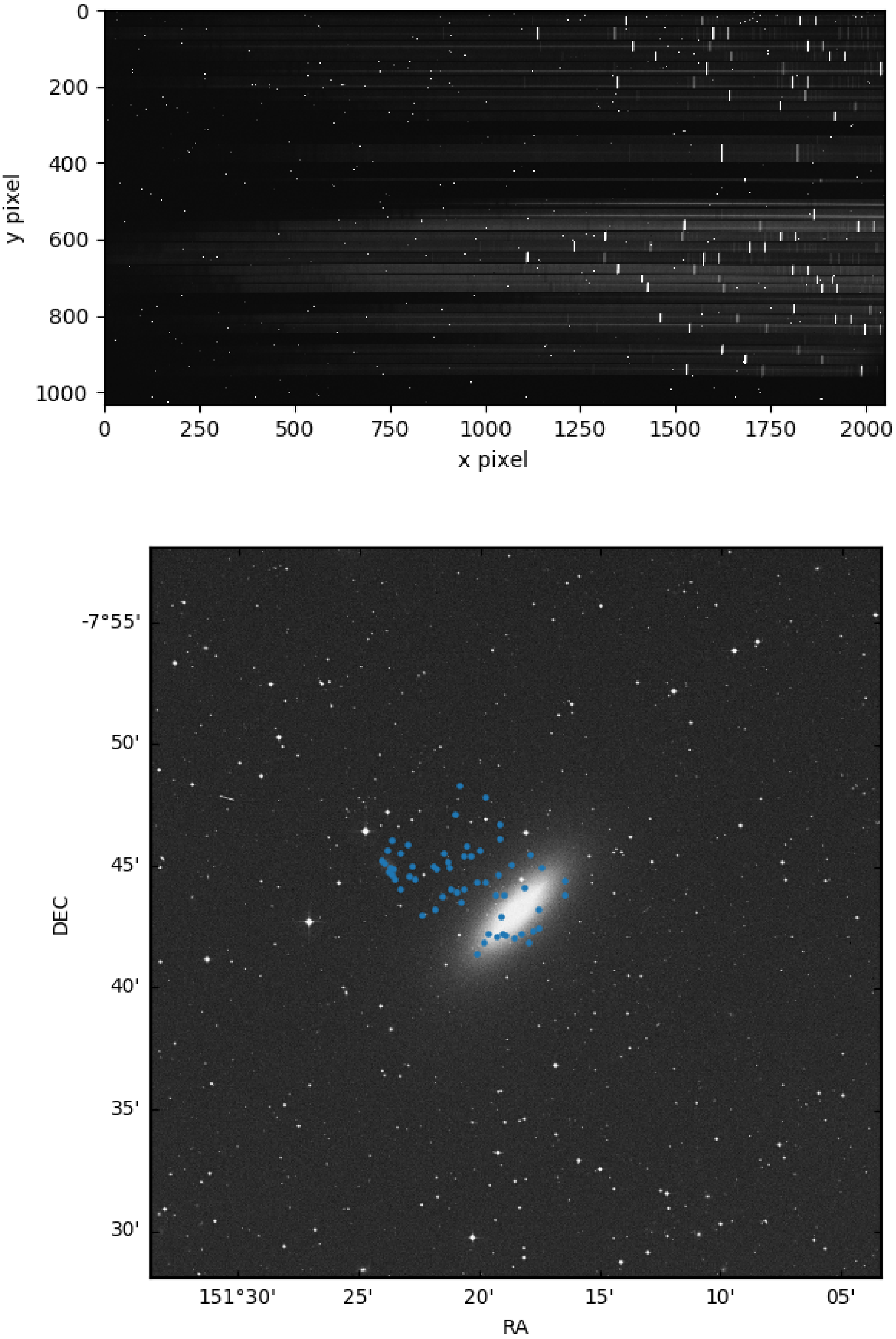

Figure 2.6: On the left plot is the position of targets of Field 5 overlaid on an image of NGC 3115. The right plot shows the MXU mask of the same targets and the differing length of the slits.

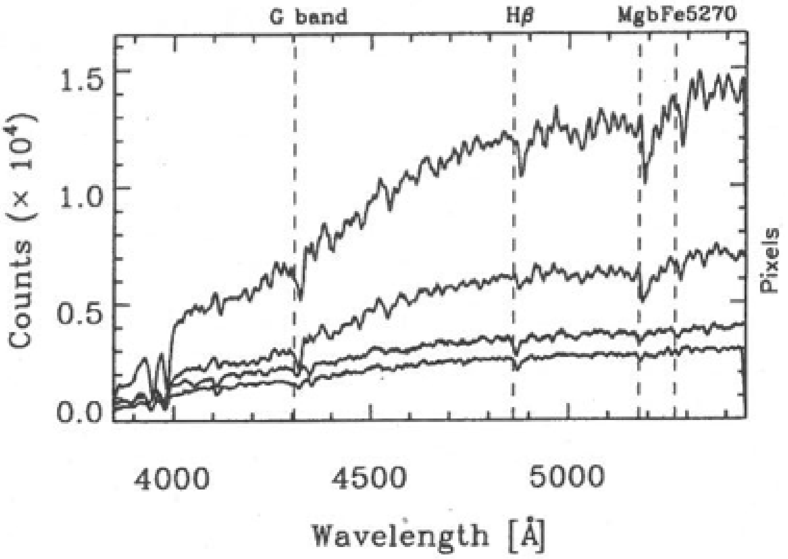

Figure 2.7: Sample spectra of NGC 3115 GC targets, of varying metallicity, from the 081.B-0633(B) observation of Field 1. Dashed lines show key rest wavelength absorption features. The redshift of the GCs is visible from the discrepancy between the rest wavelength and the location of the absorption features in the spectra.

2.3 Data reduction pipeline

In order to reduce the data, the ESO Reflex software was used, in conjunction with the FORS2 reduction pipeline (Freudling et al. 2013). This allowed the standard set of reduction steps to be completed with relative ease, along with the ability to check products of the reduction at each stage. Reflex (Freudling et al. 2013) is a graphical environment that allows a simple way of reducing VLT data, it is very similar to Esorex (ESO 2016) but automates the data organisation of each product created at every stage of the reduction. It is also interactive, and so parameters used in the reduction can be changed within the graphical environment. This means the effects of changing each parameter can be viewed before the data is completely reduced.

Firstly a master bias is created for each exposure automatically, it first finds the bias frames, which are provided with the observations, and the readout noise for each

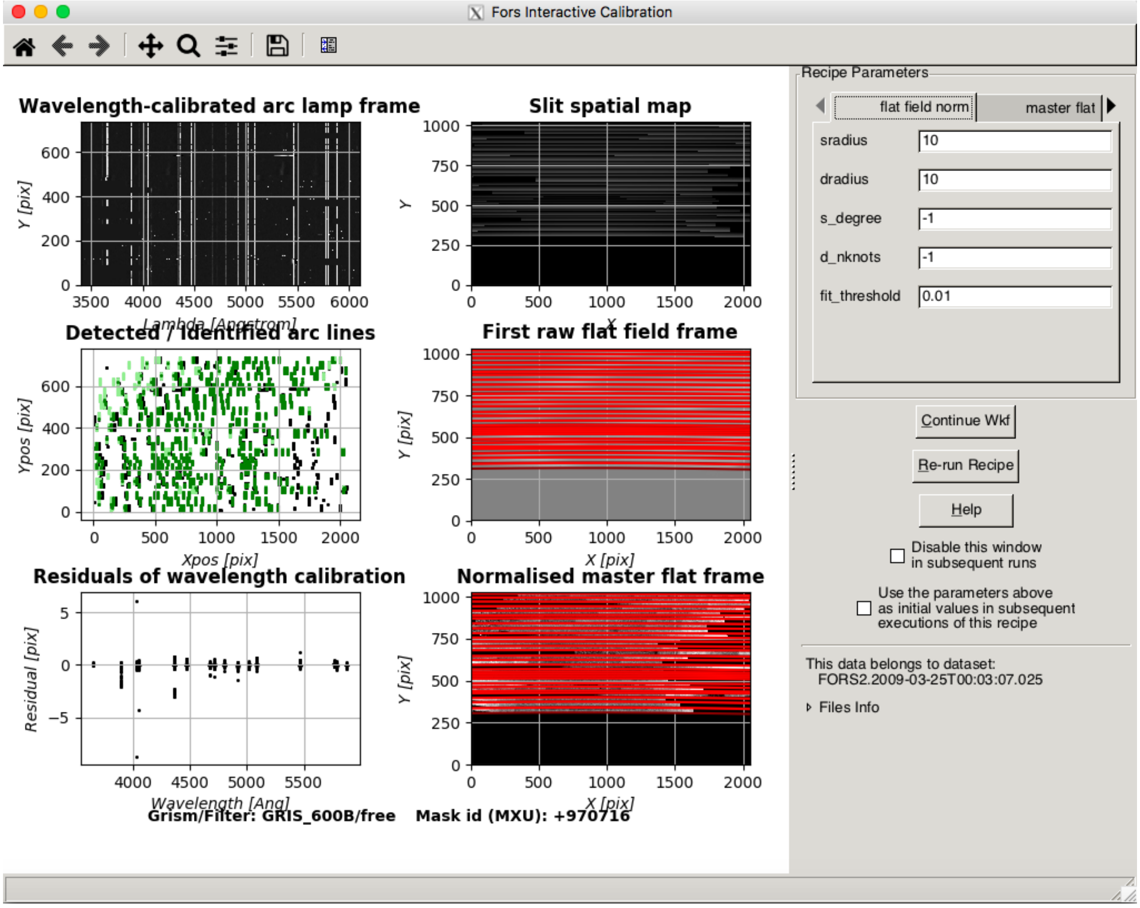

sradius 10

dradius 10

s_degree -1

d_nknots -1

fit_threshold 0.01

☐ Disable this window in subsequent runs

☐ Use the parameters above as initial values in subsequent executions of this recipe

This data belongs to dataset:
FORS2.2009-03-25T00:03:07.025

Figure 2.8: The FORS_CALIB interactive window where each section represents a different process step of the reduction. Top left shows the wavelength-calibrated arc lamp frame, centre left shows the positions of detected arc lines in the rectified frame and bottom left shows the residuals between predicted and detected arc line positions. The top right shows the slits positions in pixel values and the centre and bottom right are the raw and normalised master flat fields

frame is obtained from the standard deviation in each detector readout port. The master bias is produced by combining the bias frames using the median values and its error then appropriately propagated. This master bias is then subtracted from any of the raw files used in the pipeline. Reflex then begins the reduction by calling two procedures: fors_calib and fors_science. These procedures perform the bulk of the data reduction using interactive windows and are described in detail below.

2.3.1 FORS_CALIB

The fors_calib recipe first takes the grism table, arc lamp exposures, master bias, reference line catalogue and spectral screen flat exposures from the observation logs and downloads the relevant files using the ESO archive server. The recipe then identifies reference lines on the arc lamp exposure and fits a polynomial that maps the pixel space to wavelength space. In the case of this study, the lamps FlatBlue+4 and FlatRed+3 were used with the arc lines used for identification documented in Table 2.2. It then traces the edges of the spectra on the flat field, allowing the recipe to create a normalised flat field frame and the spectral extraction mask which is applied in the scientific data reduction. The spectra are also rectified using the arc lines to correct for the curvature of the spectra on the slits.

Figure 2.8 shows the fors_calib interactive window; in each panel a different calibration process is being shown. Top left shows the wavelength-calibrated arc lamp frame, there should not be any empty rows as that indicates an error in the detection of the arc lines. Centre left shows the positions of detected arc lines in the rectified frame and once again should not show any empty rows. Bottom left shows the residuals between predicted and detected arc line positions, for which the majority should be less than 0.5 pixels. Outliers are allowed so long as there is not a trend, and any badly fit lines can be added to an ignore list. The top right shows the slit positions in pixel values, which should not be curved or overlapping. Centre and bottom right are the raw and normalised master flat fields. The red lines indicate the edges of the slits and this, along with the area of each slit, should be the same in both panels.

Table 2.2: The master arc line catalogue used in fors_calib

Wavelength (Å)	Chemical Ion	Line set
3466.92	Cd I	standard
3611.69	Cd I	standard
3650.153	Hg I	standard
3888.643	He I	standard
4026.206	He I	standard
4046.563	Hg I	standard
4358.328	Hg I	standard
4471.501	He I	standard
4678.149	Cd I	standard
4713.173	He I	standard
4799.912	Cd I	standard
4921.931	He I	standard
5015.678	He I	standard
5085.822	Cd I	standard
5460.735	Hg I	standard
5769.363	Hg I	standard
5790.663	Hg I	standard
5875.663	He I	standard
6438.47	Cd I	extended
6678.152	He I	extended
7065.249	He I	extended

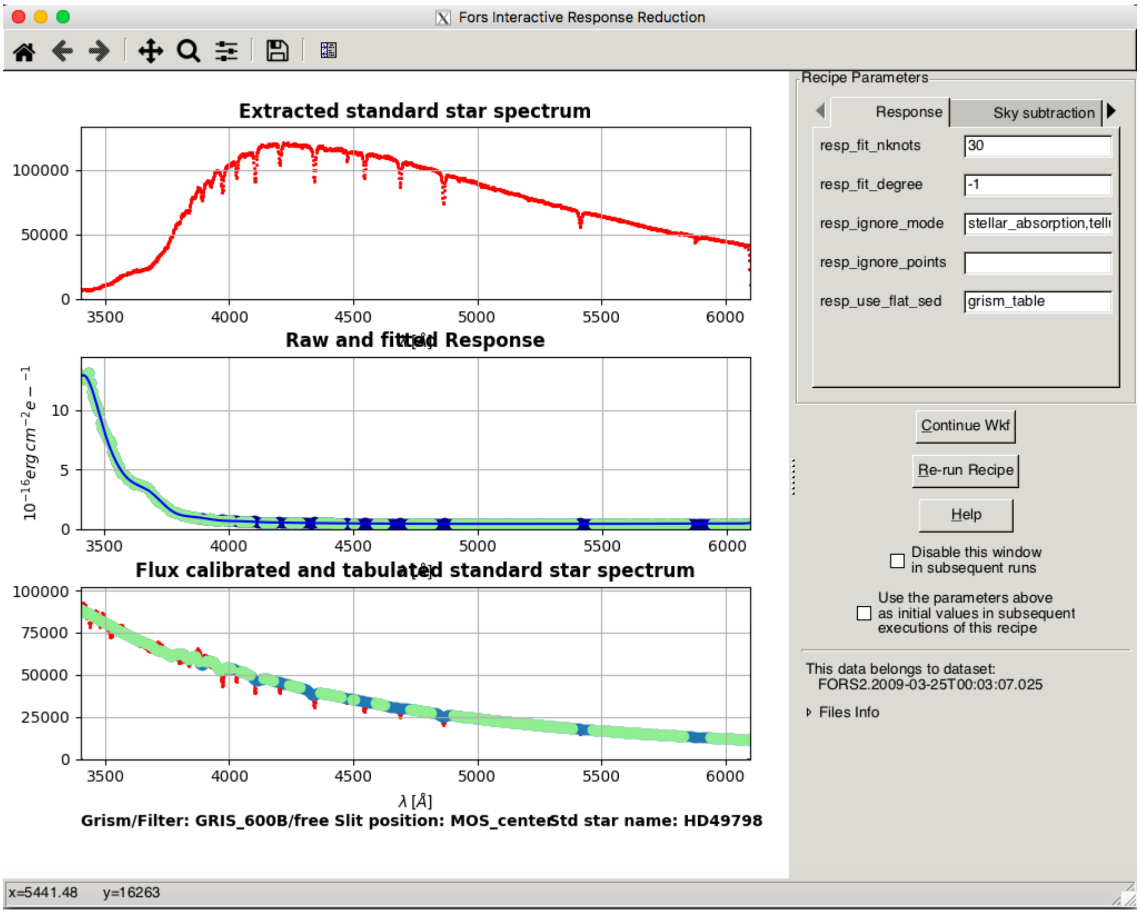

Grism/Filter: GRIS_600B/free Slit position: MOS_center Std star name: HD49798

resp_fit_nknots: 30
resp_fit_degree: -1
resp_ignore_mode: stellar_absorption,tell
resp_ignore_points:
resp_use_flat_sed: grism_table

☐ Disable this window in subsequent runs

☐ Use the parameters above as initial values in subsequent executions of this recipe

This data belongs to dataset:
FORS2.2009-03-25T00:03:07.025

x=5441.48 y=16263

Figure 2.9: This figure shows the interactive window for fors_science (response). The top panel is the extracted standard star spectrum, the centre panel shows the raw response (ratio of reference spectrum and observed spectrum integrated over same bins as reference spectrum) and fit. The bottom panel shows the flux-calibrated standard star spectrum and reference.

2.3.2 FORS_SCIENCE

The fors_science reduction is completed in two parts. The first is shown in Figure 2.9 and is the fitting of the spectrophotometric response curve using a standard star. This is done to account for any effect the response of the instrument may have on the shape of the spectra. Once the response has been calculated using a spectrophotometric standard, the correction can be applied to all the spectra obtained in the next stage of the recipe. At the top of Figure 2.9 is the extracted star spectrum. The centre panel shows the raw response (the ratio of the reference spectrum and observed spectrum integrated over same bins as reference spectrum) and the best fit, represented by the dots and blue line respectively. Finally, the flux-calibrated standard star spectrum and reference spectrum is shown in the bottom panel; the red line is the star spectrum after the response curve is calibrated while the blue and green is the reference data. Any discrepancy between the blue and green dots here represents an error in the wavelength calibration, whilst differences between the red and blue indicate errors in the inter/extrapolation.

Sky subtraction takes place with the spectral extraction, with each individual spectrum having the sky above and below the object sampled to create a sky spectrum. Figure 2.10 shows how the sky subtraction and spectral extraction has been performed. The top panel shows the mapped and sky-subtracted 2-dimensional spectrum, that has also been wavelength calibrated and rectified. Also indicated are the extraction limits of each spectrum, shown by the yellow and red lines. Each spectrum can be viewed in the bottom panel to check if the sky has been acceptably removed. Figure 2.11 shows a summary of the products that running FORS_SCIENCE produces and the definition for each, taken from the FORS User manual.

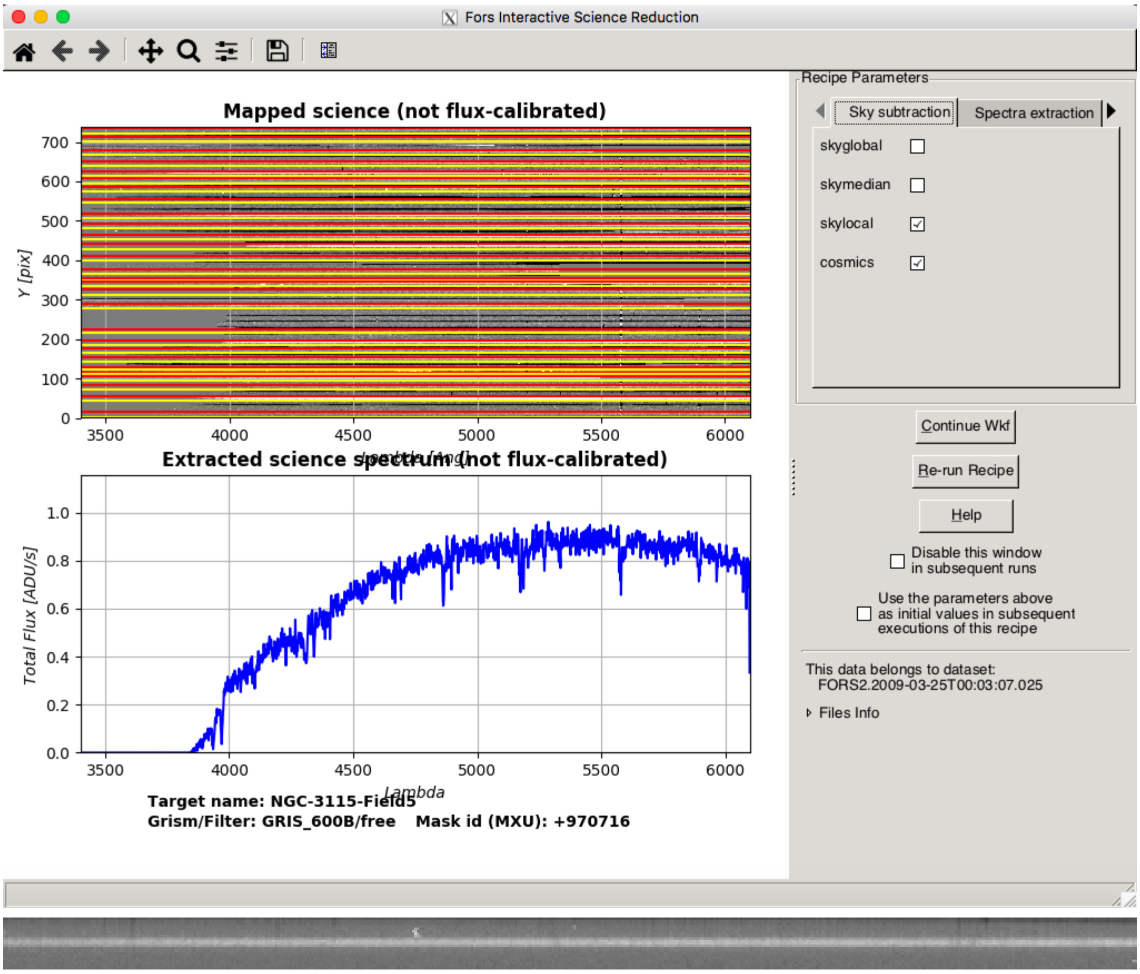

Target name: NGC-3115-Field5
Grism/Filter: GRIS_600B/free Mask id (MXU): +970716

skyglobal ☐
skymedian ☐
skylocal ☑
cosmics ☑

☐ Disable this window in subsequent runs

☐ Use the parameters above as initial values in subsequent executions of this recipe

This data belongs to dataset:
FORS2.2009-03-25T00:03:07.025

Figure 2.10: The FORS_SCIENCE interactive window where the top panel shows the mapped sky-subtracted 2-dimensional spectrum which has also been wavelength calibrated and rectified and the bottom panel shows the final 1d spectrum for a typical target. Underneath is a close up of an individual GC target as seen on the slit.

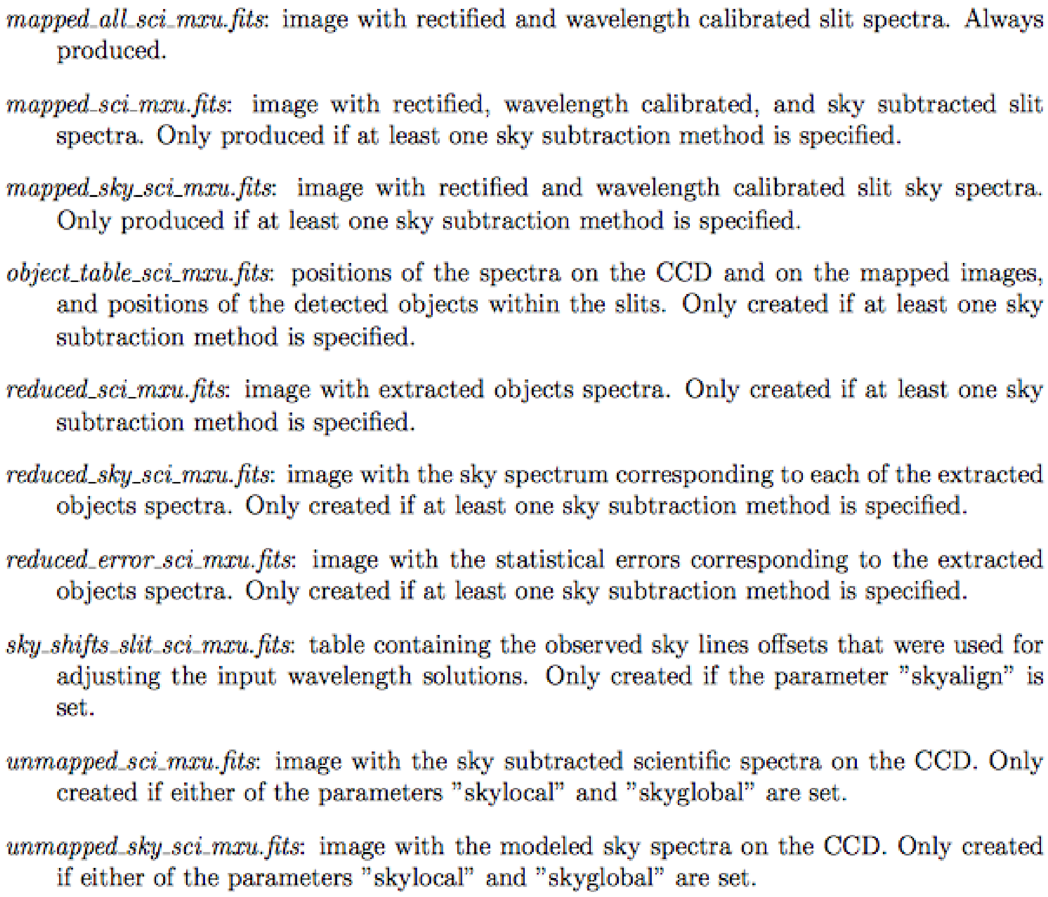

mapped_all_sci_mxu.fits: image with rectified and wavelength calibrated slit spectra. Always produced.

mapped_sci_mxu.fits: image with rectified, wavelength calibrated, and sky subtracted slit spectra. Only produced if at least one sky subtraction method is specified.

mapped_sky_sci_mxu.fits: image with rectified and wavelength calibrated slit sky spectra. Only produced if at least one sky subtraction method is specified.

object_table_sci_mxu.fits: positions of the spectra on the CCD and on the mapped images, and positions of the detected objects within the slits. Only created if at least one sky subtraction method is specified.

reduced_sci_mxu.fits: image with extracted objects spectra. Only created if at least one sky subtraction method is specified.

reduced_sky_sci_mxu.fits: image with the sky spectrum corresponding to each of the extracted objects spectra. Only created if at least one sky subtraction method is specified.

reduced_error_sci_mxu.fits: image with the statistical errors corresponding to the extracted objects spectra. Only created if at least one sky subtraction method is specified.

sky_shifts_slit_sci_mxu.fits: table containing the observed sky lines offsets that were used for adjusting the input wavelength solutions. Only created if the parameter "skyalign" is set.

unmapped_sci_mxu.fits: image with the sky subtracted scientific spectra on the CCD. Only created if either of the parameters "skylocal" and "skyglobal" are set.

unmapped_sky_sci_mxu.fits: image with the modeled sky spectra on the CCD. Only created if either of the parameters "skylocal" and "skyglobal" are set.

Figure 2.11: This shows the products of running FORS_SCIENCE and the definition of each as specified in the FORS User Manual. Taken from the FORS User Manual.

2.3.3 Verification of the FORS2 reduction pipeline

After the reduction pipeline has been run, the final 2-D spectra and some reference and calibration data are created. This allows the processes carried out in the pipeline reduction to be checked, to ensure they have worked as intended. The wavelength calibration can be checked in MAPPED_ALL_SCI_MXU, which shows the spectra after the removal of optical and spectral distortions. The wavelength calibration has been successful if the bright sky lines are straight and aligned vertically, as seen in Figure 2.12 (an analysis of this is found in Chapter 3). As mentioned previously, the sky subtraction can also be checked using the error spectra created. This is done by ensuring the residual noise is compatible with the statistical error associated to the extracted object spectra, as stated in the FORS2 data reduction manual (Izzo et al. 2012).

2.3.4 Final Data Processing

The 2-D spectra produced were split into individual files for further processing. This was accomplished using the *scopy* function in Pyraf (Pyraf is a product of the Space Telescope Science Institute, which is operated by AURA for NASA). The 1-D spectra were then identified using the object tables created during the reduction, so that they could be correctly co-added with other exposures from the same field. *Scombine* was used to combine the spectra, with average sigma clipping used to reject anomalous pixels. The spectra were then scaled and combined based on the median value. This produced the final 1-D spectra, that are used in the data analysis, an example of which can be seen in Figure 2.13.

From the initial target list of ∼280 slits, 244 reduced 1-D spectra were obtained (as seen in Table 1); leaving a large sample size to perform further analysis on. The loss of spectra is mostly due to the spectral extraction, as some objects were too faint

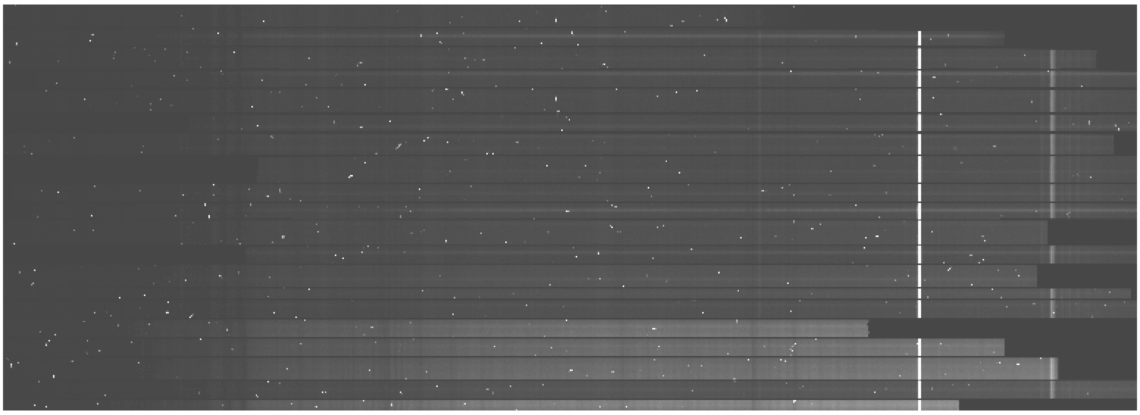

Figure 2.12: 2-D spectra of targets in Field 1, after wavelength calibration. Note the prominent sky lines visible towards the right side which can be used to check the wavelength calibration from the data reduction. Each of the lighter coloured rectangles correspond to a 2D spectrum extracted from one of the multi-slits shown in Figure 2.10.

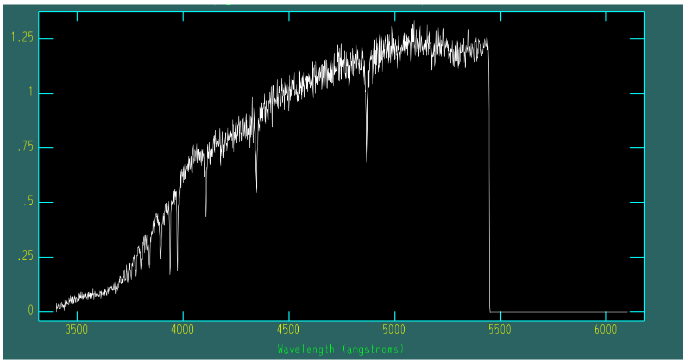

Figure 2.13: 1-D spectrum of a target in Field 3, displayed using the Python implementation of IRAF (Pyraf). This spectrum has been completely reduced and co-added to increase the SNR. The total exposure time for this spectrum was 13,500s. Units on the y-axis are in ADU per second.

to be detected by Reflex.

Chapter 3

Data Analysis and Model Fitting

There are two main methods for extracting metallicities from an integrated GC spectrum. These are the Lick/IDS line strength system and the full spectral fitting method. The Lick/IDS system is commonly used to measure the line strengths at optical wavelengths (Worthey et al. 1997; Trager et al. 1998). During 1972 to 1984 S.Faber and collaborators used the Image Dissector Scanner (IDS) to obtain spectra for many hundreds of stars in the Milky Way, creating a large library which was used to define the line strength system, originally containing 11 indices (Faber et al. 1985). This has more recently been updated to include more than 25 indices, including more age sensitive indices, such as Hδ and Hγ, by Worthey et al. (1997). The combination of the large number of indices, and range of stellar types within the library, have made the Lick/IDS system an important method for creating SSP models. It is then possible to compare obtained spectra to these theoretical SSP models in order to determine parameters such as age, metallicity and [α/Fe].

The full spectral fitting method can also be used to obtain properties of unresolved stellar populations, such as GCs (Foster et al. 2011; Lützgendorf et al. 2012; Lützgendorf et al. 2013). This method involves comparing spectra with grids of synthetic stellar population templates, of various ages and metallicities, and finding the best matching combination of templates. This enables ages and metallicities to be estimated from the observations. These templates are also convolved with a line-of-sight velocity distribution (LOSVD) to estimate kinematics from the spectrum.

3.1 Introduction to pPXF

In order to obtain kinematics and metallicities from the GC spectra in this study, the publicly available distribution of the Penalised Pixel Fitting Method (pPXF), developed by Cappellari and Emsellem (Emsellem et al. 2004; Cappellari 2017) was used. pPXF was chosen as it allows kinematics and metallicities to be easily extracted via the method of full spectrum fitting. It uses large numbers of template spectra to reduce the risk of template mismatch and, therefore, inaccurate results being obtained. pPXF fits the spectra in pixel space, using a maximum penalised likelihood approach, making it easier for the user to mask emission lines and bad pixels in the fit.

In order to produce the best fit spectrum, pPXF creates an optimal fitting template, for each input spectrum, formed by varying contributions from multiple user defined stellar population templates. Legendre polynomials are used to account for differences in continuum shape between the input spectra and the templates used. pPXF trials many LOSVD and, for each, a combination of templates is selected, using a linear least-squares method (Lawson et al. 1974), to create the optimal template with an associated set of template weights. These weights reflect the fraction of how much each stellar population template contributes to the optimal template, over the wavelength range. The goodness of fit for each trial is calculated via a χ^2 value and the template weights with the best χ^2 are used. From this, values for the kinematics, age and metallicity of the input spectra can be calculated, based upon the weights of the contributing templates.

3.2 Setup and use of pPXF

In order to use pPXF to obtain kinematics and metallicities using the data in this study, some modifications to the code in the public distribution had to be made. The new code created was checked using the examples given in the pPXF distribution, in order to ensure it worked as intended. The main change made was to ensure that the wavelength start and end points for each spectrum could be changed individually, based on where the number of counts were non-zero. Without this, pPXF produced incorrect results, as it was including invalid data in the fit, due to the nature of multi-slit spectroscopy.

In order to fit the data, 144 stellar population models from Vazdekis et al. (2010) were used as the template spectra. These models are from the Medium-resolution Isaac Newton Telescope Library of Empirical Spectra (MILES) (Sánchez-Blázquez et al. 2006). This library is used primarily as it covers the wavelength range of the spectra in this study (3525-7500Å), in addition to covering a large range of stellar ages (0.063 to 17.78Gyr) and metallicities ([M/H]=-2.32 to +0.22). These templates are based on the solar value of $[\alpha/Fe]$, meaning all metallicities extracted will be based on this assumption.

The use of pPXF was split into two parts (kinematics and metallicity) and separate scripts were created for each. When fitting for kinematics, the user is given the option of how many LOSVD parameters to fit for (mean velocity, velocity dispersion, h3 and h4). h3 and h4 are the Gauss-Hermite coefficients and represent the the skewness and kurtosis of the velocity distribution of the GCs. In the case of NGC 3115 GC spectra, obtaining even velocity dispersion is difficult. This is because the typical velocity dispersion of GC's are $> 10\text{kms}^{-1}$ which is too low to be resolved given the spectral resolution of FORS2. This was verified by testing in pPXF, which always returned a value of 1 kms^{-1}. Therefore only the mean velocity produced by pPXF will be given in the final results.

The majority of the code for these two implementations is the same, with key differences being the use of multiplicative legendre polynomials (instead of additive legendre polynomials) to account for the shape of the spectra, and the application of regularization, both of which are used in the metallicity implementation. When pPXF fits a spectrum, it assigns weights to each of the stellar templates used in the fitting and, in order to obtain meaningful values for metallicity using pPXF, these weights need to be regularized. This is because obtaining the star formation history (SFH), and therefore metallicity, from integrated spectra is an ill-posed problem (Engl et al. 2000; Cappellari 2017). Regularization in pPXF is performed using the $REGUL$ keyword, using equation (19.5.10) of Press (2007).

For each spectrum an appropriate value for $REGUL$ had to be obtained and the method for doing so is set out in the documentation for pPXF. The basic process is as follows:

- Perform an unregularized fit ($REGUL$=0)
- Re-scale the NOISE spectrum so that $\chi^2/N_{DOF} = 1$. This is done in Python by NOISE = NOISE*sqrt(pp.chi2).
- Iteratively change $REGUL$ until $\Delta\chi^2 = \chi^2 - \chi^2_{unregul} = \sqrt{2 \times len(goodPixels)}$

In order to decrease the amount of computation time needed to perform this process, the input GC and noise spectra, along with the template spectra, were normalised. This forced the range of values $REGUL$ could take to be similar in all spectra, and typically two orders of magnitude lower than the counts values. The value obtained for the regularization using this method is the the maximum that enables the SFH to be the smoothest (minimum curvature or variation) but still consistent with the data (Cappellari 2017). Once each spectrum has an associated value for $REGUL$, pPXF was then used to obtain kinematics and metallicity values for each spectrum. The value obtained for velocity was checked against the version of the code that did not use *REGUL*, to ensure that pPXF was working as intended, as the kinematics result should not be overly reliant on the regularization, as found in testing.

In order to ensure that the results would be reliable, and comparable to other studies, different cut-off points were selected for the minimum SNR for kinematics and metallicities. The signal to noise ratio was calculated for each pixel and then averaged over the entire spectrum. For kinematics a SNR ≥ 6 per pixel was chosen and for metallicities it was set higher at a SNR ≥ 10 per pixel. This ensured that the errors obtained weren't too large as to make the results unusable. Errors were calculated using a Monte Carlo approach (Newman et al. 1999). Each spectrum had an additional noise spectrum created using the combined errors of read-out noise, Poisson noise and sky noise. Using this, the spectra were randomly redrawn, for each trial, and fit 200 times. Values for mean velocity and metallicity were obtained; taking the standard deviation of these values gave the 1 σ error in these parameters.

3.3 Reliability of results

When fitting using pPXF, the option to display the fit is given. This gives an opportunity to inspect the goodness of fit by eye, although it shouldn't be used to discount a target without additional reasons. It has however, provided a useful tool to inspect whether the results given by pPXF are realistic, based on whether the optimal template produced fits the absorption features of the input spectra. This section will show some examples of fits to the data before providing the final results of the data analysis.

In Figure 3.1 there are two fits to the same spectrum. The top plot was obtained after running the kinematics code and therefore the *REGUL* option of pPXF is turned off. The bottom plot shows the fit of the same spectra where *REGUL* is used. From the figure it is possible to see that the bottom plot seems to better fit the absorption features depth, indicating a more reliable obtained value for the metallicity of the target.

In some spectra is was not possible for pPXF to accurately fit the spectra and the causes of these problems are not always obvious. However, there were some common features when pPXF could not perfectly fit a spectrum. In Figure 3.2 we see a star that has contaminated the data set, due to the usage of SSP models for the pPXF fitting the absorbtion lines are not correctly accounted for.

In order to see if the results obtained are reasonable and believable, some checks were carried out. Firstly the SNR was plotted against the V magnitude of the targets observed, from Figure 3.3 we can see that as magnitude increases the SNR decreases, which is what we would expect. In Figure 3.4 the SNR has been plotted against velocity error (from pPXF), this allows us to see if the the size of the errors increases as the quality of the spectra decreases. Indeed we can that this is the case for the majority of the targets, there are some outliers with very large errors, which may indicate a problem with those specific spectra. This plot can also be used to see if the kinematic SNR cut-off is appropriate. As can be seen in the plot, once the SNR gets to 5-6 the numbers of large errors is increasing and so it would not make sense to decrease the cut-off as the velocities would become meaningless.

Figure 3.5 shows the SNR plotted against the pPXF obtained metallicities. Generally it follows the same trend as with the kinematics with lower SNR meaning a larger error. There are some spectra that have suspiciously low error for a low SNR, potentially indicating a problem with obtaining the errors from pPXF in certain spectra. In Figure 3.6 the scatter on the 5577 Åline, from Field 1, is shown. This gives an indication of the accuracy of the wavelength calibration performed during the data reduction process.

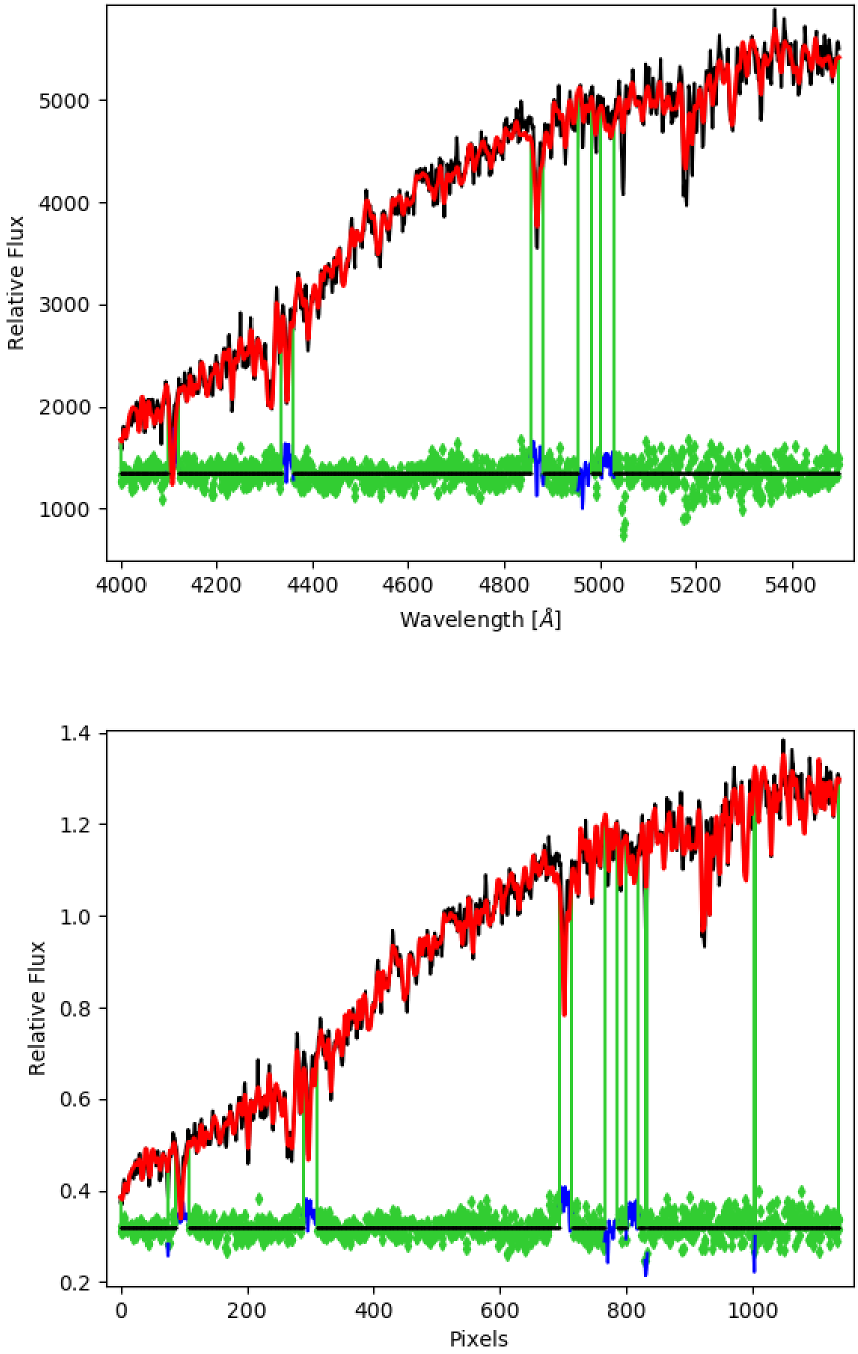

Figure 3.1: A GC spectrum from Field 5 (Object ID 5_47). Top panel shows the fit using the kinematics implementation of pPXF. The bottom panel shows the fit using the metallicity implementation in which the depth of the absorption features are clearly better incorporated. In each plot the the black line is the original observed spectrum and the overplotted red line is the best fit spectrum created by pPXF. The green dots are the residuals from the fitting process, the green vertical lines and blue lines show areas of large residuals from the fit and the difference between the spectra and the model.

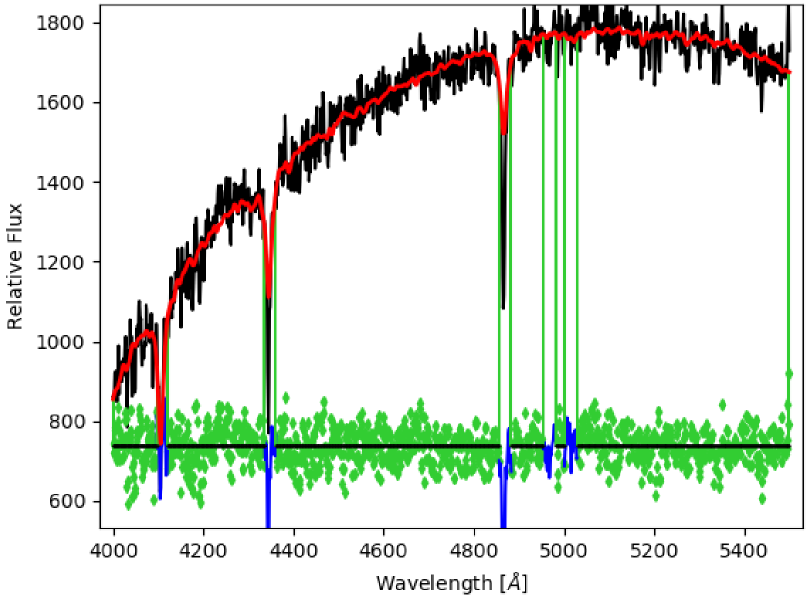

Figure 3.2: A star spectrum from Field 5 (Object ID 5_27) with incorrect fitting. This is because the models used are for SSPs and therefore do not account for single hot stars.

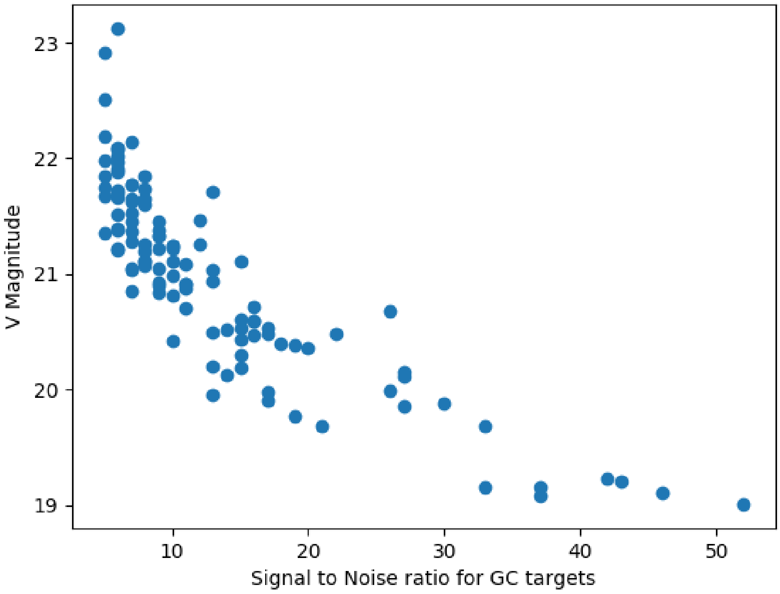

Figure 3.3: This plot shows the SNR and the V magnitude of all the GC targets for which kinematics could be extracted. As would be expected there is the general trend that as the magnitude increases the SNR decreases.

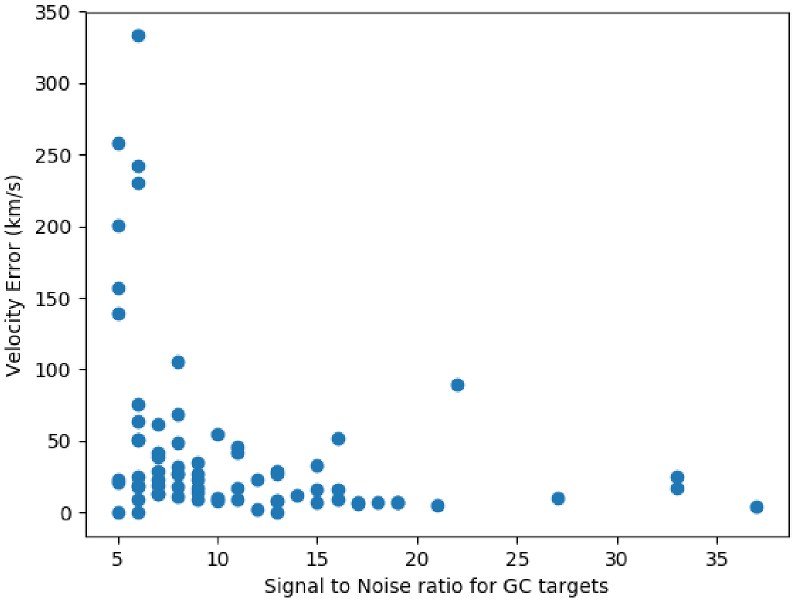

Figure 3.4: In this plot the SNR and the error from the pPXF velocities are shown. The errors increase in size with decreasing SNR and begin to get much larger as the cut-off SNR is reached. This therefore shows that the cut-off SNR is appropriate and going to lower SNR would not yield any useful results.

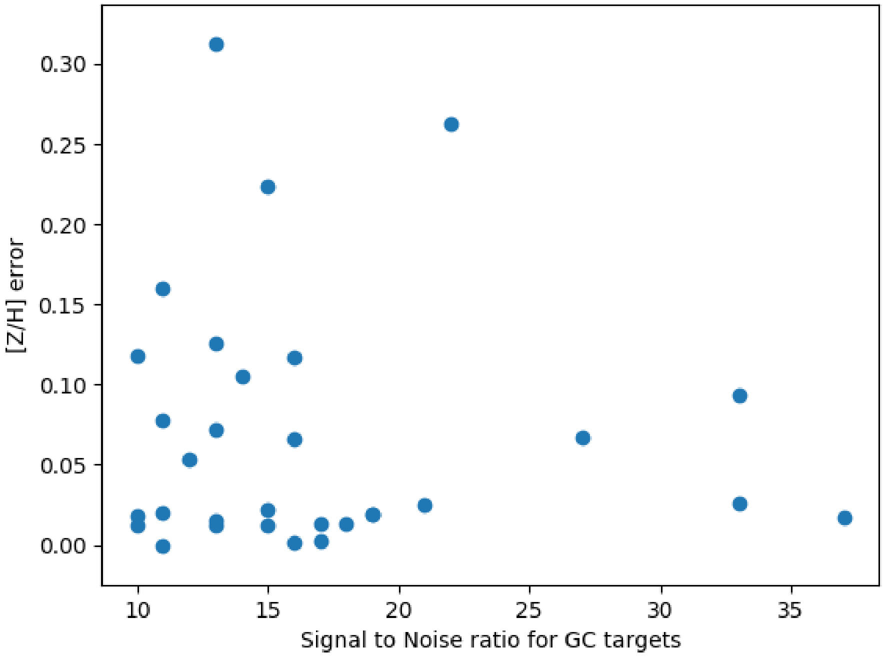

Figure 3.5: In this plot the SNR and the error from the pPXF [Z/H] errors are shown.

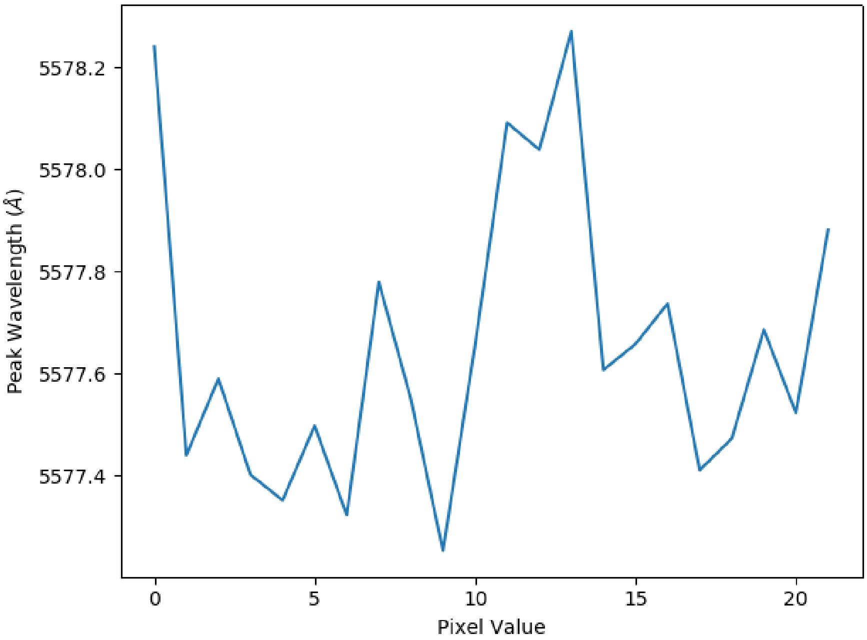

Figure 3.6: This plot shows the scatter in the sky line at 5577Å in one of the slits after the data reduction process has taken place.

3.4 Results of the data analysis

The final results for velocities and metallicities obtained from the pPXF fits are shown in Appendix A, Table 2 and a subset of the results are shown here, in Table 3.1. In order to improve the fits it may be possible to include more templates, 144 templates were used but there is the option to add more from the MILES database. However, based on other studies in the literature, this number of templates should be sufficient for the majority of cases.

Table 3.1: Table of GC targets listing: Object ID, SNR, Velocity, Velocity Error, metallicity and metallicity error obtained from pPXF. Complete table given in Appendix A.

Object ID	SNR	Velocity	Vel error	[Z/H]	[Z/H] error
1_12	37	187	3	-0.43	0.07
1_14	6	1074	242		
1_15	5	484	23		

Object ID	SNR	Velocity	Vel error	[Z/H]	[Z/H] error
1_19	21	1127	5	-0.19	0.08
1_21	7	992	29		
1_22	8	476	69		
1_24	9	223	223	-0.79	0.13
1_25	9	822	14	-0.21	0.07

Chapter 4

Results and Analysis

From the initial 266 GC candidate targets, 111 had a high enough SNR to extract kinematics and 67 passed the threshold for useful metallicity determination. At the distance of NGC 3115, it is difficult to ensure that only GCs are detected using purely photometric (image size and shape) data. To ensure that the sample was not contaminated with background galaxies or foreground stars, a velocity cut was therefore imposed. NGC 3115 has a heliocentric radial velocity of 663 [±4] kms^{-1} (Tonry et al. 2001; Paturel et al. 2002). Using this, and the velocity cut from Kuntschner et al. (2002), our sample therefore contains objects with radial velocities between 200 kms^{-1} and 1300 kms^{-1} (including errors). After this cut, there are 69 remaining candidates with velocities and 31 with metallicities, the locations of which can be seen in Figure 4.1. Therefore, 65% of the candidates, with SNR greater than 6 per pixel, were deemed dynamically associated with NGC 3115.

Using these remaining targets, a V-I vs V colour-magnitude plot was produced, along with a colour histogram (see Figure 4.2). The cut off between the red and blue GCs is the mean value of the full HST sample from Kundu et al. (1998), given as (V-I) = 1.06. These plots show that there is an excess of red GCs, and we would therefore expect the metallicity results to reflect this as colour and metallicity are

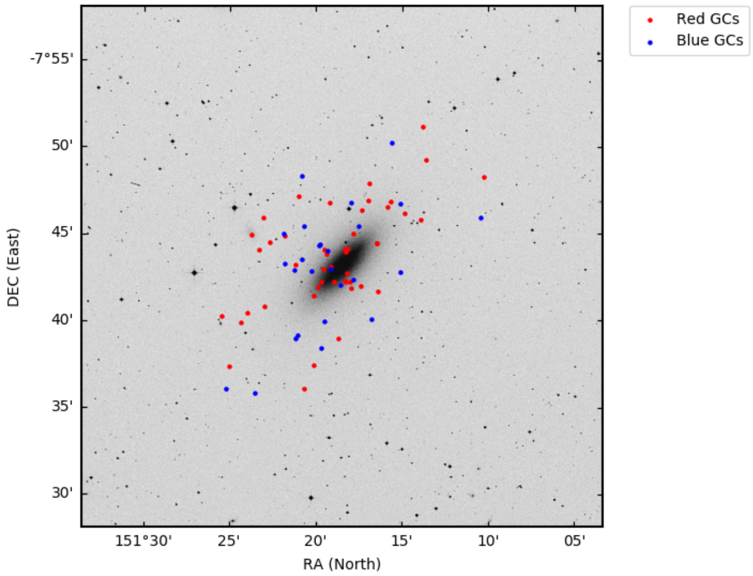

Figure 4.1: The positions of the red and blue GC targets, after the velocity cut, are shown overplotted on an image of NGC 3115. North is to the bottom of the image and East is to the left.

clearly linked in GC populations (Barmby et al. 2000; Kundu et al. 2007; Spitler et al. 2008). Of the final 69 targets, 47 were classified as red GCs and 26 as blue GCs. There is, however, no obvious bimodality in the colours of the target population (as seen in Figure 4.2), although the low number of GC targets may be a cause of this.

4.1 Kinematics of NGC 3115 Globular Clusters

The 69 radial velocities are obtained from GCs at various projected galacto-centric radii (see Figure 4.3). The confirmed GCs have an average distance of 10.6 kpc, compared with the average of all the initial GC targets of 12.9 kpc. The majority (74%) of the targets for which kinematics could be extracted are found within 15 kpc. The average velocity of the GCs is 602 [±29] kms^{-1} which agrees with the observed radial velocity of NGC 3115, to within the errors. A histogram showing the velocity distribution of the targets can be seen in Figure 4.4. Taking the recessional velocity

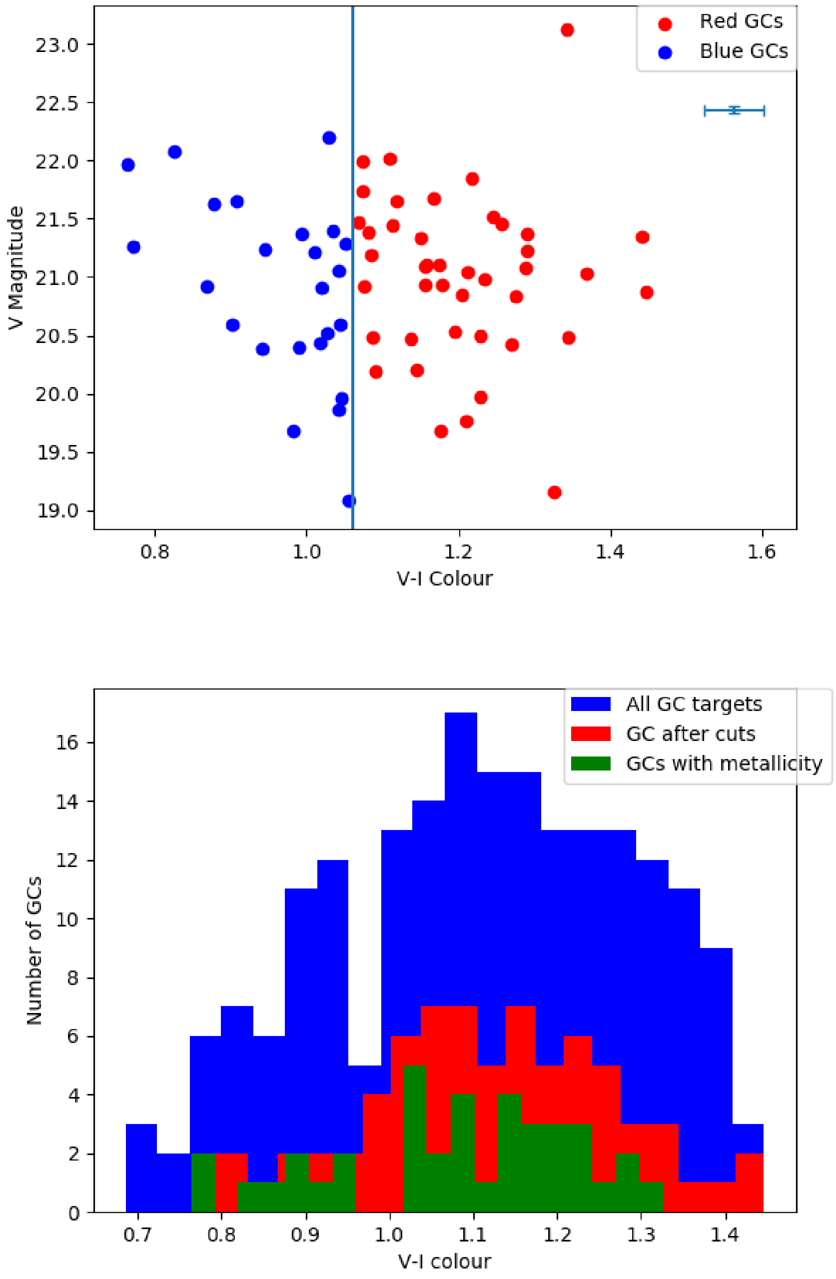

Figure 4.2: Both plots contain the GC targets with V-I less than 2.00, there is one target off the plot with V-I = 2.58. The top plot shows the blue and red clusters, plotting V magnitude against V-I colour. The cut off between blue and red colour comes from Kundu et al. (1998) and is given as (V-I) = 1.06. There is also a representative error in both the magnitudes and colours underneath the legend. The bottom plot is three histograms showing the colour distribution for the GC targets at different stages of the selection process.

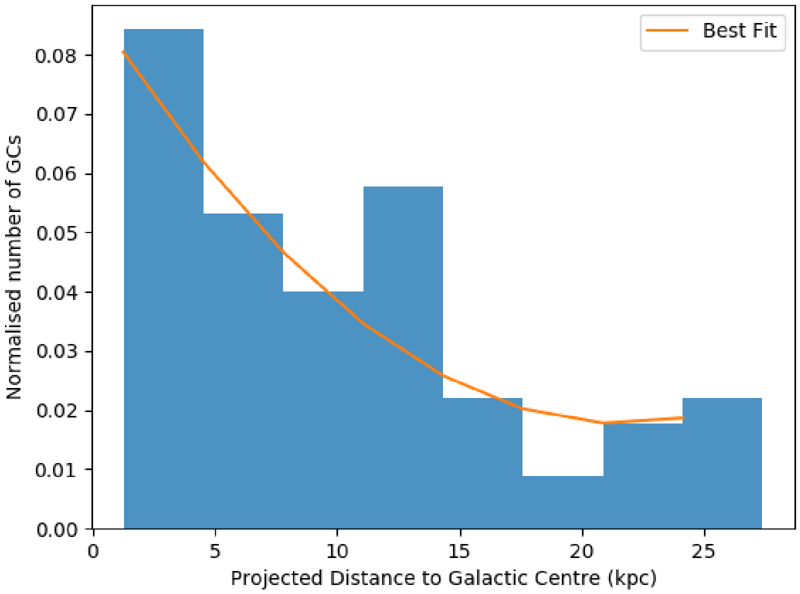

Figure 4.3: Histogram showing the projected galacto-centric distance for all the GC targets that could have kinematics extracted and lie within the velocity range expected for GCs associated with NGC 3115. 74% of the targets lie within 15 kpc of the galactic centre.

of the GCs to be that of NGC 3115 (663 kms^{-1}), the velocities relative to the system were obtained.

The results for the kinematics were matched with data from other studies in order to examine the reliability of the obtained results. They were first matched with the data from Kuntschner et al. (2002), but none of the their GC targets were covered in the final dataset of this study. The GC targets were then matched with the SLUGGS survey, using the positions from Arnold et al. (2011), which returned 22 matches. GC targets were deemed a match if the separation between the positions was less than 2 arcseconds; for these 22 matches the average separation was 1.05 arcseconds. The error bars for the present study are larger than that of the SLUGGS results, due to the lower SNR of the spectra. Overall however, there is a good correlation between the velocity data sets as seen in Figure 4.6. The average offset between the two datasets is 31.3 kms^{-1}, with none higher than 87 kms^{-1}. The dataset was also compared with Puzia et al. (2004), for which there was a single match. Puzia et al.

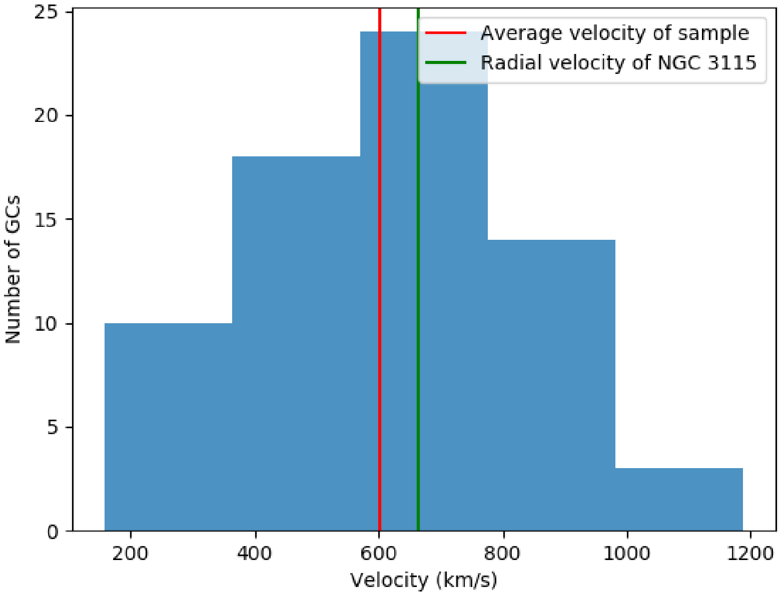

Figure 4.4: Histogram showing the distribution of velocities for the confirmed GC targets in NGC 3115. The average velocity is 602 ±29 kms^{-1}, as shown by the red line, and a standard deviation of 245 kms^{-1}. The overplotted line green line shows the radial velocity of NGC 3115

(2004) find a velocity of 957 kms^{-1} compared to 912 ± 19 kms^{-1} from this study, however no error is given for their value.

4.2 Metallicities and Ages

The targets for which metallicities were obtained came from similar projected distances as the kinematics, as seen in top plot of Figure 4.7, with $\sim 77\%$ coming from within 15 kpc. Despite only containing 31 GCs, there appears to be evidence of a bimodal population in the bottom plot of Figure 4.7. This plot also shows a reflection of the colour distribution, with more metal-rich clusters present in the sample than metal-poor clusters, which is to be expected if there is a higher number of red clusters. In Figure 4.8 the colour-metallicity relationship for the target clusters can be seen, along with the best fit line and the relationship found by Kundu et al. (1998)

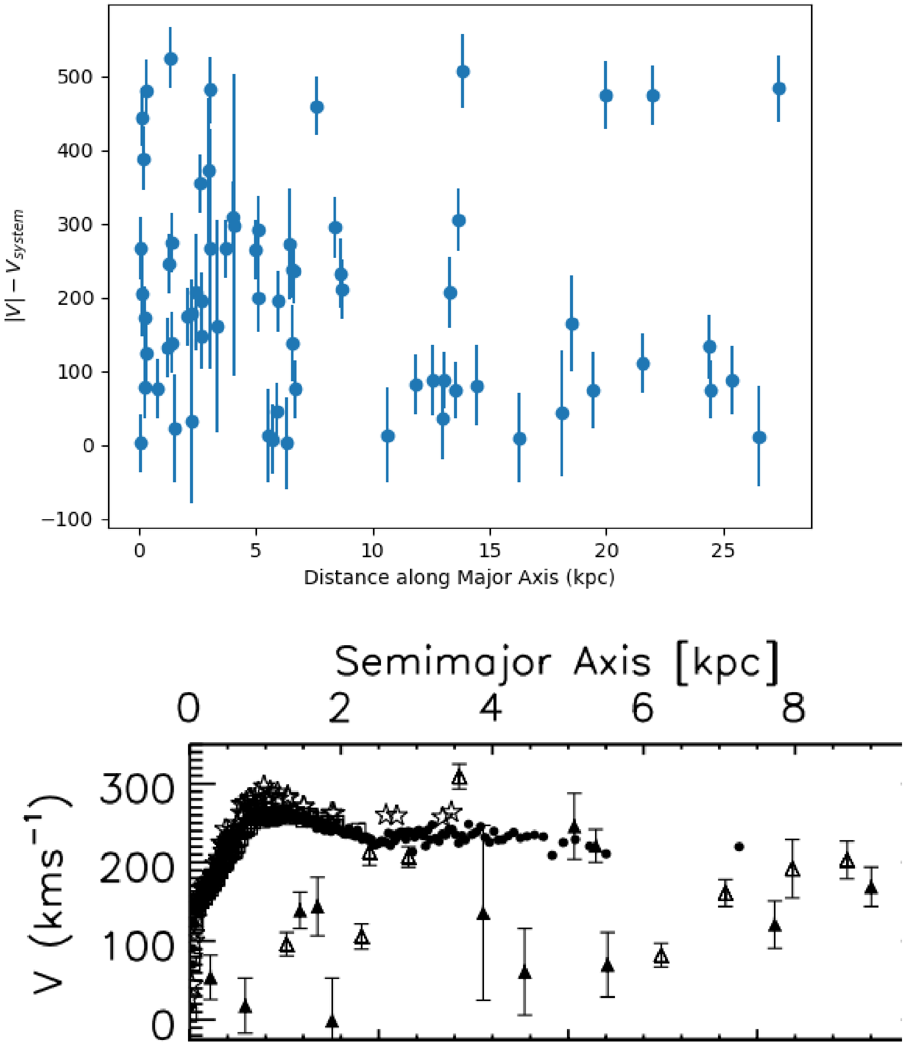

Figure 4.5: The top plot shows the absolute velocities obtained for the GC targets from this study where the major axis data has been mirrored about the minor axis. The velocities are δV having had the NGC 3115 system velocity of 660 kms^{-1} subtracted. The bottom plot shows the rotation curve of the bulge and disk of NGC 3115. Filled circles are from Norris et al. (2006), asterisks from Bender et al. (1994) and squares are from Fisher (1997). The filled triangles are blue GCs and unfilled triangles are red GCs both from Kuntschner et al. (2002). Taken from Norris et al. (2006).

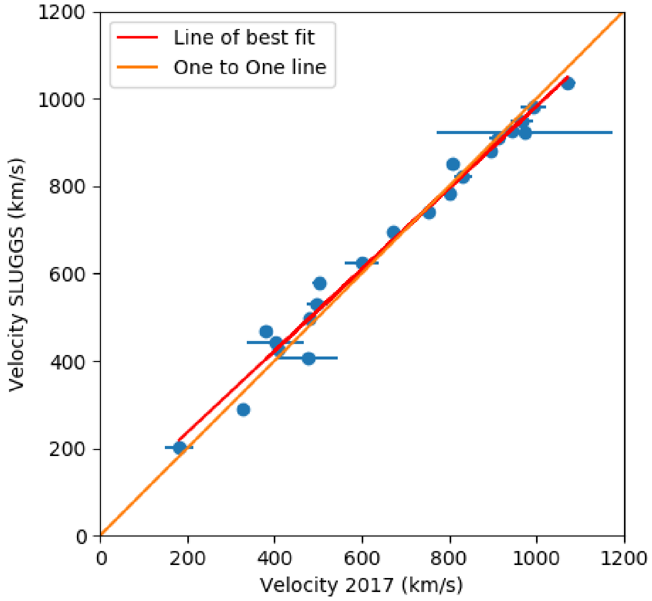

Figure 4.6: This Figure shows the velocity comparison between the dataset of this study and that of Arnold et al. 2011, along with a line of best fit between the two datasets. There is an average offset of 31.3 kms^{-1} between the two datasets.

for NGC 3115. Figure 4.9 shows the metallicity gradient for the GC targets. The top plot shows both the blue and red clusters from our sample, whereas the bottom plot shows the mean [Z/H] for GCs within radial galacto-centric distance bins. The metallicity gradient has a downward trend with increasing distance, which would be expected if the metal-poor clusters reside predominantly in the galaxy's halo.

Unfortunately, when attempting to compare the metallicity data with that of other studies, only 3 targets could be matched. These targets were observed in the SLUGGS survey and the comparisons are in Table 4.1, with 2 of the 3 agreeing within the errors. However, such a small sample size is not sufficient to establish whether the two studies agree overall. Figure 4.10 shows a comparison between this study, SLUGGS and the data from Kuntschner et al. (2002), for the metallicity distributions of each studies GC targets. Although it should be noted that the Kuntschner et al. (2002) sample is limited in size, the datasets show similar features for the metallicity distribution, with both this study and SLUGGS having a deficit

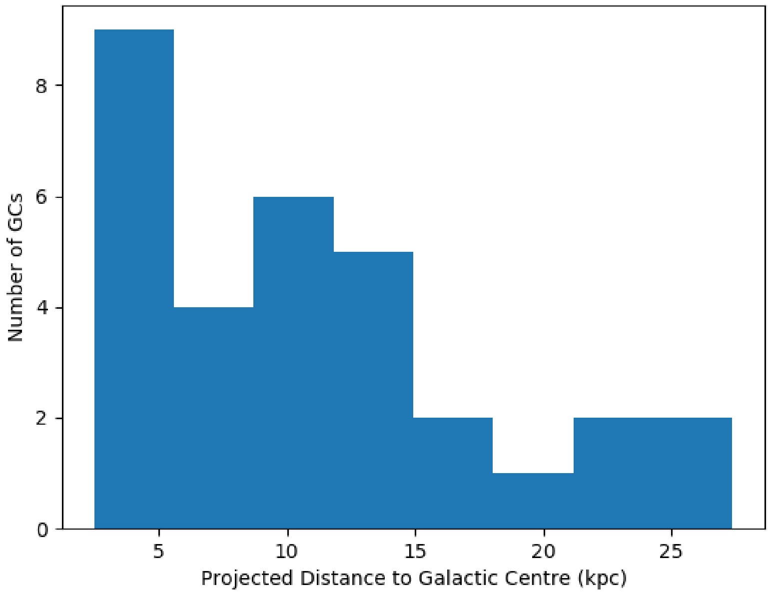

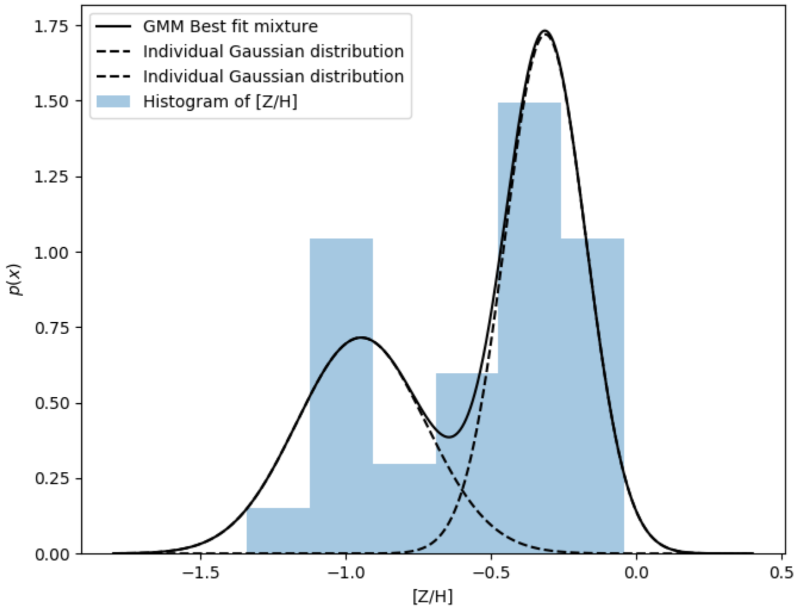

Figure 4.7: The top histogram shows the projected galacto-centric radii of the targets for which metallicities could be extracted. The bottom histogram is the metallicity distribution for the targets in the dataset for this study. There is an indication of a bimodal population, although the number of targets is not high enough for this to be strongly confirmed. A Gaussian Mixture Method (GMM) profile is plotted over the histogram.

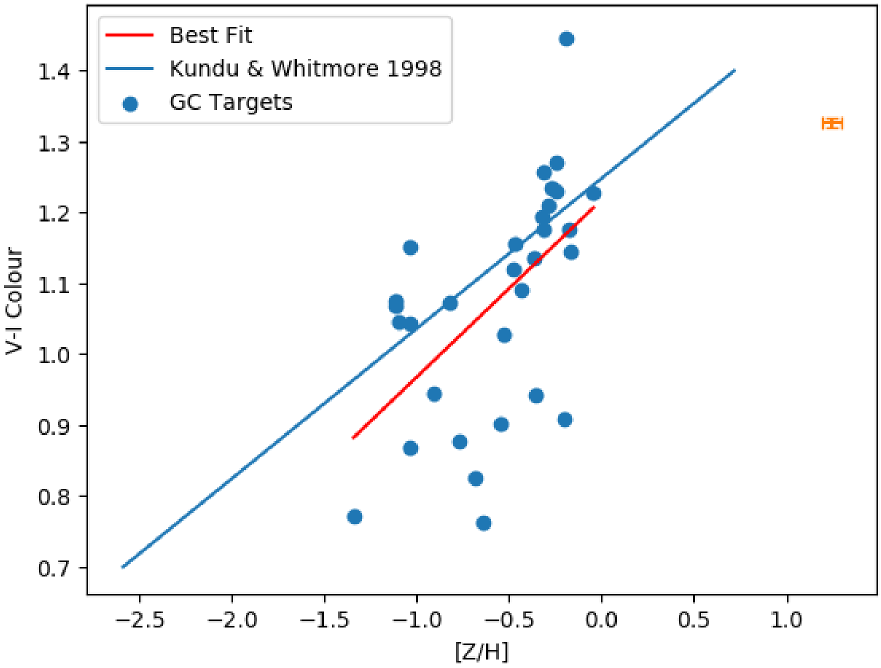

Figure 4.8: This plot shows the colour vs metallicity for each object with a high enough SNR. Overplotted is the best fit line for the data along with the line found by Kundu et al. (1998) for NGC 3115.

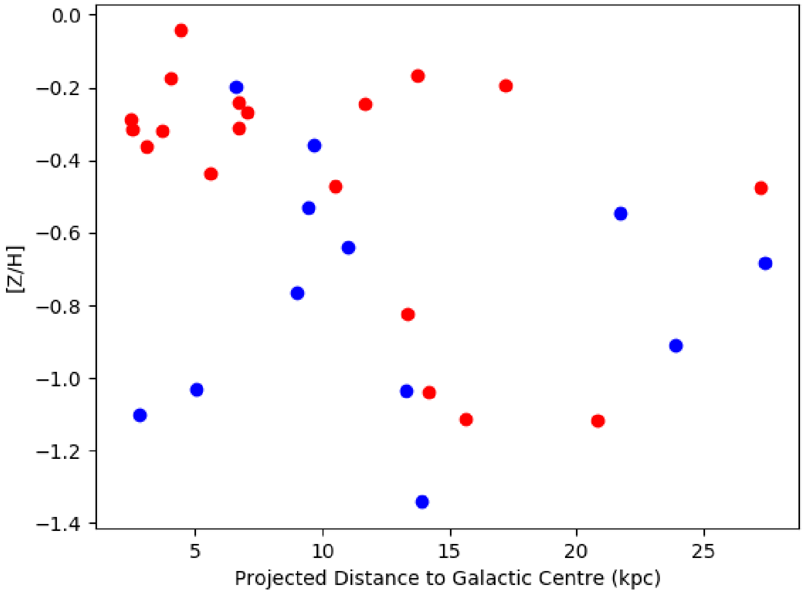

Figure 4.9: This plot shows [Z/H] against galacto-centric distance for the red and blue clusters. From the graph we can see there is some overlap between the red and blue clusters in the metal-poor and metal-rich areas.

Target ID	[Z/H]	[Z/H] error	SLUGGS ID	[Z/H]	[Z/H] error
2_47	-0.043	0.072	GC109	-0.03	0.12
2_52	-0.27	0.073	GC12	-0.01	0.31
2_53	-0.53	0.127	GC14	-0.94	0.14

Table 4.1: Table showing the comparison between the matched targets in the GC metallicity dataset of this study and that of the SLUGGS survey.

in the number of GCs in a similar location ([Z/H]=-0.5 to -0.8).

As previously noted in the dataset from this study, we find a higher number of metal-rich (21) than metal-poor (10) clusters, when taking [Z/H] = -0.7 to be the cut-off between the two populations. In the SLUGGS survey this population bias does not appear to be present, and from their sample there are 62 metal-rich clusters to 61 metal poor clusters. This suggests that the relative number of metal-rich to metal-poor clusters may be spatially dependant, given that the present study has a higher average distance from the galactic centre than in the SLUGGS survey (11.1 kpc compared to 9.0 kpc).

Age estimates are more difficult to obtain from spectra using pPXF, as they require an even higher SNR in the spectra for reliable results. However, age estimates were obtained for those spectra which met the same criteria as the metallicity sample. Figure 4.11 is a histogram that shows the frequency of the obtained ages, in which the majority of the spectra fall between 9-10 Gyr (29/31 GCs). Given that this sample contains both metal-rich and metal-poor clusters, it might be expected that there would be a some difference in ages if multiple GC formation events had occurred. The ages of the clusters against their galacto-centric distance can be seen in Figure 4.12, from the plot there doesn't appear to be a difference in age based on the distance from the galactic centre. In Kuntschner et al. (2002) they find the two GC sub-populations to be coeval to $\sim$ 2Gyr but based on this study, this appears to be

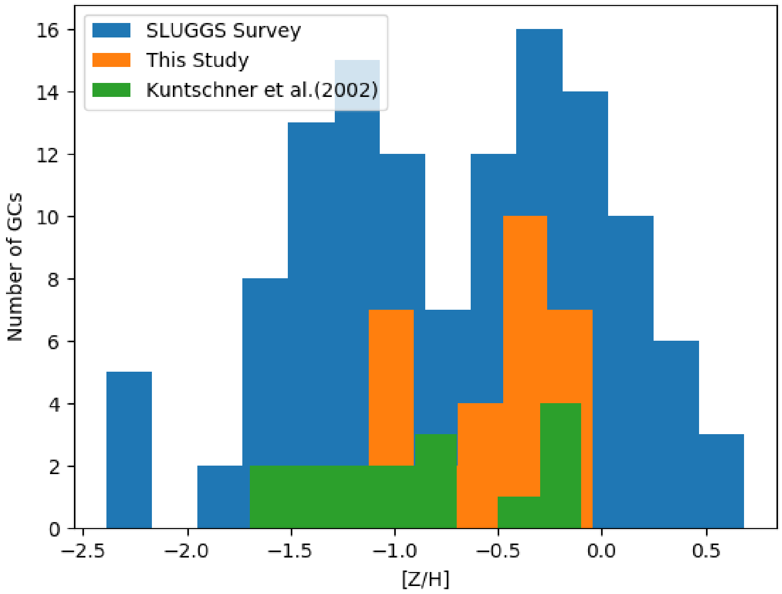

Figure 4.10: Histogram showing the metallicity distribution for this study along with that of Kuntschner et al. (2002) and Arnold et al. (2011). Both this study and the SLUGGS survey have the metal rich and metal poor peaks at a similar metallicity. Unfortunately the sample size of Kuntschner et al. (2002) is not large enough to draw any strong conclusions from the distribution.

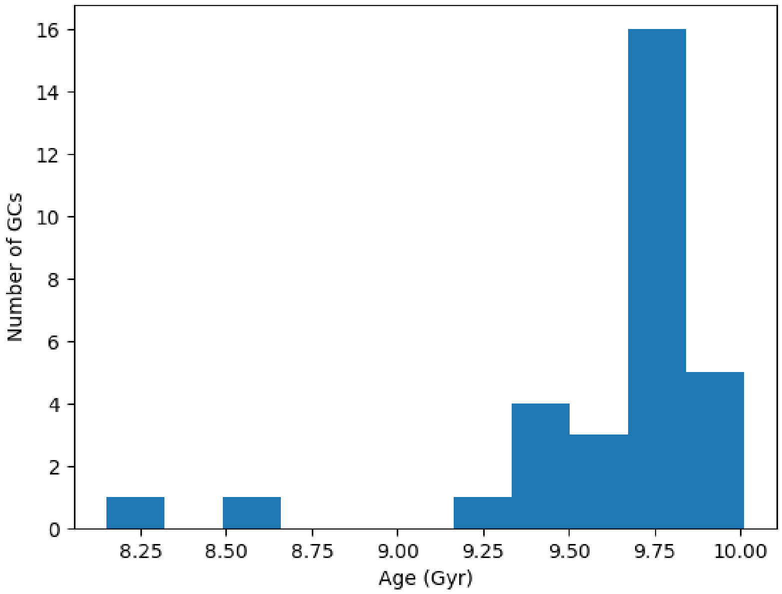

Figure 4.11: Histogram of the ages obtained from pPXF. The majority of GCs fall within 9.25-10 Gyr and there is no obvious bimodal age distribution as may be expected from multiple GC formation events. However the age estimates errors vary greatly and are up to ±1 Gyr.

closer to $\sim$ 1Gyr. This result is also mostly consistent with the ages found by Norris et al. (2006), as will be discussed in Chapter 5.

4.3 Combined datasets

The datasets of this study, Kuntschner et al. (2002) and Arnold et al. (2011) can be combined together in order to create an overview of the kinematics and metallicities of GCs in NGC 3115. Figure 4.13 shows the histograms of the combined data for these three studies, along with a best fit double GMM profile for the metallicities. It is clear from the data that there is a bimodal population of GCs, with the peak values at [Z/H]=-1.2 and -0.21. The combined kinematics are also consistent with the average mean velocity of the total dataset being 666 [±13] kms^{-1}. The combined velocity distribution (Figure 4.14) again shows the general downward trend of

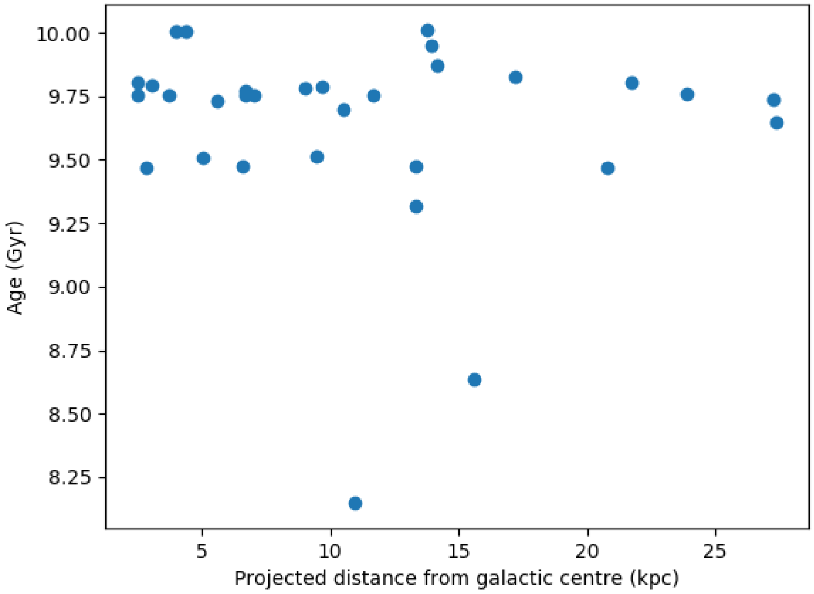

Figure 4.12: The plot shows pPXF obtained ages against their projected galacto-centric radii. From the plot it appears that for our GC targets, age remains relatively constant out to larger distances from the galactic centre.

velocities at greater galacto-centric distance, as seen by the best fit function. This shows the decreasing velocity dispersion of the GC system at larger galacto-centric radii, reflecting the dark matter halo in which NGC 3115 is embedded.

The metallicity gradient can also be constructed from the combined data of this survey and that from the SLUGGS survey. The top plot in Figure 4.15 shows metallicity against distance for all the GCs in both surveys. It appears that the general trend in both surveys agree, as metallicity decreases with projected galacto-centric radii. This has also been found to be the case in other galaxies apart from NGC 3115, as noted by in Zinn (1985) and Forbes et al. (2011). The bottom plot, shows the mean metallicity against binned distance for both the surveys, and is consistent with the relation of the previous plot.

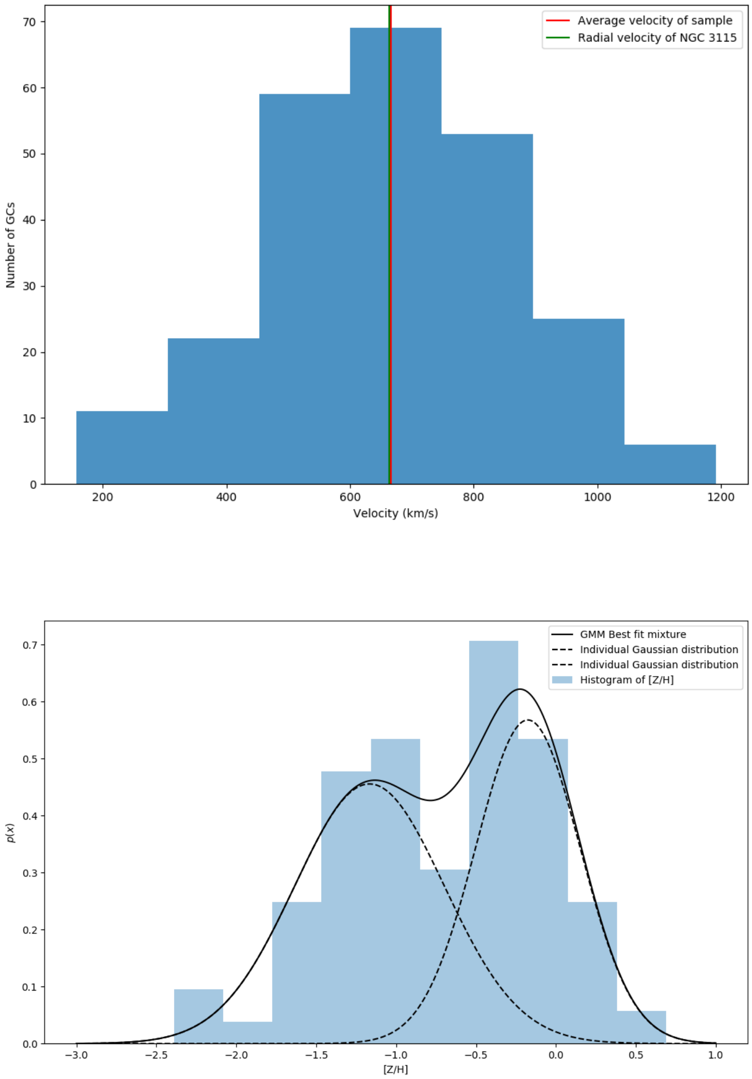

Figure 4.13: Histograms showing the kinematics and metallicity distributions for the combined dataset. The top graph shows the distribution of obtained velocities from Kuntschner et al. (2002), Arnold et al. (2011) and this study. The average velocity of all the GCs is 666 [±13] kms^{-1}. This is shown as the red line on the plot and the radial velocity of NGC 3115 is shown in green. The bottom plot is the metallicity distribution for the combined datasets of Kuntschner et al. (2002), Arnold et al. (2011) and this study, with a best fit line overplotted. The metallicities peak at [Z/H]=-1.2 and -0.21.

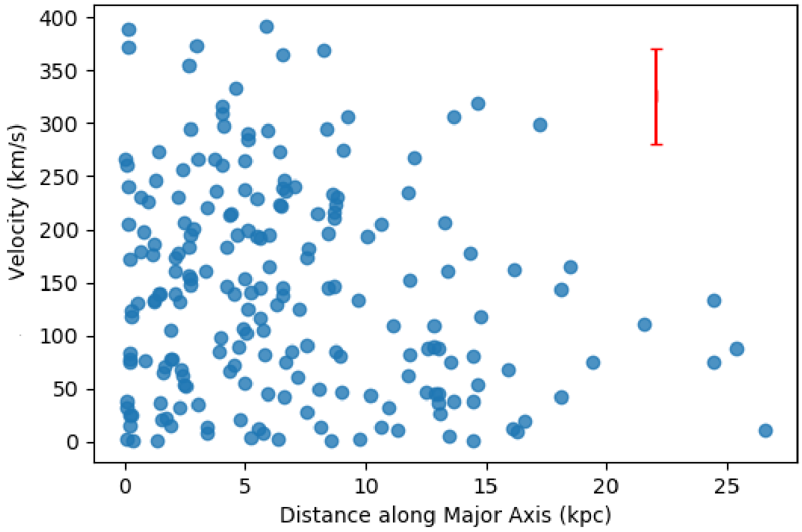

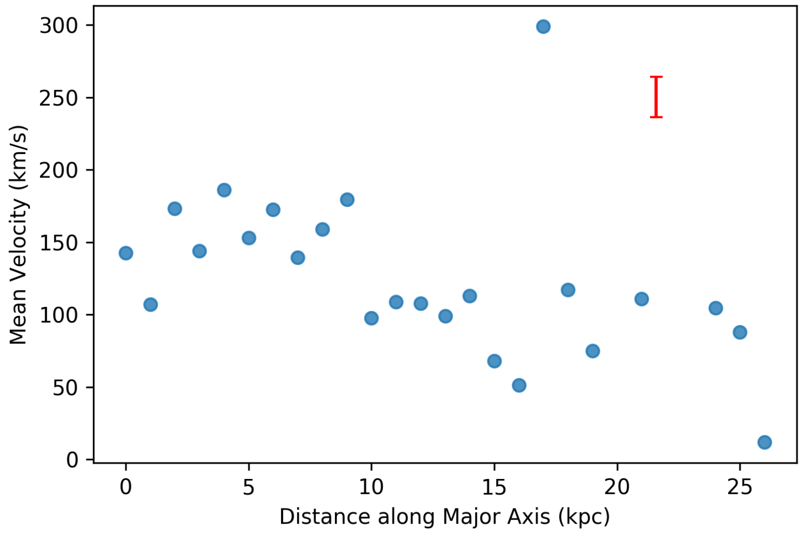

Figure 4.14: The top plot shows velocity residual (relative to the systemic velocity of NGC 3115) against distance along the major axis for the combined data of this study, Kuntschner et al. (2002) and Arnold et al. (2011). A maximum error for the velocities is shown in the top right corner of the plot. The bottom plot shows the mean velocity residual (in radial distance bins) against distance along the major axis for the data from this study, Kuntschner et al. (2002) and Arnold et al. (2011). Along with a representative error bar in the top right corner.

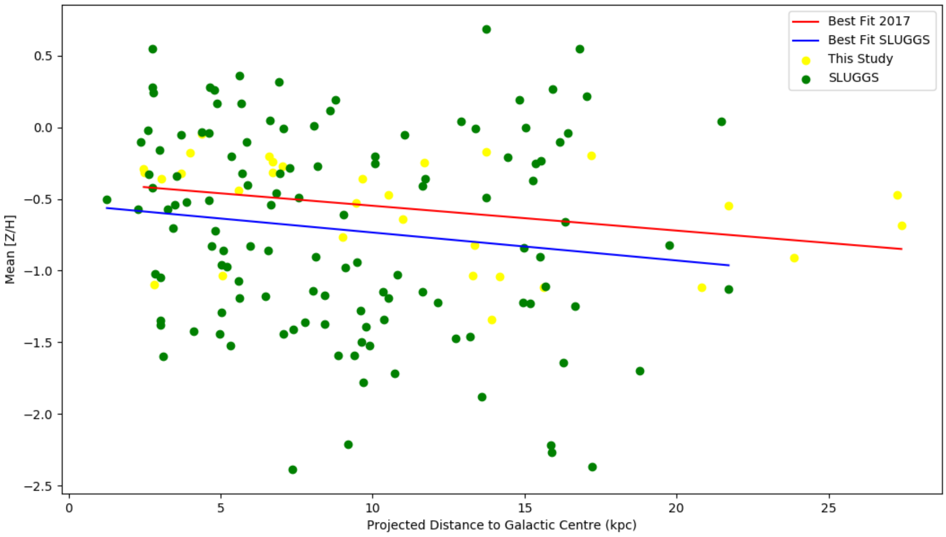

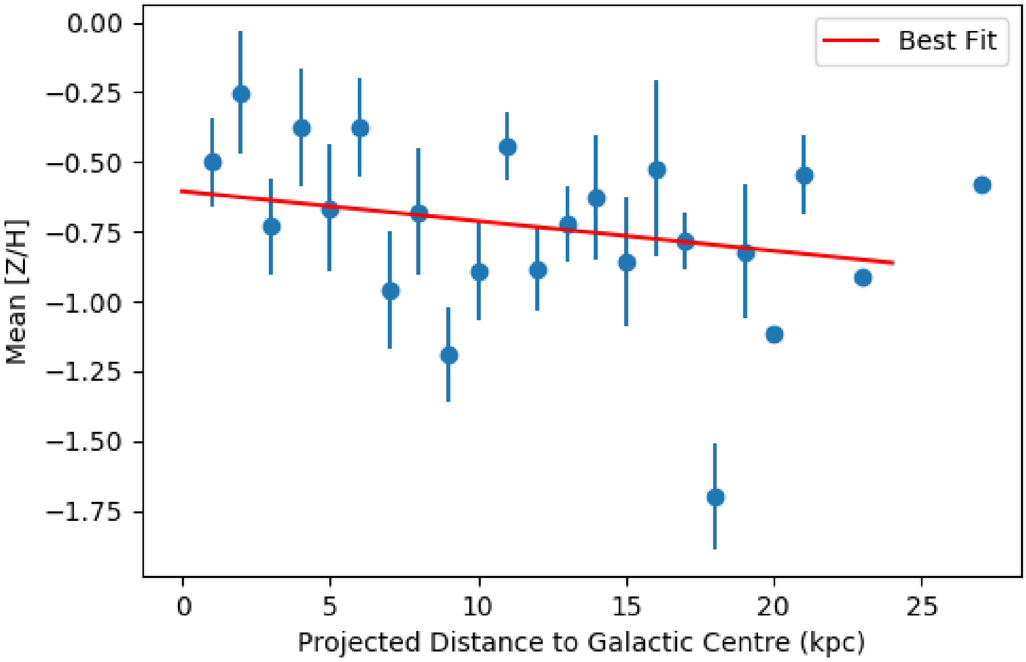

Figure 4.15: The top plot shows metallicity against projected galacto-centric distance for the GC targets of both Arnold et al. (2011) and this study, along with best fit lines for both datasets. The bottom plot is the mean [Z/H] against projected galacto-centric distance for the combined dataset, with a best fit line plotted over the data.

Chapter 5

Discussion and Conclusions

The aim of this project was to add to the expanding dataset of spectroscopy for GCs around the S0 galaxy NGC 3115. More specifically, GCs that are located at larger galacto-centric distances than had previously been attempted, in order to obtain velocities and metallicities, for GCs from varying components of the galaxy, thereby gaining a greater understanding of the distribution of the GC subpopulations within NGC 3115. Within this thesis the methods for reducing the data, along with obtaining meaningful results from them, has been presented. The analysis of these results has been presented within the context of previous studies. In this chapter, the implications of the results of this study, and the precursor studies, will be investigated to establish preliminary conclusions and areas that require further investigation.

5.1 Implications for the formation of NGC 3115 and its GCs

The velocity distributions presented in Chapter 4, show evidence that the GC system of NGC 3115 is rotating about the minor axis of the galaxy (Figure 4.5) and within the inner ∼5 kpc, the GCs have velocities consistent with that of the stellar bulge measured by Norris et al. (2006). The best fits of both binned and unbinned velocity residuals appear to be declining at larger radii (see Figure 4.14), which corroborates the findings of Arnold et al. (2011) shown in Figure 5.1. According to their analysis, this result is not consistent with a major merger event, as this would produce higher than observed rotation in the outer regions of the galaxy. Arnold et al. (2011) instead postulate that the detection of a declining rotation profile, suggests a two-phase assembly scenario, where the inner bulge forms at high redshift and the outer bulge and halo growth is created by minor-merger accretion events (Vitvitska et al. 2002; Abadi et al. 2006; Bournaud et al. 2007; Qu et al. 2010). The declining velocity gradient of the GC system shown in Figure 4.14, could therefore represent the transition between a component formed at high redshift and another which has been formed by accretion. A similar rolling fit method to that of Arnold et al. (2011) has been used on the data in this study, which can be seen in Figure 5.2. This, along with Figure 5.3, which shows the method applied to the combined dataset, is consistent with the plot from Arnold et al. (2011), finding a declining velocity gradient beyond 5 kpc. It should be noted however, that at the largest radii there are low numbers of clusters in the radial bins.

The metallicities obtained in this study, appear to confirm what has previously been found in other studies. NGC 3115 hosts a bimodal GC population in metallicity as well as having a bimodal colour distribution. This bimodality can be seen in both the sample from this study (Figure 4.7), and when combined with Kuntschner et al. (2002) and Usher et al. (2012) (Figure 4.13). The combined metallicity distribution

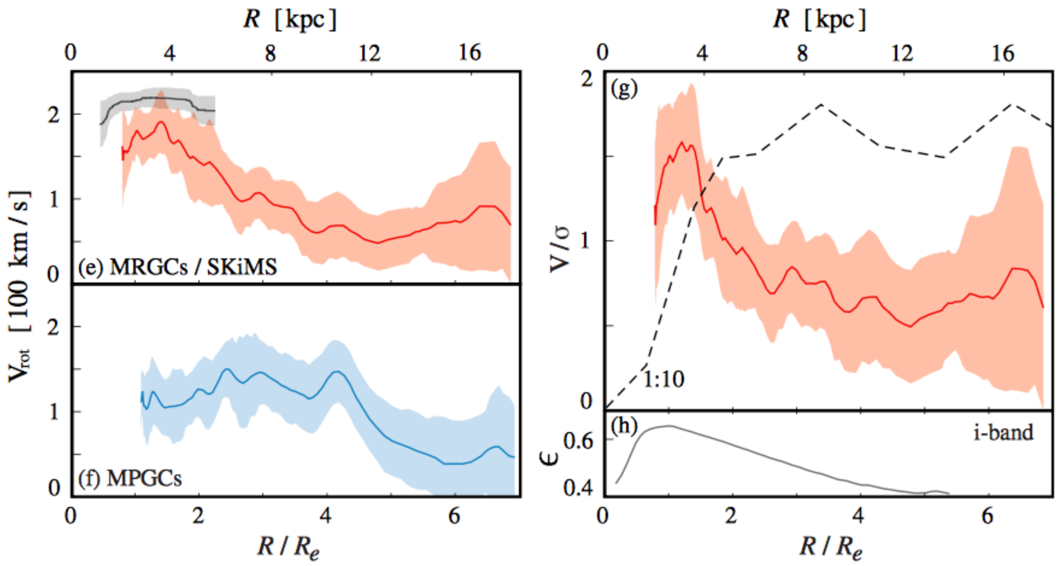

Figure 5.1: The left plot shows the smoothed rolling-fit rotational profile with uncertainty envelope for the metal-rich GCs (red curve) and metal-poor GCs (blue curve) along with the stellar light (black curve). The right plot shows the v/σ profile of the metal-rich GCs compared with a simulated merger remnant with a 1:10 mass-ratio (from Bournaud et al. (2005). Taken from Arnold et al. (2011).

is found to be bimodal using a Gaussian Mixture Method (GMM) test, as seen in Figure 4.13. These results suggest that the bimodal colour distribution of the GC population in NGC 3115, is consistent with being caused by a bimodal metallicity distribution. It is therefore unlikely that other effects, such as a difference in ages between the GC sub-populations, play a major role in creating the bimodality in colour. Both the sample from this study, and the combined data, imply a declining metallicity gradient. This is again consistent with the findings of Arnold et al. (2011) and would be expected in their hypothesis of a two-phase assembly scenario because the lower-mass accreted systems would be expected to be more metal-poor than NGC 3115 (Naab et al. 2009; Bezanson et al. 2009).

Kuntschner et al. (2002) found the GC sub-population ages in NGC 3115 to be coeval at 11-12[±2] Gyr, with an indication that the red clusters may be slightly younger by ~2 Gyr. The results of the study in this thesis find 29 of the 31 GCs to be between 9-10 Gyr, which is within 1σ of the mean age found by Kuntschner

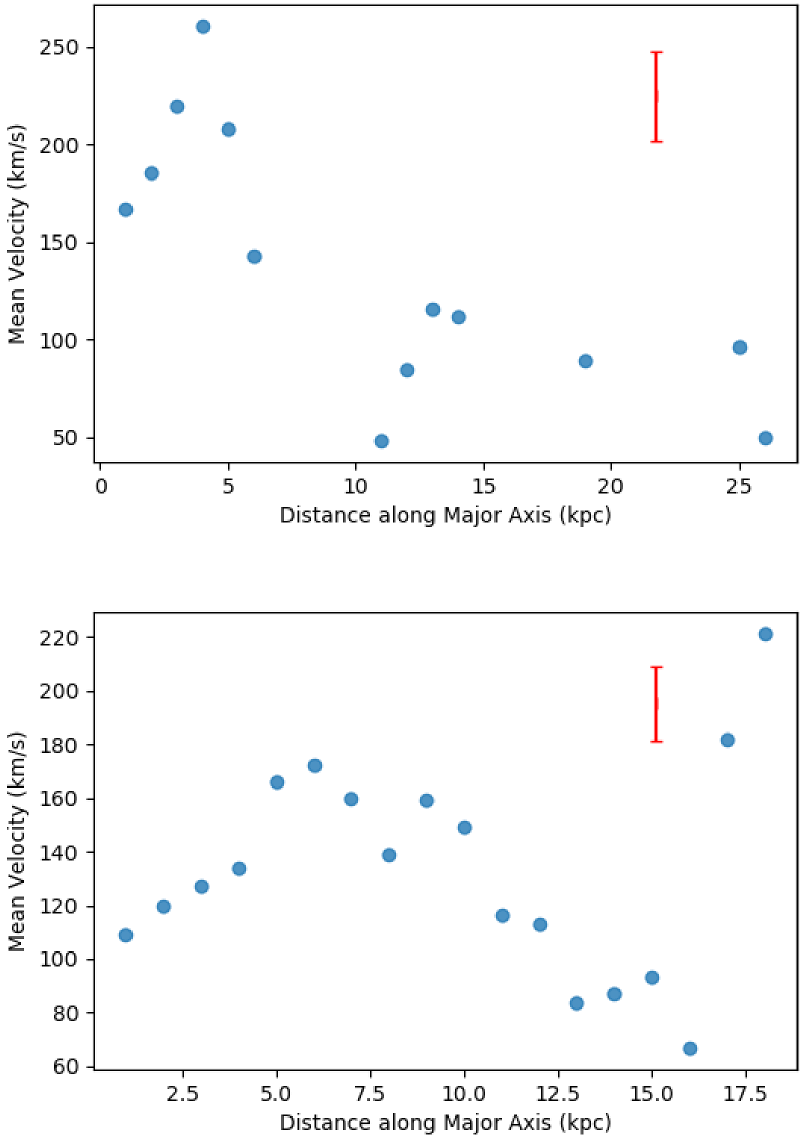

Figure 5.2: This figure shows the velocity plot using a rolling fit technique similar to that of Arnold et al. (2011). The data for both studies is binned in radial distances of 1 kpc. The top plot is only for data produced from the study in this thesis, whereas the bottom plot is for the data from Arnold et al. (2011). In our data we find a similar result with the velocity gradient decreasing at radii $\geq$ 5kpc.

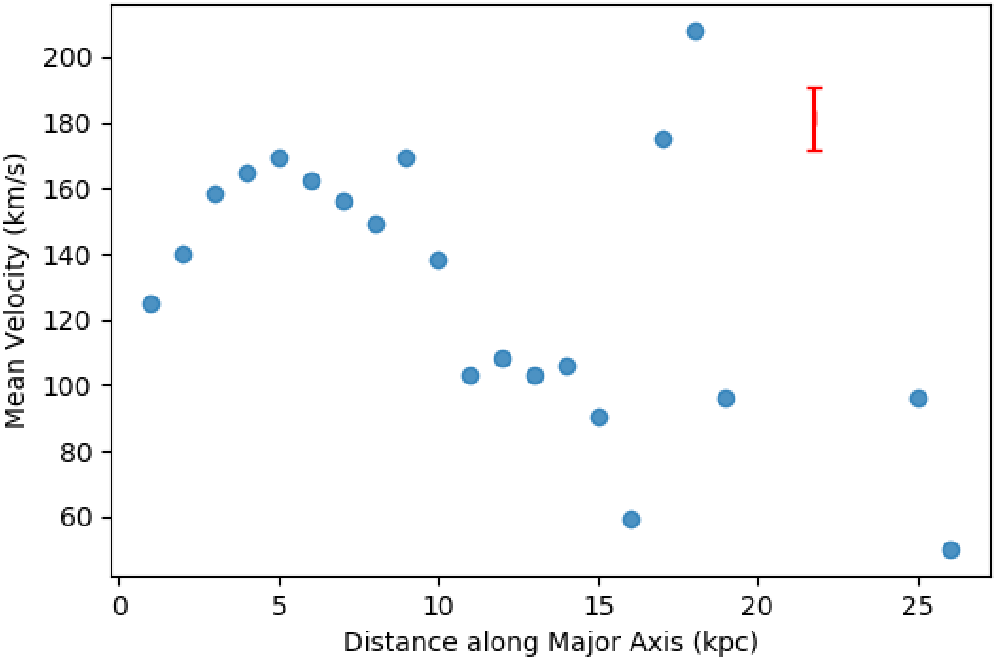

Figure 5.3: This is a rolling-fit velocity profile using the data from the study in this thesis and that of Arnold et al. (2011). The data is binned in radial distances of 1 kpc, with the bins within 15 kpc containing $\sim$ 15 GC velocities. However, those at the largest radii frequently only contain 1 GC.

et al. (2002). There is also no sign of a large age difference between the two subpopulations of GCs, with both metal-poor and metal-rich clusters having similar mean ages. These results may be compared with the findings of Norris et al. (2006), who looked at longslit spectra of the minor axis of NGC 3115 (which should trace the spheroidal component of the galaxy) and found it to have similar properties to the red GCs at large radii, and estimate that the spheroid has a mean age of ∼10-12 Gyr. In the sample in this thesis, there is also potential evidence of a small younger population of GCs, with ages ∼8 Gyr, although only two such objects were found in this study. Norris et al. (2006) suggest that there may be a young (5-8Gyr), chemically enriched stellar disc component in their major axis disc spectra, therefore if these ages are correct, these younger GCs may have formed along with the disc in NGC 3115.

If GCs only form during major periods of star formation, then the results of this study suggest that NGC 3115 has not undergone such an event in the last ∼8 Gyr. This is similar to the conclusions of Puzia et al. (2002), who claim that NGC 3115 has a similar GC population to the Milky Way, with two sub-systems differing mainly in metallicity, with a small age difference between them. It is still possible that multiple GC formations have occurred in NGC 3115, however, this study finds that these events would have to have occured within a period of ∼1 Gyr for the ages obtained to be consistent with this hypothesis. It is possible that other subpopulations of GCs exist in NGC 3115, with ages different from those detected in this study, however there is no significant evidence for it from our sample of GCs.

5.2 Suggestions for further investigation

In order to better understand the GC population of NGC 3115, higher SNR observations of the GCs discovered in this study are ideally required. The initial dataset covered a large range of galacto-centric radii, which has not been previously or subsequently observed, that could allow for GC subpopulations to be associated with different components of NGC 3115. In this study there were initially many more GC candidate targets than the final number of useful spectra used in the data analysis, so obtaining observations with a higher SNR should be a priority. This will allow a larger number of GCs to have their ages and metallicities extracted and investigate whether the sub-populations, of blue and red clusters, are separated by small age differences as well as metallicity. Abundance ratios for more clusters would also enable further investigation of the trends of α/Fe, found in the stellar populations by Norris et al. (2006), applies to the GCs as well. Finally, the aim of these studies is not simply to discover more about the GC population of NGC 3115, but also to attempt to find a way of using GCs to understand galaxy evolution in all galaxy types. Therefore, expanding the analysis to other galaxies, and more specifically other galaxy morphologies, will help establish the extent to which GCs are a viable tracer of galaxy evolution.

5.3 Summary and Conclusions

This thesis has explored the importance of GCs in the context of galaxy evolution, and how they can be used to track star formation events over time. Previous studies of extragalactic GCs, with particular reference to studies that examined NGC 3115, were discussed and their conclusions presented. The GC sample of this thesis was then introduced, along with an explanation of how the data reduction was performed. The use of the full spectrum fitting method pPXF and how it was implemented with this sample was explored, and details of how kinematics and metallicities were extracted from the spectra were presented. The reliability of the results were examined, to ensure that the data analysis had produced realistic results. The velocity and metallicity distributions for NGC 3115 were then compared to previous studies. Finally, the sample of this study was combined with that of

Kuntschner et al. (2002) and Usher et al. (2012) to enable more robust conclusions to be derived from the augmented dataset.

This study was a success in so far as it has added more kinematic, metallicity and age results to the previous studies of GCs in NGC 3115. However, the numbers of useful spectra expected from the initial research proposal were significantly higher than the final sample size. This was primarily due to the lower than expected SNR in many of the GC spectra. Even with this reduced sample size, it has however been possible to obtain meaningful results from the data and strengthen findings of previous studies of NGC 3115.

We find a bimodal metallicity distribution which is consistent with that of Brodie et al. (2012), based on their CaT index results. This does not support the suggestion of Yoon et al. (2006) that the metallicity distributions are uni-modal and the observed colour bimodality is caused by an artefact of strongly non-linear colour-metallicity transformations. We also find declining metallicity and velocity gradients, which give support to the suggestion of Arnold et al. (2011), that NGC 3115 was formed in a two-phase assembly process. While the ages obtained have significant uncertainty, due to the SNR of the spectra, they do appear to be consistent with previous studies to within errors. The results demonstrate that the two sub-populations of GCs are coeval, which supports previous work by Kuntschner et al. (2002) and Arnold et al. (2011). As no GCs have been detected with ages less than 8 Gyr, it suggests that there has been no major star-formation events in NGC 3115 since that time.

With a combined sample of $\sim$230 GC velocities and $\sim$180 metallicities, there is now a significant population of GCs in NGC 3115 from which to draw conclusions. This enables more confidence in the results, as the sample is more likely to be representative of the entire GC population of NGC 3115. Also, with GCs coming from a wider range of galacto-centric radii, possible links between GC properties and different components of NGC 3115 are becoming better established, with the potential of finding common origins for these components. This will allow for refined tests of galaxy formation and evolution theories and determine whether GCs can be used successfully as tracers of their host galaxy stellar population in a wide range of galaxy types.

Appendix A

Table 1: Table of target objects with their: Field, Slit ID, Object ID, Right Ascension, Declination, VRI magnitude and associated error obtained from the pre-imaging.

Field	Slit ID	Object ID	RA	Dec	V	V error	R	R error	I	I error
1	2	1_2	151.3568	-7.6754	22.4893	0.1349	21.3288	0.0683	20.1392	2.3501
1	3	1_3	151.3436	-7.6886	21.4501	0.0767	20.8305	0.0508	20.2397	1.2104
1	4	1_4	151.3303	-7.7017	22.8284	0.1586	22.2282	0.1079	21.4675	1.3609
1	5	1_5	151.317	-7.7149	18.3627	0.0179	17.6577	0.0114	17.1361	1.2266
1	6	1_6	151.3038	-7.7280	21.265	0.0716	20.8016	0.0495	20.2009	1.0641
1	7	1_7	151.3598	-7.7316	21.0537	0.0648	20.582	0.0452	20.1106	0.9431
1	8	1_8	151.3535	-7.7347	22.2826	0.1233	21.666	0.0785	21.0167	1.2659
1	9	1_9	151.3732	-7.7118	22.5152	0.1367	21.9251	0.09	21.1605	1.3547
1	10	1_10	151.3908	-7.7039	21.853	0.0958	21.107	0.0585	20.4672	1.3858
1	11	1_11	151.3486	-7.7489	21.7059	0.0902	20.4353	0.042	18.5298	3.1761
1	12	1_12	151.3549	-7.7496	19.1626	0.026	18.7138	0.0186	18.3459	0.8167
1	14	1_14	151.3547	-7.7157	21.6676	0.0885	21.0918	0.0588	20.6838	0.9838
1	15	1_15	151.3536	-7.7207	21.678	0.0886	21.0776	0.0585	20.51	1.168
1	16	1_16	151.345	-7.7345	22.7455	0.1522	22.0206	0.094	21.5896	1.1559

Field	Slit ID	Object ID	RA	Dec	V	V error	R	R error	I	I error
1	17	1_17	151.3371	-7.7230	22.6441	0.1453	22.0455	0.0972	21.2812	1.3629
1	18	1_18	151.3271	-7.7367	21.4195	0.0786	21.057	0.0573	20.581	0.8385
1	19	1_19	151.3256	-7.7350	19.682	0.0332	19.0906	0.0223	18.505	1.177
1	20	1_20	151.3479	-7.7089	22.7593	0.1529	22.1831	0.1022	21.8391	0.9202
1	21	1_21	151.3383	-7.7147	21.3679	0.0756	20.848	0.052	20.3741	0.9938
1	22	1_22	151.3263	-7.7161	21.8502	0.0921	21.1244	0.058	20.6333	1.2169
1	23	1_23	151.3163	-7.7331	22.486	0.1328	21.9236	0.0892	21.2686	1.2174
1	24	1_24	151.3471	-7.6990	21.0486	0.0631	20.5651	0.0445	20.2138	0.8348
1	25	1_25	151.3197	-7.7185	20.9298	0.0598	20.3087	0.0395	19.7518	1.178
1	26	1_26	151.3178	-7.7129	21.8397	0.0918	20.9207	0.0527	20.2478	1.5919
1	27	1_27	151.3362	-7.6919	21.9049	0.0962	21.2622	0.0624	20.7533	1.1516
1	28	1_28	151.3037	-7.7128	21.2223	0.0686	20.4938	0.0431	19.9314	1.2909
1	29	1_29	151.3161	-7.7039	21.349	0.073	20.5426	0.0442	19.9066	1.4424
1	30	1_30	151.3222	-7.7018	22.131	0.1087	21.5046	0.0697	20.7283	1.4027
1	31	1_31	151.335	-7.6784	22.2501	0.1168	21.6859	0.078	21.301	0.9491
1	32	1_32	151.3511	-7.6524	20.9152	0.0602	20.4558	0.0427	20.0462	0.869
1	33	1_33	151.3121	-7.6950	21.7918	0.0901	21.1842	0.0602	20.7872	1.0046

Field	Slit ID	Object ID	RA	Dec	V	V error	R	R error	I	I error
1	34	1_34	151.321	-7.6894	22.9849	0.1697	22.2699	0.1012	21.8254	1.1595
1	35	1_35	151.2801	-7.6688	20.385	0.0463	19.8846	0.0323	19.4429	0.9421
1	36	1_36	151.2894	-7.6636	22.1656	0.1149	21.703	0.0793	21.1723	0.9933
1	37	1_37	151.3118	-7.6496	20.4987	0.049	19.9074	0.0327	19.2696	1.2291
1	38	1_38	151.3291	-7.6405	21.2131	0.0693	20.6802	0.0472	20.203	1.0101
1	39	1_39	151.3111	-7.6543	23.0507	0.1756	22.34	0.1133	21.9788	1.0719
1	40	1_40	151.2605	-7.6804	21.1418	0.0697	20.7866	0.0507	19.7395	1.4023
1	41	1_41	151.3034	-7.6747	21.8605	0.0965	21.2663	0.0634	20.7849	1.0756
1	42	1_42	151.3418	-7.6414	22.226	0.118	21.4649	0.07	20.942	1.284
1	43	1_43	151.3253	-7.6667	21.8437	0.0964	21.4393	0.0687	21.0279	0.8158
1	44	1_44	151.3285	-7.6669	20.2944	0.0443	19.5882	0.0281	18.9837	1.3107
1	45	1_45	151.3088	-7.6903	22.3354	0.1247	21.6137	0.0774	21.143	1.1924
2	1	2_1	151.3188	-7.7143	21.858	0.0888	20.8644	0.0498	20.1563	1.7017
2	2	2_2	151.3055	-7.7275	22.2175	0.1053	21.4166	0.0641	20.61	1.6075
2	3	2_3	151.2923	-7.7406	20.8649	0.0575	20.242	0.0379	19.5182	1.3467
2	4	2_4	151.279	-7.7538	22.1888	0.1056	21.6061	0.0722	20.8924	1.2964
2	6	2_6	151.2525	-7.7801	21.6571	0.0818	21.1823	0.0582	20.7093	0.9478

Field	Slit ID	Object ID	RA	Dec	V	V error	R	R error	I	I error
2	7	2_7	151.3488	-7.7569	23.197	0.1748	21.7502	0.079	20.6753	2.5217
2	8	2_8	151.3452	-7.7577	21.0729	0.0609	20.619	0.0444	20.2252	0.8477
2	9	2_9	151.3167	-7.7832	19.1421	0.0249	18.7804	0.0188	18.4096	0.7325
2	10	2_10	151.3044	-7.7932	22.094	0.1017	21.4727	0.0679	20.9783	1.1157
2	11	2_11	151.2933	-7.7986	22.4107	0.123	21.7213	0.0782	21.1754	1.2353
2	12	2_12	151.3044	-7.7846	22.9924	0.1614	21.8379	0.0798	20.0503	2.9421
2	13	2_13	151.3381	-7.7483	21.6203	0.0819	20.7796	0.0484	19.601	2.0193
2	14	2_14	151.2826	-7.8002	21.8632	0.0908	21.2424	0.0601	20.5425	1.3207
2	15	2_15	151.2998	-7.7804	21.0489	0.061	20.5333	0.0429	20.0059	1.043
2	16	2_16	151.2813	-7.7965	23.2	0.1798	21.8402	0.0818	20.1607	3.0393
2	17	2_17	151.2865	-7.7894	22.6305	0.1329	21.9173	0.0831	21.3256	1.3049
2	18	2_18	151.3309	-7.7391	20.9032	0.0572	20.4309	0.0408	19.8833	1.0199
2	19	2_19	151.3133	-7.7598	22.3473	0.116	21.7208	0.0772	21.0975	1.2498
2	20	2_20	151.2833	-7.7827	21.5143	0.0767	20.9329	0.0519	20.2694	1.2449
2	21	2_21	151.2898	-7.7727	21.1914	0.0656	20.6832	0.0459	20.1064	1.085
2	22	2_22	151.3004	-7.7590	22.7288	0.1367	22.1095	0.0907	21.3472	1.3816
2	23	2_23	151.3225	-7.7338	21.2816	0.0686	20.8226	0.0491	20.2298	1.0518

Field	Slit ID	Object ID	RA	Dec	V	V error	R	R error	I	I error
2	24	2_24	151.2929	-7.7573	21.3955	0.0728	20.929	0.0517	20.36	1.0355
2	25	2_25	151.298	-7.7450	20.1883	0.0406	19.6386	0.028	19.0985	1.0898
2	26	2_26	151.3092	-7.7368	19.9097	0.0356	19.0943	0.0217	18.4077	1.502
2	27	2_27	151.3068	-7.7365	21.8551	0.089	21.258	0.0602	20.7348	1.1203
2	28	2_28	151.3049	-7.7328	19.7678	0.0333	19.1414	0.0222	18.5572	1.2106
2	29	2_29	151.3056	-7.7347	21.375	0.071	20.7374	0.0471	20.0843	1.2907
2	30	2_30	151.3174	-7.7356	20.6028	0.0493	20.1085	0.035	19.6546	0.9482
2	31	2_31	151.334	-7.7615	22.6471	0.1343	21.5627	0.0702	20.087	2.5601
2	32	2_32	151.3041	-7.7276	21.46	0.0739	20.8325	0.0487	20.2728	1.1872
2	34	2_34	151.2776	-7.7500	21.5579	0.078	20.889	0.0508	20.2057	1.3522
2	37	2_37	151.2949	-7.7262	22.4688	0.122	21.9172	0.0828	21.1053	1.3635
2	39	2_39	151.3061	-7.7076	21.8272	0.088	21.2211	0.0594	20.6065	1.2207
2	40	2_40	151.3059	-7.7050	21.0325	0.059	20.2926	0.0376	19.6633	1.3692
2	41	2_41	151.2998	-7.7083	21.9116	0.0941	21.2284	0.0604	20.5619	1.3497
2	42	2_42	151.2753	-7.7409	20.4246	0.0455	19.832	0.0307	19.1541	1.2705
2	43	2_43	151.3004	-7.7041	21.0777	0.0617	20.4468	0.041	19.7898	1.2879
2	44	2_44	151.288	-7.7090	22.5144	0.1243	21.9394	0.0846	21.3979	1.1165

Field	Slit ID	Object ID	RA	Dec	V	V error	R	R error	I	I error
2	45	2_45	151.2624	-7.7318	22.6215	0.1321	22.0369	0.0897	21.5699	1.0516
2	46	2_46	151.2419	-7.7498	21.6067	0.0803	21.1939	0.0588	20.8069	0.7998
2	47	2_47	151.2901	-7.7000	19.9748	0.0368	19.3738	0.0248	18.7466	1.2282
2	48	2_48	151.2836	-7.7043	21.7371	0.0857	21.1969	0.059	20.4626	1.2745
2	49	2_49	151.2838	-7.7014	22.9555	0.1563	22.2092	0.0973	21.5093	1.4462
2	50	2_50	151.2679	-7.7146	21.9907	0.1002	20.9437	0.053	20.0348	1.9559
2	51	2_51	151.279	-7.7008	22.5702	0.1343	22.0723	0.0941	21.4106	1.1596
2	52	2_52	151.2739	-7.6948	20.9863	0.0593	20.406	0.0402	19.7525	1.2338
2	53	2_53	151.2522	-7.7133	20.5191	0.0475	20.0309	0.0337	19.4914	1.0277
2	54	2_54	151.2392	-7.7233	21.9892	0.0969	21.471	0.0674	20.9638	1.0254
2	55	2_55	151.2806	-7.6792	22.1474	0.1068	21.5833	0.0712	21.0116	1.1358
2	56	2_56	151.271	-7.6859	22.1327	0.1047	21.5505	0.0708	21.013	1.1197
2	57	2_57	151.273	-7.6811	22.1651	0.1061	21.4984	0.0685	20.8811	1.284
2	58	2_58	151.2778	-7.6727	22.2152	0.1098	21.5844	0.0711	21.195	1.0202
2	59	2_59	151.245	-7.7014	22.4897	0.1281	21.6839	0.0749	20.8835	1.6062
2	60	2_60	151.2529	-7.6882	20.1275	0.0398	19.6708	0.0284	19.2264	0.9011
3	7	3_7	151.4397	-7.6664	23.1483	0.1623	22.474	0.1082	21.7857	1.3626

Field	Slit ID	Object ID	RA	Dec	V	V error	R	R error	I	I error
3	8	3_8	151.4046	-7.6985	22.9566	0.1432	22.5266	0.1106	22.2126	0.744
3	9	3_9	151.4175	-7.6837	22.685	0.129	22.0099	0.0871	21.381	1.304
3	10	3_10	151.4435	-7.6557	20.712	0.0496	20.2096	0.0357	19.7227	0.9893
3	11	3_11	151.4245	-7.6717	21.377	0.0678	20.8733	0.0489	20.2962	1.0808
3	12	3_12	151.4	-7.6921	22.9348	0.1489	21.6819	0.0752	20.5532	2.3816
3	13	3_13	151.4482	-7.6409	21.7726	0.083	21.3788	0.0619	20.8466	0.926
3	14	3_14	151.4396	-7.6465	22.9985	0.1486	21.7577	0.0753	20.1054	2.8931
3	15	3_15	151.4007	-7.6816	22.5478	0.1209	22.1109	0.0908	21.6167	0.9311
3	16	3_16	151.4237	-7.6540	22.5042	0.1163	21.9748	0.0839	21.6087	0.8955
3	17	3_17	151.4267	-7.6533	23.6413	0.2031	22.4396	0.1074	21.1445	2.4968
3	18	3_18	151.4005	-7.6742	20.874	0.0537	20.1734	0.0354	19.427	1.447
3	19	3_19	151.4066	-7.6652	22.0212	0.092	21.4421	0.0645	20.9121	1.1091
3	20	3_20	151.425	-7.6438	21.2456	0.0637	20.5076	0.0411	19.8666	1.379
3	21	3_21	151.384	-7.6807	23.1221	0.1674	21.6928	0.0758	20.5468	2.5753
3	22	3_22	151.4339	-7.6272	22.9691	0.148	22.3367	0.0996	21.7078	1.2613
3	23	3_23	151.3825	-7.6753	22.3616	0.11	21.6108	0.0723	20.6961	1.6655
3	24	3_24	151.4331	-7.6223	21.3282	0.0678	20.9672	0.0526	20.4308	0.8974

Field	Slit ID	Object ID	RA	Dec	V	V error	R	R error	I	I error
3	25	3_25	151.3892	-7.6626	21.906	0.088	21.1943	0.0574	20.5159	1.3901
3	26	3_26	151.4318	-7.6171	22.1351	0.0972	21.6307	0.0701	21.1349	1.0002
3	27	3_27	151.3835	-7.6621	21.8485	0.0848	20.7364	0.0459	19.3037	2.5448
3	28	3_28	151.4192	-7.6242	22.1989	0.1012	21.5329	0.0688	21.062	1.1369
3	29	3_29	151.4177	-7.6231	22.0798	0.0951	21.5028	0.0661	20.7368	1.343
3	30	3_30	151.3655	-7.6724	23.7221	0.2178	23.106	0.1519	22.1516	1.5705
3	31	3_31	151.4244	-7.6060	20.3641	0.0422	19.84	0.0301	19.4861	0.878
3	33	3_33	151.3798	-7.6465	20.193	0.0389	19.7747	0.0291	19.4012	0.7918
3	34	3_34	151.3733	-7.6504	21.9622	0.0877	21.4561	0.0646	20.8789	1.0833
3	35	3_35	151.4206	-7.6011	21.2557	0.0643	20.8323	0.0482	20.4309	0.8248
3	36	3_36	151.3943	-7.6244	22.0695	0.0945	20.9074	0.0496	19.3618	2.7077
3	37	3_37	151.4097	-7.6060	22.8352	0.1373	21.8529	0.0793	20.9553	1.8799
3	38	3_38	151.3636	-7.6480	21.7765	0.0817	21.0852	0.0539	20.493	1.2835
3	39	3_39	151.3755	-7.6332	21.7259	0.0801	20.8024	0.0476	20.0541	1.6718
3	40	3_40	151.3713	-7.6350	22.7933	0.1368	22.0269	0.0889	21.6132	1.1801
3	41	3_41	151.3539	-7.6498	19.684	0.0308	19.2951	0.0233	18.9123	0.7717
3	42	3_42	151.3725	-7.6289	21.2194	0.063	20.3942	0.039	19.6834	1.536

Field	Slit ID	Object ID	RA	Dec	V	V error	R	R error	I	I error
3	43	3_43	151.383	-7.6158	23.5063	0.189	22.1329	0.0897	20.2198	3.2865
3	44	3_44	151.3925	-7.5979	21.4687	0.0707	20.7672	0.0465	20.4854	0.9833
3	45	3_45	151.3833	-7.6039	21.1045	0.0596	20.2441	0.0363	19.4853	1.6192
3	46	3_46	151.3421	-7.6420	22.3729	0.1077	21.8781	0.0801	21.3552	1.0177
3	47	3_47	151.4011	-7.5811	22.5236	0.1165	21.2666	0.0599	19.3912	3.1324
3	48	3_48	151.3442	-7.6350	22.6371	0.1246	21.591	0.0696	20.1533	2.4838
3	49	3_49	151.3843	-7.5928	20.8148	0.052	19.7287	0.0285	18.449	2.3658
3	50	3_50	151.359	-7.6152	24.1811	0.269	22.6554	0.1181	21.1563	3.0248
3	51	3_51	151.33	-7.6415	21.2569	0.0641	20.7302	0.0457	20.2027	1.0542
3	52	3_52	151.3437	-7.6222	22.8779	0.143	21.9602	0.0857	21.1446	1.7333
3	53	3_53	151.3363	-7.6243	22.097	0.0963	21.4932	0.067	20.9695	1.1275
3	55	3_55	151.361	-7.5968	23.0989	0.1557	22.0393	0.0857	20.4039	2.695
3	56	3_56	151.3299	-7.6255	23.2992	0.1751	22.9165	0.1329	22.3834	0.9158
3	57	3_57	151.3311	-7.6185	22.6331	0.1253	21.5599	0.0702	21.02	1.6131
3	58	3_58	151.3456	-7.6014	20.5958	0.047	20.0573	0.0333	19.5276	1.0682
3	59	3_59	151.3664	-7.5782	22.5144	0.116	21.2526	0.0586	19.506	3.0084
3	60	3_60	151.3755	-7.5667	22.028	0.0936	21.7484	0.0749	20.7967	1.2313

Field	Slit ID	Object ID	RA	Dec	V	V error	R	R error	I	I error
4	1	4_1	151.2617	-7.7711	22.623	0.1255	22.4138	0.1032	21.9266	0.6964
4	4	4_4	151.2219	-7.8106	23.7522	0.2199	23.1856	0.1516	22.9129	0.8393
4	7	4_7	151.2511	-7.8541	23.232	0.1665	22.6519	0.1166	22.4356	0.7964
4	8	4_8	151.2429	-7.8596	21.7073	0.0796	21.4769	0.0653	20.8299	0.8774
4	9	4_9	151.2849	-7.8153	22.1827	0.101	21.5769	0.0689	20.9948	1.1879
4	10	4_10	151.2601	-7.8376	19.1596	0.0241	18.717	0.0178	18.2581	0.9015
4	12	4_12	151.2629	-7.8297	21.2176	0.0629	20.7081	0.0452	20.3218	0.8958
4	13	4_13	151.2301	-7.8532	21.3319	0.0666	20.728	0.0455	20.0058	1.3261
4	14	4_14	151.2854	-7.8016	22.5361	0.1205	21.6375	0.0701	20.7104	1.8257
4	16	4_16	151.2828	-7.7984	21.0414	0.058	20.5076	0.0411	19.89	1.1514
4	17	4_17	151.2815	-7.7969	22.7706	0.1362	22.1165	0.0908	20.1786	2.592
4	18	4_18	151.2287	-7.8457	22.8012	0.1405	22.3293	0.1045	21.5967	1.2045
4	19	4_19	151.2651	-7.8056	22.3928	0.1119	21.8247	0.077	21.2893	1.1035
4	20	4_20	151.2717	-7.7959	23.7022	0.2163	22.9969	0.1435	22.6349	1.0673
4	21	4_21	151.2551	-7.8098	21.3337	0.0671	20.8343	0.0484	20.2885	1.0452
4	22	4_22	151.2463	-7.8157	22.4918	0.118	21.8959	0.0818	21.2336	1.2582
4	23	4_23	151.2304	-7.8285	23.2335	0.1707	22.6691	0.1217	22.1569	1.0766

Field	Slit ID	Object ID	RA	Dec	V	V error	R	R error	I	I error
4	24	4_24	151.2703	-7.7863	22.6885	0.1272	21.636	0.0704	19.9071	2.7814
4	25	4_25	151.2546	-7.7993	23.0816	0.1554	21.917	0.0806	20.3867	2.6949
4	26	4_26	151.2481	-7.8033	23.7792	0.2177	22.83	0.1327	21.62	2.1592
4	27	4_27	151.227	-7.8217	21.4484	0.0703	20.8023	0.0471	20.2371	1.2113
4	28	4_28	151.2333	-7.8128	23.4285	0.1869	22.2885	0.0981	20.4631	2.9654
4	29	4_29	151.2618	-7.7817	22.1939	0.1008	21.6701	0.0714	21.0802	1.1137
4	30	4_30	151.2647	-7.7759	21.7005	0.0792	21.1472	0.0556	20.2919	1.4086
4	31	4_31	151.2462	-7.7916	20.7606	0.0508	20.1382	0.0345	19.5157	1.2449
4	32	4_32	151.2522	-7.7790	21.735	0.0802	21.1863	0.0564	20.7064	1.0286
4	33	4_33	151.2168	-7.8115	21.8859	0.0875	21.2758	0.0589	20.3482	1.5377
4	34	4_34	151.2138	-7.8115	22.0881	0.0956	20.9878	0.0513	19.5677	2.5204
4	35	4_35	151.2029	-7.8194	21.5226	0.0727	21.1166	0.0546	20.7156	0.807
4	36	4_36	151.1968	-7.8230	23.3925	0.1828	22.4619	0.1107	21.7284	1.6641
4	37	4_37	151.2478	-7.7698	20.9368	0.0552	20.4215	0.0395	19.8635	1.0733
4	38	4_38	151.1983	-7.8119	19.0127	0.0225	18.4363	0.0156	17.9072	1.1055
4	39	4_39	151.228	-7.7861	22.6665	0.1263	21.7168	0.0731	20.9409	1.7256
4	40	4_40	151.1839	-7.8235	22.906	0.1422	22.4338	0.1044	21.9163	0.9897

Field	Slit ID	Object ID	RA	Dec	V	V error	R	R error	I	I error
4	41	4_41	151.1971	-7.8084	21.7051	0.0799	21.3008	0.0598	20.785	0.9201
4	42	4_42	151.2396	-7.7640	21.4762	0.071	20.3444	0.038	18.8273	2.6489
4	43	4_43	151.2321	-7.7642	21.652	0.0779	21.0935	0.0543	20.4962	1.1558
4	44	4_44	151.2251	-7.7686	22.3758	0.1104	21.135	0.0551	19.2103	3.1655
4	45	4_45	151.2155	-7.7756	22.7521	0.1349	21.5916	0.0693	20.666	2.0861
4	46	4_46	151.1931	-7.7946	20.5351	0.0457	19.8244	0.0297	19.1572	1.3779
4	47	4_47	151.1966	-7.7880	21.9634	0.092	21.1853	0.0577	20.4527	1.5107
4	48	4_48	151.1835	-7.7982	21.1068	0.0598	20.7258	0.0454	20.419	0.6878
4	49	4_49	151.2308	-7.7487	20.7004	0.0496	19.7699	0.0291	18.7624	1.938
4	50	4_50	151.1712	-7.8048	21.2396	0.0636	20.6914	0.0447	20.1206	1.119
4	51	4_51	151.1884	-7.7851	22.8866	0.1409	21.7932	0.0757	20.3973	2.4893
4	52	4_52	151.1967	-7.7745	19.2055	0.0246	18.8546	0.019	18.4338	0.7717
4	53	4_53	151.1705	-7.7980	20.6852	0.0491	19.6538	0.0275	18.3695	2.3157
4	54	4_54	151.1801	-7.7857	23.1303	0.1617	22.7852	0.121	22.1342	0.9961
4	55	4_55	151.1811	-7.7820	22.3181	0.1069	21.945	0.0815	21.495	0.8231
4	56	4_56	151.2129	-7.7478	19.9961	0.0356	19.489	0.0255	18.9694	1.0267
4	57	4_57	151.1687	-7.7888	22.1897	0.1013	21.3645	0.0626	20.6163	1.5734

Field	Slit ID	Object ID	RA	Dec	V	V error	R	R error	I	I error
4	58	4_58	151.1862	-7.7649	21.8791	0.0862	20.9196	0.0497	20.0305	1.8486
4	59	4_59	151.19	-7.7586	22.5199	0.1183	21.9708	0.0834	21.2165	1.3034
4	60	4_60	151.168	-7.7780	22.5949	0.1223	21.7384	0.0741	20.7908	1.8041
4	61	4_61	151.1601	-7.7831	22.8741	0.1389	21.8613	0.0782	20.6621	2.212
4	62	4_62	151.1744	-7.7662	19.8604	0.0334	19.3308	0.0238	18.9148	0.9456
5	1	5_1	151.3734	-7.7169	23.4987	0.1903	22.7861	0.1308	22.4648	1.0339
5	2	5_2	151.3601	-7.7300	21.1829	0.0621	20.6119	0.0432	20.069	1.1139
5	5	5_5	151.3203	-7.7695	20.3278	0.0419	19.7622	0.0291	19.1049	1.2229
5	7	5_7	151.3945	-7.7682	23.6589	0.2068	22.2885	0.098	21.2106	2.4483
5	8	5_8	151.3981	-7.7614	20.1566	0.0385	19.7494	0.0288	19.2962	0.8604
5	9	5_9	151.4021	-7.7545	22.9893	0.147	22.5403	0.1082	21.9417	1.0476
5	10	5_10	151.3479	-7.8056	21.1041	0.06	20.6328	0.0437	20.0621	1.042
5	11	5_11	151.3993	-7.7528	24.2172	0.2879	23.2152	0.1635	22.5032	1.714
5	12	5_12	151.3842	-7.7659	21.9867	0.0908	21.409	0.0634	20.8287	1.158
5	13	5_13	151.3885	-7.7593	22.5141	0.1208	21.1242	0.0574	19.9915	2.5226
5	14	5_14	151.396	-7.7496	20.2016	0.0402	19.6623	0.0287	19.1268	1.0748
5	15	5_15	151.3967	-7.7468	23.6757	0.2244	22.9911	0.1606	22.7963	0.8794

Field	Slit ID	Object ID	RA	Dec	V	V error	R	R error	I	I error
5	16	5_16	151.3936	-7.7486	22.9614	0.1492	22.4728	0.1103	21.8704	1.091
5	18	5_18	151.3507	-7.7862	22.9135	0.1415	22.2381	0.0943	21.6612	1.2523
5	19	5_19	151.3945	-7.7448	22.5762	0.1286	21.2888	0.064	20.2041	2.3721
5	20	5_20	151.3924	-7.7422	22.9385	0.1497	21.7213	0.0751	20.6259	2.3126
5	21	5_21	151.3812	-7.7506	21.837	0.085	21.2883	0.0599	20.5279	1.3091
5	22	5_22	151.3301	-7.7984	22.5447	0.1188	21.2725	0.059	19.2031	3.3416
5	23	5_23	151.3823	-7.7438	22.9857	0.1474	22.0299	0.0846	20.4627	2.523
5	24	5_24	151.3886	-7.7349	20.4768	0.0447	19.8908	0.0308	19.3319	1.1449
5	25	5_25	151.3789	-7.7422	21.9669	0.0899	21.3343	0.0611	20.6224	1.3445
5	26	5_26	151.3591	-7.7593	21.2623	0.0645	20.3356	0.0379	19.4307	1.8316
5	27	5_27	151.3654	-7.7504	20.4772	0.0447	20.1319	0.0345	19.7135	0.7637
5	28	5_28	151.3643	-7.7486	21.626	0.0766	21.0279	0.0531	20.5387	1.0873
5	29	5_29	151.356	-7.7538	19.1917	0.0247	18.278	0.0146	17.3404	1.8513
5	30	5_30	151.3427	-7.7646	23.0399	0.1507	22.446	0.1059	21.8586	1.1813
5	31	5_31	151.3553	-7.7499	19.233	0.0251	18.7696	0.0183	18.3021	0.9309
5	32	5_32	151.3449	-7.7575	21.0852	0.0583	20.6655	0.0438	20.2072	0.878
5	33	5_33	151.3201	-7.7796	20.4013	0.0432	19.8576	0.0303	19.246	1.1553

Field	Slit ID	Object ID	RA	Dec	V	V error	R	R error	I	I error
5	34	5_34	151.34	-7.7573	22.4669	0.1141	21.4305	0.0636	19.8685	2.5984
5	35	5_35	151.3336	-7.7612	22.7146	0.1289	21.6297	0.0699	20.1013	2.6133
5	36	5_36	151.3537	-7.7349	22.3413	0.1075	21.6575	0.0715	21.0185	1.3228
5	37	5_37	151.3644	-7.7213	21.6502	0.0774	21.2058	0.0574	20.6604	0.9898
5	38	5_38	151.3496	-7.7328	20.1139	0.0378	19.7342	0.0286	19.3354	0.7785
5	39	5_39	151.3451	-7.7344	22.7335	0.1301	22.153	0.0907	21.5966	1.1369
5	40	5_40	151.3364	-7.7399	19.8841	0.034	19.447	0.025	18.985	0.8991
5	41	5_41	151.3469	-7.7259	20.5975	0.0473	20.1307	0.0344	19.6894	0.9081
5	42	5_42	151.3297	-7.7396	20.4761	0.0447	19.9863	0.0322	19.4329	1.0432
5	43	5_43	151.3215	-7.7451	22.4518	0.1142	21.9294	0.083	21.3148	1.137
5	44	5_44	151.3126	-7.7513	22.0001	0.0897	21.2938	0.0595	20.6901	1.31
5	45	5_45	151.2994	-7.7584	22.7305	0.1284	22.1102	0.0879	21.4213	1.3092
5	46	5_46	151.2914	-7.7498	19.103	0.0237	18.6672	0.0174	18.2529	0.8501
5	47	5_47	151.3027	-7.7358	19.0775	0.0234	18.5216	0.0163	17.9407	1.1368
5	48	5_48	151.319	-7.7166	20.8459	0.0532	20.2825	0.0371	19.7905	1.0554
5	49	5_49	151.3284	-7.7045	21.7535	0.0811	21.229	0.0577	20.5895	1.164
5	50	5_50	151.3314	-7.6988	20.8376	0.0531	20.1727	0.035	19.6325	1.2051

Field	Slit ID	Object ID	RA	Dec	V	V error	R	R error	I	I error
5	51	5_51	151.3363	-7.6909	21.4588	0.0706	20.8319	0.0479	20.1834	1.2754
5	52	5_52	151.3223	-7.7020	23.074	0.1518	22.7759	0.1244	22.3885	0.6855
5	53	5_53	151.3177	-7.7040	21.8472	0.0845	21.2341	0.0576	20.6292	1.218
5	54	5_54	151.3158	-7.7036	21.1635	0.0616	20.5309	0.0416	19.7899	1.3736
5	55	5_55	151.2754	-7.7411	20.4379	0.0439	19.8434	0.0301	19.1804	1.2575
5	56	5_56	151.2929	-7.7211	22.0762	0.0944	21.5045	0.0657	20.7497	1.3265
5	57	5_57	151.31	-7.7016	21.1089	0.06	20.6339	0.0436	20.0908	1.0181
5	58	5_58	151.3047	-7.7043	19.9578	0.0348	19.3858	0.0242	18.7825	1.1753
5	59	5_59	151.2748	-7.7312	23.0359	0.149	22.3083	0.0966	21.8113	1.2246
5	60	5_60	151.2974	-7.7061	20.5358	0.0459	20.0225	0.0327	19.4906	1.0452
5	61	5_61	151.293	-7.7080	21.9965	0.0912	21.3623	0.062	20.9094	1.0871
5	62	5_62	151.2997	-7.6986	20.9183	0.0551	20.3556	0.0383	19.7233	1.195
5	63	5_63	151.3232	-7.7311	21.6028	0.0755	21.0542	0.053	20.5274	1.0754
5	64	5_64	151.3166	-7.7308	23.6704	0.2115	23.2393	0.1652	22.5958	1.0746

Table 2: Table of GC targets listing: Object ID, SNR, Velocity, Velocity Error, metallicity and metallicity error obtained from pPXF.

Object ID	SNR	Velocity	Vel error	[Z/H]	[Z/H] error
1_12	37	187	3	-0.43	0.07
1_14	6	1074	242		
1_15	5	484	23		
1_19	21	1127	5	-0.19	0.08
1_21	7	992	29		
1_22	8	476	69		
1_24	9	223	223	-0.79	0.13
1_25	9	822	14	-0.21	0.07
1_28	6	1072	18		
1_29	5	831	21		
1_32	11	646	42	-0.87	0.11
1_35	19	328	7	-0.33	0.07
1_37	13	894	8	-0.22	0.07
1_38	6	601	9		
1_43	5	572	258		
1_44	15	86	6	0.09	0.07
2_15	7	380	13		
2_18	9	503	17	-0.28	0.41
2_20	6	689	51		
2_21	8	442	27		
2_23	7	470	42		
2_24	6	402	64		
2_25	15	410	7	-0.4	0.07
2_26	17	136	6	-0.11	0.07
2_28	19	501	7	-0.26	0.07

Object ID	SNR	Velocity	Vel error	[Z/H]	[Z/H] error
2_29	6	497	25		
2_30	15	143	15	-0.66	0.08
2_35	474	23	5		
2_40	7	1199	13		
2_42	10	435	8	-0.21	0.07
2_43	8	751	11	-0.35	0.08
2_47	17	671	7	0	0.07
2_52	10	807	10	-0.23	0.07
2_53	14	479	12	-0.53	0.13
2_60	14	30	9	-0.32	0.08
3_10	16	136	7	-0.43	0.08
3_11	9	600	35	-0.74	0.22
3_13	7	19	15		
3_16	5	163	509		
3_18	11	685	46	-0.19	0.71
3_19	6	718	76		
3_20	10	-1400	1000	-0.71	0.21
3_21	6	600	0		
3_25	6	112	12		
3_26	7	6	18		
3_29	6	809	19		
3_31	20	2600	0	0.11	0.07
3_35	12	191	23	-0.69	0.09
3_38	7	140	9		
3_39	6	79	23		
3_41	33	369	17	-1.37	0.08
3_42	10	173	13	-0.29	0.09

Object ID	SNR	Velocity	Vel error	[Z/H]	[Z/H] error
3_44	12	600	2		
3_45	10	39	9	-0.19	0.71
3_49	10	72	29	-0.2	0.71
3_53	6	1019	230		
3_58	16	510	52	-1.11	0.14
4_8	13	108	132	-0.19	0.07
4_10	33	212	25	-0.61	0.12
4_12	9	-4	23	-0.52	0.08
4_13	9	600	23	-0.47	0.08
4_16	13	600	27	-1.09	0.10
4_21	9	162	34	-0.63	0.09
4_27	9	213	9	-0.19	0.71
4_29	5	600	0		
4_30	6	459	333		
4_32	8	181	32	-1.05	0.24
4_35	7	-209	525		
4_37	13	474	29	-0.88	0.32
4_38	52	193	3	0.01	0.07
4_43	7	600	39		
4_46	17	90	5	0.04	0.07
4_48	15	-618	551	-0.37	0.07
4_49	11	26	16	-0.31	0.07
4_50	10	693	55	-0.55	0.14
4_52	43	-14	16	-1.6	0.07
4_53	26	-8	92	-0.09	0.07
4_56	26	74	5	-0.15	0.07
4_58	6	6	28		

Object ID	SNR	Velocity	Vel error	[Z/H]	[Z/H] error
4_62	27	792	10	-0.94	0.1
5_8	27	170	7	-0.59	0.08
5_10	8	684	27		
5_12	5	837	139		
5_14	13	600	0	-1.11	0.15
5_18	5	410	157		
5_24	17	216	6	-0.15	0.07
5_25	6	689	51		
5_26	8	24	15		
5_27	22	303	90	-0.66	0.27
5_28	7	194	23		
5_31	42	194	4	-0.4	0.07
5_32	11	195	17	-0.9	0.18
5_33	18	721	7	-0.43	0.07
5_37	8	673	49		
5_38	27	3	14	-0.83	0.11
5_40	30	105	5	-0.33	0.08
5_41	16	410	9	-0.22	0.07
5_42	16	943	16	-0.98	0.1
5_46	46	89	3	-0.58	0.07
5_47	37	481	4	-0.36	0.07
5_48	7	698	62		
5_49	5	974	201		
5_50	9	967	27	-0.19	0.13
5_51	7	912	19		
5_55	15	538	33	-0.27	0.07
5_57	8	708	105	-1.01	0.25

Object ID	SNR	Velocity	Vel error	[Z/H]	[Z/H] error
5_58	13	922	8	-0.27	0.07
5_60	15	754	16	-0.77	0.22
5_62	11	950	9	-0.28	0.07
5_63	8	800	18		

Bibliography

Abadi, M. G., J. F. Navarro, and M. Steinmetz (2006). “Stars beyond galaxies: the origin of extended luminous haloes around galaxies”. In: 365, pp. 747–758. DOI: `10.1111/j.1365-2966.2005.09789.x`. eprint: `astro-ph/0506659`.

Abolfathi, B. et al. (2017). “The Fourteenth Data Release of the Sloan Digital Sky Survey: First Spectroscopic Data from the extended Baryon Oscillation Spectroscopic Survey and from the second phase of the Apache Point Observatory Galactic Evolution Experiment”. In: *ArXiv e-prints*. arXiv: `1707.09322`.

Appenzeller, I. et al. (1998). “Successful commissioning of FORS1 - the first optical instrument on the VLT.” In: *The Messenger* 94, pp. 1–6.

Aragón-Salamanca, A., A. G. Bedregal, and M. R. Merrifield (2006). “Measuring the fading of S0 galaxies using globular clusters”. In: 458, pp. 101–105. DOI: `10.1051/0004-6361:20065948`. eprint: `astro-ph/0607645`.

Arnold, J. A. et al. (2011). “The Fossil Record of Two-phase Galaxy Assembly: Kinematics and Metallicities in the Nearest S0 Galaxy”. In: 736, L26, p. L26. DOI: `10.1088/2041-8205/736/2/L26`. arXiv: `1106.0745`.

Ashman, K. M. and S. E. Zepf (1992). “The formation of globular clusters in merging and interacting galaxies”. In: 384, pp. 50–61. DOI: `10.1086/170850`.

Barmby, P. et al. (2000). “M31 Globular Clusters: Colors and Metallicities”. In: 119, pp. 727–747. DOI: `10.1086/301213`. eprint: `astro-ph/9911152`.

Barr, J. M. et al. (2007). “The formation of S0 galaxies: evidence from globular clusters”. In: 470, pp. 173–178. DOI: `10.1051/0004-6361:20077151`. arXiv: `0705.0623`.

Bender, R., R. P. Saglia, and O. E. Gerhard (1994). “Line-of-Sight Velocity Distributions of Elliptical Galaxies”. In: 269, p. 785. DOI: `10.1093/mnras/269.3.785`.

Bertin, E. and S. Arnouts (1996). “SExtractor: Software for source extraction.” In: 117, pp. 393–404. DOI: `10.1051/aas:1996164`.

Bezanson, R. et al. (2009). “The Relation Between Compact, Quiescent High-redshift Galaxies and Massive Nearby Elliptical Galaxies: Evidence for Hierarchical, Inside-Out Growth”. In: 697, pp. 1290–1298. DOI: `10.1088/0004-637X/697/2/1290`. arXiv: `0903.2044 [astro-ph.CO]`.

Bournaud, F., C. J. Jog, and F. Combes (2005). “Galaxy mergers with various mass ratios: Properties of remnants”. In: 437, pp. 69–85. DOI: `10.1051/0004-6361:20042036`. eprint: `astro-ph/0503189`.

— (2007). “Multiple minor mergers: formation of elliptical galaxies and constraints for the growth of spiral disks”. In: 476, pp. 1179–1190. DOI: `10.1051/0004-6361:20078010`. arXiv: `0709.3439`.

Brodie, J. P. and J. P. Huchra (1991). “Extragalactic globular clusters. III - Metallicity comparisons and anomalies”. In: 379, pp. 157–167. DOI: `10.1086/170492`.

Brodie, J. P. and J. Strader (2006). “Extragalactic Globular Clusters and Galaxy Formation”. In: 44, pp. 193–267. DOI: `10.1146/annurev.astro.44.051905.092441`. eprint: `astro-ph/0602601`.

Brodie, J. P. et al. (2012). “The SLUGGS Survey: NGC 3115, A Critical Test Case for Metallicity Bimodality in Globular Cluster Systems”. In: 759, L33, p. L33. DOI: `10.1088/2041-8205/759/2/L33`. arXiv: `1209.5390`.

Bruzual, G. and S. Charlot (2003). “Stellar population synthesis at the resolution of 2003”. In: 344, pp. 1000–1028. DOI: `10.1046/j.1365-8711.2003.06897.x`. eprint: `astro-ph/0309134`.

Burstein, D. et al. (2005). “The K-Band Luminosities of Galaxies: Do S0s Come from Spiral Galaxies?” In: 621, pp. 246–255. DOI: `10.1086/427408`.

Cantiello, M. et al. (2014). “Globular clusters of NGC 3115 in the near-infrared. Demonstrating the correctness of two opposing scenarios”. In: 564, L3, p. L3. DOI: `10.1051/0004-6361/201323272`. arXiv: `1402.6090`.

Cappellari, M. (2017). “Improving the full spectrum fitting method: accurate convolution with Gauss-Hermite functions”. In: 466, pp. 798–811. DOI: `10.1093/mnras/stw3020`. arXiv: `1607.08538`.

Côté, P., R. O. Marzke, and M. J. West (1998). “The Formation of Giant Elliptical Galaxies and Their Globular Cluster Systems”. In: 501, pp. 554–570. DOI: `10.1086/305838`. eprint: `astro-ph/9804319`.

Decressin, T., H. Baumgardt, and P. Kroupa (2008). “The evolution of two stellar populations in globular clusters. I. The dynamical mixing timescale”. In: 492, pp. 101–109. DOI: `10.1051/0004-6361:200810275`. arXiv: `0810.5345`.

Dressler, A. et al. (1997). “Evolution since z = 0.5 of the Morphology-Density Relation for Clusters of Galaxies”. In: 490, pp. 577–591. DOI: `10.1086/304890`. eprint: `astro-ph/9707232`.

Elmegreen, D. M. et al. (2002). “Arm Structure in Anemic Spiral Galaxies”. In: 124, pp. 777–781. DOI: `10.1086/341613`. eprint: `astro-ph/0205105`.

Emsellem, E. et al. (2004). “The SAURON project - III. Integral-field absorption-line kinematics of 48 elliptical and lenticular galaxies”. In: 352, pp. 721–743. DOI: `10.1111/j.1365-2966.2004.07948.x`. eprint: `astro-ph/0404034`.

Engl, H.W., M. Hanke, and A. Neubauer (2000). *Regularization of Inverse Problems.* Mathematics and Its Applications. Springer Netherlands. ISBN: 9780792361404. URL: `https://books.google.co.uk/books?id=VuEV-Gj1GZcC`.

ESO (2011a). *FORS2 standard grisms.* URL: `http://www.eso.org/sci/facilities/paranal/instruments/fors/inst/grisms.html`.

— (2011b). *The Very Large Telescope.* URL: `http://www.eso.org/public/teles-instr/paranal-observatory/vlt/`.

ESO (2016). *EsoRex*. URL: `https://www.eso.org/sci/software/cpl/esorex.html`.

Faber, S. M. et al. (1985). "Old stellar populations. II - an analysis of K-giant spectra". In: 57, pp. 711–741. DOI: `10.1086/191024`.

Ferraro, F. R. et al. (2004). "The Discovery of an Anomalous Subgiant Branch in the Color-Magnitude Diagram of ω Centauri". In: 603, pp. L81–L84. DOI: `10.1086/383149`. eprint: `astro-ph/0401540`.

Fisher, D. (1997). "Kinematic Profiles of SO Galaxies". In: 113, p. 950. DOI: `10.1086/118312`.

Forbes, D. A., J. P. Brodie, and C. J. Grillmair (1997). "On the Origin of Globular Clusters in Elliptical and cD Galaxies". In: 113, p. 1652. DOI: `10.1086/118382`. eprint: `astro-ph/9702146`.

Forbes, D. A. and J. C. Forte (2001). "The connection between globular cluster systems and the host galaxies". In: 322, pp. 257–261. DOI: `10.1046/j.1365-8711.2001.04052.x`. eprint: `astro-ph/0005481`.

Forbes, D. A. et al. (2011). "Evidence for two phases of galaxy formation from radial trends in the globular cluster system of NGC 1407". In: 413, pp. 2943–2949. DOI: `10.1111/j.1365-2966.2011.18373.x`. arXiv: `1101.3575`.

Forbes, Duncan (2017). *The SLUGGS Survey*. URL: `http://sluggs.swin.edu.au/Survey.html`.

Foster, C. et al. (2010). "Deriving Metallicities from the Integrated Spectra of Extragalactic Globular Clusters Using the Near-infrared Calcium Triplet". In: 139, pp. 1566–1578. DOI: `10.1088/0004-6256/139/4/1566`. arXiv: `1002.1107 [astro-ph.CO]`.

Foster, C. et al. (2011). "Global properties of 'ordinary' early-type galaxies: photometry and spectroscopy of stars and globular clusters in NGC 4494". In: 415, pp. 3393–3416. DOI: `10.1111/j.1365-2966.2011.18965.x`. arXiv: `1104.5503`.

Freudling, W. et al. (2013). “Automated data reduction workflows for astronomy. The ESO Reflex environment”. In: 559, A96, A96. DOI: `10.1051/0004-6361/201322494`. arXiv: `1311.5411 [astro-ph.IM]`.

Fukugita, M, CJ Hogan, and PJE Peebles (1998). “The Cosmic baryon budget”. In: *The Astrophysical Journal* 503.2, p. 518.

Harris, W. E. (1991a). “Globular cluster systems in galaxies beyond the Local Group”. In: 29, pp. 543–579. DOI: `10.1146/annurev.aa.29.090191.002551`.

— (1996). “A Catalog of Parameters for Globular Clusters in the Milky Way”. In: 112, p. 1487. DOI: `10.1086/118116`.

Harris, W. E. and S. van den Bergh (1981). “Globular clusters in galaxies beyond the local group. I - New cluster systems in selected northern ellipticals”. In: 86, pp. 1627–1642. DOI: `10.1086/113047`.

Harris, William (1991b). *SPECIFIC FREQUENCY AND SPECIFIC LUMINOSITY*. URL: `https://ned.ipac.caltech.edu/level5/Harris/Harris4.html`.

Jennings, Z. G. et al. (2014). “The SLUGGS Survey: HST/ACS Mosaic Imaging of the NGC 3115 Globular Cluster System”. In: 148, 32, p. 32. DOI: `10.1088/0004-6256/148/2/32`. arXiv: `1405.0008`.

Kundu, A. and B. C. Whitmore (1998). “Wide Field Planetary Camera 2 Imaging of the Globular Cluster System of the S0 Galaxy NGC 3115”. In: 116, pp. 2841–2853. DOI: `10.1086/300643`.

Kundu, A. and S. E. Zepf (2007). “Bimodal Infrared Colors of the M87 Globular Cluster System: Peaks in the Metallicity Distribution”. In: 660, pp. L109–L112. DOI: `10.1086/518214`. eprint: `astro-ph/0703376`.

Kundu, Arunav and Bradley C Whitmore (2001). “New Insights from Hubble Space Telescope Studies of Globular Cluster Systems. II. Analysis of 29 S0 Systems”. In: *The Astronomical Journal* 122.3, p. 1251.

Kuntschner, H. et al. (2002). “VLT spectroscopy of NGC 3115 globular clusters”. In: 395, pp. 761–777. DOI: `10.1051/0004-6361:20021325`. eprint: `astro-ph/0209129`.

Larsen, S. S. et al. (2001). “Properties of Globular Cluster Systems in Nearby Early-Type Galaxies”. In: 121, pp. 2974–2998. DOI: `10.1086/321081`. eprint: `astro-ph/0102374`.

Lawson, C.L. and R.J. Hanson (1974). *Solving Least Squares Problems.* Classics in Applied Mathematics. Society for Industrial and Applied Mathematics. ISBN: 9780898713565. URL: `https://books.google.co.uk/books?id=ROw4hU85nz8C`.

Lützgendorf, N. et al. (2012). “Central kinematics of the globular cluster NGC 2808: upper limit on the mass of an intermediate-mass black hole”. In: 542, A129, A129. DOI: `10.1051/0004-6361/201219375`. arXiv: `1204.4074`.

Lützgendorf, N. et al. (2013). “Limits on intermediate-mass black holes in six Galactic globular clusters with integral-field spectroscopy”. In: 552, A49, A49. DOI: `10.1051/0004-6361/201220307`. arXiv: `1212.3475`.

Marino, A. F. et al. (2008). “Spectroscopic and photometric evidence of two stellar populations in the Galactic globular cluster NGC 6121 (M 4)”. In: 490, pp. 625–640. DOI: `10.1051/0004-6361:200810389`. arXiv: `0808.1414`.

Materne, J. (1979). “The structure of nearby groups of galaxies - Quantitative membership probabilities”. In: 74, pp. 235–243.

Miyazaki, S. et al. (2002). “Subaru Prime Focus Camera – Suprime-Cam”. In: 54, pp. 833–853. DOI: `10.1093/pasj/54.6.833`. eprint: `astro-ph/0211006`.

Moore, B., G. Lake, and N. Katz (1998). “Morphological Transformation from Galaxy Harassment”. In: 495, pp. 139–151. DOI: `10.1086/305264`. eprint: `astro-ph/9701211`.

Naab, T., P. H. Johansson, and J. P. Ostriker (2009). “Minor Mergers and the Size Evolution of Elliptical Galaxies”. In: 699, pp. L178–L182. DOI: `10.1088/0004-637X/699/2/L178`. arXiv: `0903.1636 [astro-ph.CO]`.

Newman, MEJ and GT Barkema (1999). *Monte Carlo Methods in Statistical Physics chapter 1-4*. Oxford University Press: New York, USA.

Norris, M. A., R. M. Sharples, and H. Kuntschner (2006). "GMOS spectroscopy of the S0 galaxy NGC 3115". In: 367, pp. 815–824. DOI: `10.1111/j.1365-2966.2005.09992.x`. eprint: `astro-ph/0601221`.

Paturel, G. et al. (2002). "Comparison LEDA/SIMBAD octobre 2002. Catalogue to be published in 2003." In: *LEDA, 0 (2002).*

Peng, E. W. et al. (2006a). "The ACS Virgo Cluster Survey. XI. The Nature of Diffuse Star Clusters in Early-Type Galaxies". In: 639, pp. 838–857. DOI: `10.1086/499485`. eprint: `astro-ph/0511251`.

Peng, Eric W et al. (2006b). "The ACS Virgo Cluster Survey. IX. The color distributions of globular cluster systems in early-type galaxies". In: *The Astrophysical Journal* 639.1, p. 95.

Piotto, G. et al. (2007). "A Triple Main Sequence in the Globular Cluster NGC 2808". In: 661, pp. L53–L56. DOI: `10.1086/518503`. eprint: `astro-ph/0703767`.

Press, William H (2007). *Numerical recipes 3rd edition: The art of scientific computing*. Cambridge university press.

Puzia, T. H. et al. (2002). "Extragalactic globular clusters in the near-infrared. II. The globular clusters systems of NGC 3115 and NGC 4365". In: 391, pp. 453–470. DOI: `10.1051/0004-6361:20020835`. eprint: `astro-ph/0206147`.

Puzia, T. H. et al. (2004). "VLT spectroscopy of globular cluster systems. I. The photometric and spectroscopic data set". In: 415, pp. 123–143. DOI: `10.1051/0004-6361:20031448`. eprint: `astro-ph/0505448`.

Qu, Y. et al. (2010). "The slowing down of galaxy disks in dissipationless minor mergers". In: 515, A11, A11. DOI: `10.1051/0004-6361/200913559`. arXiv: `1002.3375 [astro-ph.GA]`.

Sánchez-Blázquez, P. et al. (2006). "Medium-resolution Isaac Newton Telescope library of empirical spectra". In: 371, pp. 703–718. DOI: `10.1111/j.1365-2966.2006.10699.x`. eprint: `astro-ph/0607009`.

Sandage, A. (2005). “The Classification of Galaxies: Early History and Ongoing Developments”. In: 43, pp. 581–624. DOI: `10.1146/annurev.astro.43.112904.104839`.

Schweizer, F. (2000). “Interactions as a driver of galaxy evolution”. In: *Astronomy, physics and chemistry of H*\$$^{+}$\$\$$_{3}$\$. Vol. 358. Philosophical Transactions of the Royal Society of London Series A, p. 2063. DOI: `10.1098/rsta.2000.0630`. eprint: `astro-ph/0002263`.

— (2002). “Evolution of Globular Clusters Formed in Mergers”. In: *Extragalactic Star Clusters*. Ed. by D. P. Geisler, E. K. Grebel, and D. Minniti. Vol. 207. IAU Symposium, p. 630. eprint: `astro-ph/0106345`.

Spitler, Lee R., Duncan A. Forbes, and Michael A. Beasley (2008). “Extending the baseline: Spitzer mid-infrared photometry of globular cluster systems in the Centaurus A and Sombrero Galaxies”. In: *Monthly Notices of the Royal Astronomical Society* 389.3, pp. 1150–1162. ISSN: 1365-2966. DOI: `10.1111/j.1365-2966.2008.13681.x`. URL: `http://dx.doi.org/10.1111/j.1365-2966.2008.13681.x`.

Strader, J., J. P. Brodie, and D. A. Forbes (2004). “Metal-Poor Globular Clusters and Galaxy Formation”. In: 127, pp. 3431–3436. DOI: `10.1086/420995`. eprint: `astro-ph/0403160`.

Strader, J. et al. (2006). “Globular Clusters in Virgo Ellipticals: Unexpected Results for Giants and Dwarfs from Advanced Camera for Surveys Imaging”. In: 132, pp. 2333–2345. DOI: `10.1086/509124`. eprint: `astro-ph/0508001`.

Tonry, J. L. et al. (2001). “The SBF Survey of Galaxy Distances. IV. SBF Magnitudes, Colors, and Distances”. In: 546, pp. 681–693. DOI: `10.1086/318301`. eprint: `astro-ph/0011223`.

Toomre, A. and J. Toomre (1972). “Galactic Bridges and Tails”. In: 178, pp. 623–666. DOI: `10.1086/151823`.

Trager, S. C. et al. (1998). “Old Stellar Populations. VI. Absorption-Line Spectra of Galaxy Nuclei and Globular Clusters”. In: 116, pp. 1–28. DOI: `10.1086/313099`. eprint: `astro-ph/9712258`.

Usher, C. et al. (2012). “The SLUGGS survey: calcium triplet-based spectroscopic metallicities for over 900 globular clusters”. In: 426, pp. 1475–1495. DOI: `10.1111/j.1365-2966.2012.21801.x`. arXiv: `1207.6402 [astro-ph.CO]`.

van den Bergh, S. (1975). “Stellar populations in galaxies”. In: 13, pp. 217–255. DOI: `10.1146/annurev.aa.13.090175.001245`.

— (1982). “Globular clusters and galaxy mergers”. In: 94, pp. 459–464. DOI: `10.1086/131007`.

Vazdekis, A. et al. (2010). “Evolutionary stellar population synthesis with MILES - I. The base models and a new line index system”. In: 404, pp. 1639–1671. DOI: `10.1111/j.1365-2966.2010.16407.x`. arXiv: `1004.4439 [astro-ph.CO]`.

Vitvitska, M. et al. (2002). “The Origin of Angular Momentum in Dark Matter Halos”. In: 581, pp. 799–809. DOI: `10.1086/344361`. eprint: `astro-ph/0105349`.

West, M. J. (1993). “Biased Globular Cluster Formation”. In: 265, p. 755. DOI: `10.1093/mnras/265.3.755`.

Worthey, G. and D. L. Ottaviani (1997). “Hγ and Hδ Absorption Features in Stars and Stellar Populations”. In: 111, pp. 377–386. DOI: `10.1086/313021`.

Yoon, S.-J., S. K. Yi, and Y.-W. Lee (2006). “Explaining the Color Distributions of Globular Cluster Systems in Elliptical Galaxies”. In: *Science* 311, pp. 1129–1132. DOI: `10.1126/science.1122294`. eprint: `astro-ph/0601526`.

Yoon, S.-J. et al. (2011). “Nonlinear Color-Metallicity Relations of Globular Clusters. III. On the Discrepancy in Metallicity between Globular Cluster Systems and Their Parent Elliptical Galaxies”. In: 743, 150, p. 150. DOI: `10.1088/0004-637X/743/2/150`. arXiv: `1109.5178`.

Zepf, S. E. and K. M. Ashman (1993). “Globular Cluster Systems Formed in Galaxy Mergers”. In: 264, p. 611. DOI: `10.1093/mnras/264.3.611`.

Zinn, R. (1985). “The globular cluster system of the galaxy. IV - The halo and disk subsystems”. In: 293, pp. 424–444. DOI: `10.1086/163249`.